Dynamical and Chemical Properties of Magnetised Star-forming Regions

Elena Redaelli

München 2020

Dynamical and Chemical Properties of Magnetised Star-forming Regions

Elena Redaelli

Dissertation
an der Fakultät für Physik
der Ludwig–Maximilians–Universität
München

vorgelegt von
Elena Redaelli
aus Lecco, Italien

München, den 23/01/2020

Erstgutachter: Prof. Dr. Paola Caselli
Zweitgutachter: Prof. Dr. Andreas Burkert
Tag der mündlichen Prüfung: 06/03/2020

In carminibus Appius ait,
fabrum esse suae quemque fortunae.

Epistula ad Caesarem senem de re publica

Contents

List of Figures

List of Tables

Zusammenfassung

Zweifellos spielen die Sterne die führende Rolle am Nachthimmel, und ihre Beobachtungen gehen auf den Ursprung der Menschheit zurück, wenn auch anfangs aus einer Perspektive des Staunens und der Mythologie. Doch erst im XX. Jahrhundert begannen die Wissenschaftler, das frühe Leben der Sterne systematisch zu erforschen. Die Sternentstehung ist zu einem zentralen Thema der modernen Astrophysik geworden, und wo, wann und wie Sterne geboren werden, sind Fragen, die noch gründlich beantwortet werden müssen. Noch in jüngster Zeit haben sich die Astrochemie und die Astrobiologie auf diesem Gebiet immer mehr durchgesetzt. Tatsächlich ist die Sternentstehung auch eine Geschichte von zunehmender chemischer Komplexität, die um mindestens einen eigentümlichen Stern herum zur Entstehung von Leben führte.

Diese Doktorarbeit konzentriert sich auf mehrere Aspekte der Entstehung massearmer Sterne, hauptsächlich aus astrochemischer Sicht. Prästellare Kerne —kalte und dichte Fragmente von Molekülwolken am Rande des Gravitationskollapses— stellen den Geburtsort sonnenähnlicher Sterne dar. In den ersten beiden Teilen dieser Arbeit konzentriere ich mich auf diese Art von Objekten, indem sie die Isotopenzusammensetzung der reichlich vorhandenen Moleküle im kalten interstellaren Medium untersuche. Tatsächlich werden Fraktionierungsprozesse, die den molekularen Isotopengehalt verändern, als ein guter diagnostischer Tracer für die verschiedenen Sternentstehungsphasen angesehen.

Insbesondere analysiere ich zunächst das Stickstoff-Isotopenverhältnis im Diazenylium (N_2H^+) in einer kleinen Stichprobe von prästellaren Kernen. In den letzten Jahrzehnten hat die Fraktionierung von Stickstoff in der Astrochemie großes Interesse erlangt, da sie es uns ermöglichen könnte, die verschiedenen Materialien, die das eigentliche Planetensystem bilden, mit der ursprünglichen interstellaren Materie zu verbinden. Sein Isotopenverhältnis kann uns daher helfen, grundlegende Fragen zu beantworten, wie zum Beispiel, wie und in welchem Ausmaß unser Planet seine Zusammensetzung vom ursprünglichen Sonnennebel geerbt hat. Um dieses Ziel zu erreichen, ist jedoch ein umfassendes Verständnis der Stickstoffchemie erforderlich, und weitere Beobachtungsdaten, wie sie in dieser Arbeit vorgestellt werden, können weitere Einschränkungen für die chemischen Modelle liefern.

Der zweite Teil handelt vom prästellaren Kern L1544. Insbesondere konzentriere ich mich auf den Deuterierungsgrad —d.h. die Fraktionierung von Wasserstoff— dieses Objekts und analysiere mehrere Rotationsübergänge von zwei üppig vorhandenen Ionen: Diazenylium und protoniertes Kohlenmonoxid (HCO^+). Diese aktuellen, qualitativ hochwertigen Daten erlauben es, zuverlässige Informationen über die raümliche Verteilung des Deuteriumanteils abzuleiten. Die Kombination eines fortschrittlichen Modells des Strahlungstransportes mit einem hochmod-

ernen chemischen Netzwerk wird genutzt um auch die Chemie dieser Moleküle in L1544 zu untersuchen.

Auf die prästellare Phase folgt die protostellare, in dem sich als Folge des Gravitationskollapses ein zentrales Objekt —ein Protostern— bildet. IRAS 15398-3359, das zu dieser Kategorie von Objekten gehört, wird im letzten Teil dieser Arbeit untersucht. Ich konzentriere mich auf die Untersuchung von Magnetfeldern, von denen bekannt ist, dass sie bei der Sternentstehung eine wichtige Rolle spielen. Tatsächlich können Magnetfelder die Gasströme regulieren, und bieten eine zusätzliche Druckquelle, die die Gravitationskraft ausgleicht. Ich benutze polarimetrische Beobachtungen der thermischen Staubemission aus dem protostellaren Kern, um die magnetische Stärke und Morphologie abzuleiten. Insbesondere bei letzterem stelle ich fest, dass die Feldlinien eine charakteristische Sanduhrform aufweisen, die auf einen magnetisch bedingten Kollaps hinweist.

Zukünftige Beobachtungen mit höherer Empfindlichkeit und besserer Winkelauflösung, möglicherweise mit den neuesten interferometrischen Einrichtungen, werden uns helfen, all diese miteinander verbundenen Aspekte der Sternentstehungstheorie noch mehr zu erhellen und Schritt für Schritt zu einem vollständigen Verständnis der Theorie zu gelangen.

Summary

Without a doubt, stars play the leading role in the night sky, and their observations trace back to the origin of humankind, even though at the beginning from a perspective of wonder and mythology. However, it was only in the XX century that scientists began systematically to study the early life of stars. Stellar formation has become a central subject in modern astrophysics, and where, when, and how stars are born are questions that still need thorough answers. Even more recently, astrochemistry and astrobiology became more and more prominent in this field. In fact, star formation is also a story of increasing chemical complexity, which around at least one peculiar star culminated in the emergence of life.

This thesis focuses on several aspects of low-mass star formation, mainly from an astrochemical point of view. Prestellar cores —cold and dense fragments of molecular clouds on the verge of gravitational collapse— represent the birth place of Sun-like stars. In the first two parts of this work I concentrate on this kind of objects, studying the isotopic composition of abundant molecules in the cold interstellar medium. In fact, fractionation processes, which alter the molecular isotopic content, are considered a good diagnostic tracer of the different star-forming phases.

In particular, I first analyse the nitrogen isotopic ratio in diazenylium (N_2H^+) in a small sample of prestellar cores. In the last few decades, nitrogen fractionation has become of key interest in astrochemistry, since it could allow us to link the various materials that constitute the actual planetary system to the pristine interstellar matter. Its isotopic ratio can hence help us answering fundamental questions, such as how and to which extent our planet inherited its composition from the primordial Solar Nebula. To achieve this goal, however, a comprehensive understanding of nitrogen chemistry is needed, and more observational data, such as the ones presented in this work, can provide further constraints for the chemical models.

The second part aims its attention to the prestellar core L1544. In particular, I focus on the deuteration level —i.e. hydrogen fractionation— of this object, analysing several rotational transitions of two abundant ions: diazenylium and protonated carbon monoxide (HCO^+). These recent, high-quality data allow to derive reliable information on the spatial distribution of the deuterium fraction. The combination of an advanced radiative transfer model with a state-of-the-art chemical network is used to investigate also the chemistry of these molecules in L1544.

The protostellar phase follows the prestellar one when, as a consequence of the gravitational collapse, a central object —a protostar— is formed. IRAS 15398-3359, which belongs to this category of objects, is studied in the last part of this thesis. I focus on the study of magnetic fields, which are known to play an important role in star formation. In fact, they can regulate gas flows,

and they provide an extra source of pressure balancing the gravitational pull. I use polarimetric observations of the dust thermal emission arising from the protostellar core to derive the magnetic strength and morphology. Concerning the latter, in particular, I find that the field lines present a characteristic hourglass shape, which is indicative of a magnetically-driven collapse.

Future observations with higher sensitivity and better angular resolution, possibly with the most recent interferometric facilities, will help us enlighten even more all these interconnected aspects of the star formation theory, moving step by step towards a complete understanding of it.

List of Constants used in This Thesis

We list here the main constants used throughout this work, together with their values. Concerning the system of units, we adopt the centimetre-gram-second (CGS) convention.

k_{B}	Boltzmann constant	$1.381 \times 10^{-16}\,\mathrm{erg\,K^{-1}}$
G	Gravitational constant	$6.674 \times 10^{-8}\,\mathrm{cm^{3}\,g^{-1}\,s^{-2}}$
h	Planck constant	$6.626 \times 10^{-27}\,\mathrm{erg\,s^{-1}}$
m_{H}	Hydrogen mass	$1.673 \times 10^{-24}\,\mathrm{g}$
$M_{\odot}$	Solar mass	$1.988 \times 10^{33}\,\mathrm{g}$
c	Speed of light	$2.998 \times 10^{10}\,\mathrm{cm\,s^{-1}}$

Chapter 1

Introduction

Figure 1.1: Copy of original photo of the North America Nebula by E. E. Barnard. The darkest regions, where only few stars are visible, correspond to the position of the molecular gas. Credit: http://www.catchersofthelight.com/catchers/post/2012/07/22/Edward-Emerson-Barnard-History-of-Astrophotography.

How stars form is a long-standing problem of modern astrophysics. The formation of low-mass stars[1] is particularly intriguing, since it is directly linked to how our own Solar System was

[1]Throughout this work, a star is high-mass if its initial mass is $> 8\,M_\odot$. Stars above this limit generally end their lifecycle through a supernova phase and their remnants are neutron stars or black holes. Low-mass stars, instead, become white dwarves. Often the range $2\,M_\odot < M < 8\,M_\odot$ is referred to as intermediate mass, whilst the very low-mass end is defined by $M < 2\,M_\odot$.

born. As a general picture, stars form in the interstellar medium from cold and dense gas, which is mainly composed by molecules.

Astrochemistry is the branch of astrophysics that studies the chemical composition and evolution of molecular gas. Its goal is to understand the increasing chemical complexity that during the star formation process leads to the first organic molecules, which are then inherited by circumstellar discs, where planets are born. Furthermore, the capability of molecules to trace different physical conditions of a source make their emission an ideal diagnostic tool to probe the physics and kinematics of the interstellar medium.

In this Introduction, we present some of the main concepts involved in the analysis of the star formation process. In §1.1, which is mostly based on Stahler & Palla (2005), we focus on the interstellar medium, in particular analysing its phases and stability. §1.2 describes the gas content of molecular clouds, with a special attention to the molecular line emission properties. In §1.3 we introduce fractionation processes, which alter the isotopic composition of molecules and can be used as diagnostic tools to follow the different star-forming phases. Section §1.4 contains the study of the properties of interstellar dust. In §1.5 we analyse another fundamental component of the interstellar medium: magnetic fields, which can greatly affect the dynamical evolution of star-forming regions. Section §1.6 provides a short description of radio telescopes, instruments used to detect the radiation coming from molecular clouds, and it is based mainly on Rohlfs & Wilson (2004). Finally, §1.7 contains the layout of this thesis.

1.1 The interstellar medium and star formation

Star formation is the story of how the diffuse phase of the interstellar medium (ISM) condensates in denser and denser material, and eventually collapses due to the gravitational pull to form protostellar objects. The study of this process is hence tightly linked to understanding the physical processes that involve the interstellar medium. In the following, we will focus on properties of one peculiar spiral galaxy, the Milky Way, which is however fairly representative of its kind. Spiral (and barred) galaxies, being still rich in gas content, are active in star formation, with typical rates[2] of $\approx 1 - 10\,M_\odot/\mathrm{yr}$.

The ISM exists in a number of different phases that are in pressure equilibrium with each other, spanning five orders of magnitude in density and temperature (McKee & Ostriker 1977). The *warm ionised medium* has a typical temperature of $T \approx 8 \times 10^3\,\mathrm{K}$ and a volume number density of $n \approx 0.3\,\mathrm{cm}^{-3}$, similarly to the *warm neutral medium*, where however most of hydrogen is not ionised. The *cold neutral medium* is characterised by lower temperatures ($T \approx 50 - 100\,\mathrm{K}$), and it is denser ($n \approx 50 - 100\,\mathrm{cm}^{-3}$). Finally the *molecular phase*, being the coldest and densest, is the one we are mainly interested in, since it represents the preferential site of star formation.

In the Milky Way, the molecular gas accounts for approximately $2 \times 10^9\,M_\odot$ (two order of magnitudes less than the total stellar mass), and about 80% of it is found in *giant molecular clouds* (GMCs), objects with a typical mass of $10^5\,M_\odot$ and typical temperatures of 10 K. The rest is located in smaller dark clouds ($M \sim 10^4\,M_\odot$) and in isolated cores ($M \sim 10 - 100\,M_\odot$).

[2] We would like to mention here that starbursts, usually small and irregular galaxies with high fractions of mass still in the gaseous phase, can exhibit star formation rate as high as $\approx 100 - 1000\,M_\odot/\mathrm{yr}$.

Due to their high densities, molecular clouds can efficiently block the majority of the background starlight, and as a consequence they stand out as dark patches in the shiny sky. Already described as *nebulae* centuries ago by William Herschel, many of them were catalogued by Edward Emerson Barnard at the beginning of the XX century (see Figure 1.1).

1.1.1 Clouds stability

Unlike the rest of the ISM, molecular clouds are not confined by being in pressure equilibrium with the surrounding medium. Instead, their dynamics is dominated by gravity. We can investigate their equilibrium state by means of the *virial theorem*, which in its simplest form reads:

$$\frac{1}{2}\frac{d^2I}{dt^2} = 2U + \Omega \,, \tag{1.1}$$

where I is the source moment of inertia, U is the thermal energy content and Ω the gravitational one. If the cloud is in equilibrium, then Eq. 1.1 must sum to zero (the moment of inertia is not varying in time), and one obtains $|\Omega| = 2U$. For a GMC of mass M, temperature T and size R, we have:

$$\frac{2U}{|\Omega|} \approx \left(2 \times \frac{3Mk_{\rm B}T}{2\mu m_{\rm H}}\right)\left(\frac{GM^2}{R}\right)^{-1} \approx 10^{-2}\left(\frac{M}{10^5\,M_\odot}\right)^{-1}\left(\frac{R}{25\,\mathrm{pc}}\right)\left(\frac{T}{15\,\mathrm{K}}\right) \,, \tag{1.2}$$

where μ is the gas mean molecular weight, $m_{\rm H}$ the hydrogen atom mass, $k_{\rm B}$ the Boltzmann constant, and G the gravitational constant. Eq. 1.2 shows that for the typical physical conditions of molecular clouds, thermal support is significantly smaller than the gravitational pressure, and that they should collapse converting all the available gas into stars. The time-scale of this process can be approximated with the free-fall time $\tau_{\rm ff}$, i.e. the time needed for a pressure-less homogenous sphere of density ρ to collapse into a point:

$$\tau_{\rm ff} = \sqrt{\frac{3\pi}{32G\rho}} \approx 10^6\,\mathrm{yr}\left(\frac{n}{10^3\,\mathrm{cm}^{-3}}\right)^{-\frac{1}{2}} \,. \tag{1.3}$$

However, already Zuckerman & Palmer (1974) noted that if molecular clouds collapsed at free-fall velocity, the Milky Way star formation rate should be one order of magnitude higher than the observed one, which is $\approx 1\,M_\odot/\mathrm{yr}$ (Robitaille & Whitney 2010). Moreover, observations of GMCs suggest that they are long-living structures, with longer ages than $\tau_{\rm ff}$. The star formation efficiency is therefore significantly lower than what expected from the balance of thermal motions and gravity only. This hints that other forces are present to hinder the gravitational pull. Indeed, a more complete version of the virial theorem, in case of equilibrium, reads:

$$2U + \Omega + 2K + \mathscr{M} = 0 \,, \tag{1.4}$$

where now also the contributions of non-thermal motions (K) and magnetic field pressure ($\mathscr{M}$) are taken into account. The first term comprises both bulk motions, such as rotation, and turbulence. To estimate its importance, we define V the average speed of the non-thermal motions.

Then:

$$\frac{2K}{|\Omega|} \approx \left(2 \times \frac{MV^2}{2}\right)\left(\frac{GM^2}{R}\right)^{-1} \approx 1.5\left(\frac{M}{10^5\,M_\odot}\right)^{-1}\left(\frac{R}{25\,\mathrm{pc}}\right)\left(\frac{V}{5\,\mathrm{km\,s^{-1}}}\right)^2 , \tag{1.5}$$

where for the average speed we used a typical value of velocity dispersion obtained via molecular spectroscopic observations[3] (see for instance Solomon et al. 1987).

Since magnetic fields are ubiquitous in the Galaxy (see §1.5 for more details), we must include the magnetic energy term $\mathscr{M}$ in the virial theorem. A uniform magnetic field with strength B carries the energy density $\Phi_{\mathrm{dens}} = B^2/8\pi$. Therefore one can derive:

$$\frac{\mathscr{M}}{|\Omega|} \approx \left(\frac{B^2}{8\pi} \times \frac{4\pi R^3}{3}\right)\left(\frac{GM^2}{R}\right)^{-1} \approx 0.4\left(\frac{M}{10^5\,M_\odot}\right)^{-2}\left(\frac{R}{25\,\mathrm{pc}}\right)^4\left(\frac{B}{20\,\mu\mathrm{G}}\right)^2 . \tag{1.6}$$

In Eq. 1.6 we used a typical value for the magnetic field strength observed in clouds with the Zeeman effect (Crutcher et al. 2010). The magnetic field properties in the ISM will be presented in more details in §1.5.

Equations 1.5 and 1.6 show that the gas motions related to non-thermic effects and the magnetic fields can provide pressure terms comparable to the gravitational one, and can thus sustain GMCs (and more in general molecular clouds) in an equilibrium state.

1.1.2 Jeans mass and fragmentation

Let us assume to have a homogeneous spherical source of volume density n and temperature T. Which is the maximum size it can sustain before collapsing? The Jeans theory, developed by Sir J. H. Jeans at the beginning of the XX century, focuses precisely on this question. It defines the Jeans mass and length as the critical values that allow the source to be in equilibrium. There are a number of ways to derive these quantities, and a straightforward approach is based on the virial theorem in its simplest form (Eq. 1.1). In the equilibrium case:

$$2U = |\Omega| \quad \rightarrow \quad Mc_\mathrm{s}^2 = G\frac{M^2}{R} \quad \rightarrow \quad \frac{k_\mathrm{B}T}{\mu m_\mathrm{H}} = G\frac{M}{R} , \tag{1.7}$$

in which we expressed the thermal energy content in terms of the isothermal sonic speed c_s. Given the relation between M, R, and the density n, one can easily solve for the Jeans mass (M_J) and length (λ_J):

$$M_\mathrm{J} \propto T^{\frac{3}{2}} n^{-\frac{1}{2}} \approx 2\,M_\odot \left(\frac{T}{15\,\mathrm{K}}\right)^{\frac{3}{2}}\left(\frac{n}{10^3\,\mathrm{cm^{-3}}}\right)^{-\frac{1}{2}} , \tag{1.8}$$

$$\lambda_\mathrm{J} \propto \left(\frac{M_\mathrm{J}}{\mu m_\mathrm{H} n}\right)^{\frac{1}{3}} \approx 0.3\,\mathrm{pc}\left(\frac{T}{15\,\mathrm{K}}\right)^{\frac{1}{2}}\left(\frac{n}{10^3\,\mathrm{cm^{-3}}}\right)^{-\frac{1}{2}} . \tag{1.9}$$

[3]The velocity dispersion of a molecular line in principle is due to both thermal and non-thermal motions of the gas. However, the first contribution cannot be larger than the gas sonic speed, which for temperatures of $10 - 30\,\mathrm{K}$ is $< 0.5\,\mathrm{km\,s^{-1}}$, thus negligible with respect to the observed velocity dispersion values.

Equation 1.8 and 1.9 state respectively the maximum mass and size that a source with given temperature and density can have to maintain the balance between thermal pressure and gravitational pull. It is interesting to notice that for typical molecular clouds these values are much smaller than the observed ones. This suggests —as previously noticed— that if no other source of pressure is present, the cloud should collapse in a free-fall time. On the other hand, small cores within molecular clouds have masses of $1-10\,M_\odot$ and sizes of $0.1-1.0\,\mathrm{pc}$, which equal the Jeans quantities for $T \approx 10\,\mathrm{K}$ and $n \approx 10^4\,\mathrm{cm}^{-3}$. At these small scales, hence, the thermal motions of the gas can prevent the gravitational contraction. These cores are defined *starless* when they do not host a central object. When they are also gravitationally bound, they are called *prestellar* (Ward-Thompson et al. 1999). Prestellar cores are hence the birthplaces of low-mass stars. They are cold ($T \approx 5-7\,\mathrm{K}$ at the centre) and dense (peak density $n \approx 10^{5-6}\,\mathrm{cm}^{-3}$) fragments of molecular clouds which are on the verge of gravitational collapse.

The Jeans equations yield further insights on the stability of clouds and cores. First of all, the Jeans mass decreases with lowering temperatures, which means that the colder the cloud, the easier the collapse. Furthermore, for a constant temperature value, M_J decreases when the density rises. When the gravitational collapse starts, the gas is still diffuse enough that the heating caused by the contraction can be immediately irradiated away: the first stage of the process is quasi-isothermal. This means that the mass limit for the stability becomes smaller and smaller, leading to the fragmentation of the cloud in cores. At a certain point, however, the density grows high enough ($\rho \gtrsim 10^{-13}\,\mathrm{g\,cm}^{-3}$) that photons are trapped in the gas that cannot cool anymore. The fragmentation process is then halted, and a *first hydrostatic core* is formed. The collapse now happens adiabatically in a quasi-equilibrium regime, until the temperature reaches $\approx 2000\,\mathrm{K}$. Then, the H_2 molecules start to dissociate, a process which is endothermic, absorbing the heat of the collapse. In this phase, the contraction is again approximately isothermal, and the thermal energy is not enough to balance the gravitational force. When the gas is completely in atomic form, it begins to heat up, giving rise to a second quasi-equilibrium phase. Then a central object, called *protostar*, finally forms.

1.1.3 Low-mass protostars

At the present day, the theory of low-mass star formation is far more detailed and complete than its high-mass counterpart, mainly due to the advantages it carries from the observational point of view. First of all, low-mass stars are far more frequent. The stellar initial mass function (IMF) greatly favours objects with less than one solar mass. As a consequence, their progenitors, also known as *young stellar objects* (YSOs), are more frequent. This means that we can observe more objects, and also that statistically there are more of them closer to the Solar System with respect to high-mass protostars. Furthermore, the evolutionary timescales concerning star evolution are inversely proportional to the stellar mass. For instance, the protostellar phase lasts $\gtrsim 10\,\mathrm{Myr}$ for Sun-like stars, while for a $10\,M_\odot$ it lasts less than a million year. Hence, low-mass objects are long-lived. This allowed to investigate their protostellar phase with great detail, and to distinguish different evolutionary stages (see Figure 1.2).

The initial stage, called Class 0, is characterised by the fact that the object is still deeply embedded in a dense envelope, which is heated by the material accreting onto the protostars

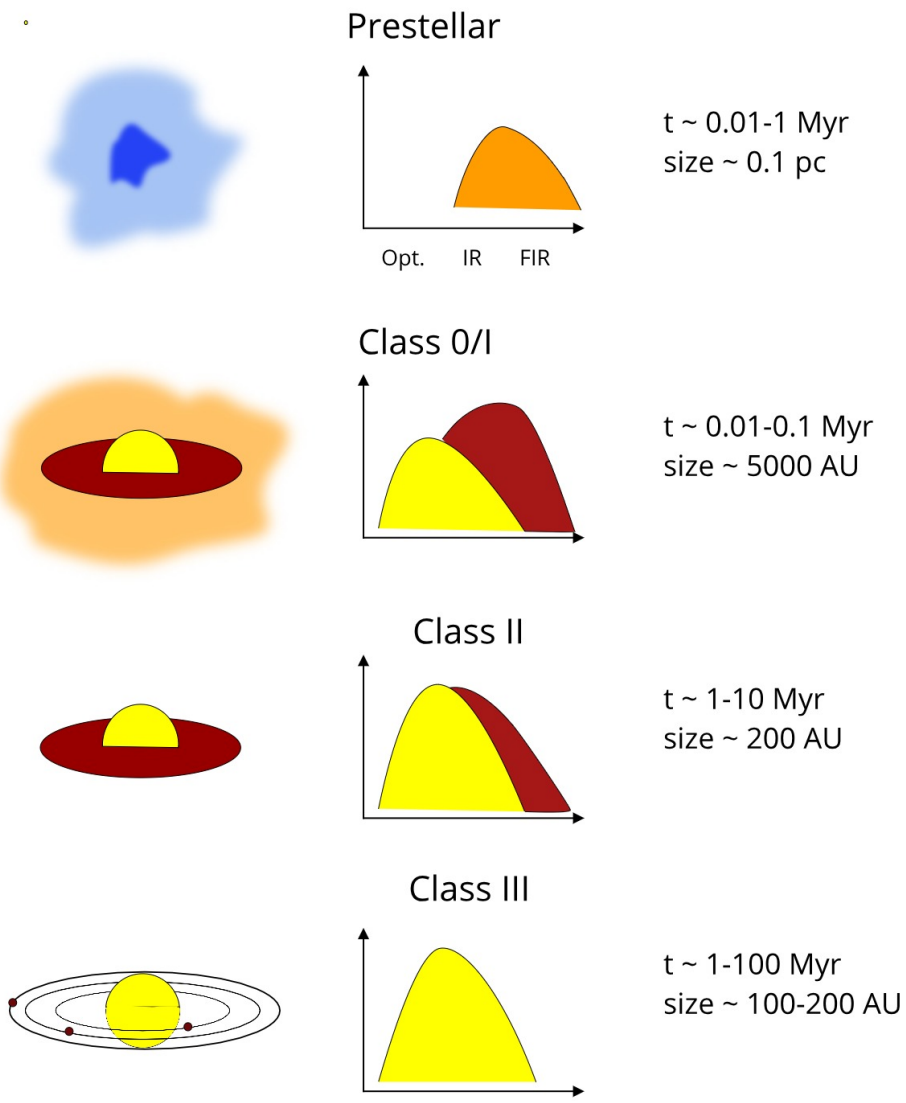

Figure 1.2: Schematic draw of the different stages of low-mass objects (on the left), together with their typical SEDs (central panel). Approximative durations and sizes of each stage are reported on the right. The time evolves from top to bottom. Figure based mainly on André et al. (2000).

and re-emits this energy at far infrared wavelengths. The arising spectral energy distribution (SED) is dominated by this IR excess. In this phase, the envelope mass is still larger then the stellar one ($M_{\rm env} > M_*$). As material is cleared from the envelope, the black-body emission from the protostar starts to become more important: this is the so-called Class I stage. In Class II objects, accretion flows and feedbacks from the central source (such as outflows) have removed the envelope completely. The infrared excess which is still visible in the SED is due to the

protoplanetary disc. The central object, from now on called a pre-main sequence star, is optically visible. In the low-mass end ($M < 2\,M_\odot$), this phase corresponds to the observational category of classic T-Tauri stars (CTTSs). Eventually, also the disc is cleared of most its material, leaving a formed protoplanetary system (Class III). Weak T-Tauri objects (WTTSs) belong to this stage.

1.2 The gas component of molecular clouds

Right after the primordial nucleosynthesis, within a few tens of minutes after the Big Bang, hydrogen atoms ($^1_1$H) accounted for 75% of the total mass, and elements heavier then helium (generically called *metals* in astronomy) represented only the 0.01%. During their lifecycle, stars produce energy via nuclear fusion, thus forming heavier elements, which can later on be redistributed in the interstellar medium through stellar wind or, more catastrophically, through supernovae explosions. In the proto-Sun, which formed from an already metal-enriched environment, the mass fraction of metals is $\approx 1.4\%$ (Asplund et al. 2009). Hydrogen is however still the most abundant element in the present ISM, and as a consequence H_2 is by far the most abundant molecule in molecular clouds. However, as we will illustrate, the physical conditions in the cold and dense gas do not excite efficiently any transition of H_2, which thus remains invisible to us.

The second most abundant component of molecular clouds is carbon monoxide (CO), which typically has an abundance[4] of $X_{\rm CO} \approx 10^{-4}$ (see for instance Bolatto et al. 2013, and references therein). Due to its energy level structure, in the cold gas it emits efficiently through its rotational spectrum. It also represents the most efficient coolant in molecular gas, allowing the first phases of the gravitational collapse to be isothermal.

Shielded by the strong interstellar UV field, the interior parts of molecular clouds represent a safe environment for several other molecules to form. Astrochemistry is the field of astronomy that studies these processes, with the aim of understanding the mutual interaction between the physical properties of collapsing cores and their chemical complexity. Furthermore, the analysis of molecular emission can provide a wealth of physical information, such as the gas kinematics, its density and its temperature. The following subsections are dedicated to understand how to relate these quantities with the observable ones.

1.2.1 Line emission and the two-level system

Molecules emit through three main kinds of transitions: electronic, vibrational and rotational. The first type requires excitation energy E of typically 1 eV, which corresponds to $\lambda \approx 1\,\mu$m, thus emitting lines in the optical/ultraviolet spectrum. Vibrational states have a separation of ≈ 0.1 eV, corresponding to the infrared wavelengths. Finally, the rotational spectrum is characterised by $E \approx 10^{-3}$ eV, which means that it emits lines in the microwave/radio regime. In the ISM, molecules are excited through collision, and thus the energy budget available for the excitation roughly corresponds to the gas thermal energy. Since a temperature of $T \approx 15$ K trans-

[4]We define the *abundance* of a molecule ($X_{\rm mol}$) as the ratio of its volume or column density with respect to molecular hydrogen.

lates in $E \approx 1.3 \times 10^{-3}$ eV, in cold clouds the molecular emission is mainly due to rotational (or ro-vibrational) transitions.

For the sake of simplicity, we now consider a system formed by only two states, labeled u and l, separated by the energy ΔE_{ul}. Their populations are regulated by the Boltzmann equation:

$$\frac{n_u}{n_l} = \frac{g_u}{g_l} \exp\left(-\frac{\Delta E_{ul}}{k_B T_{ex}}\right) , \tag{1.10}$$

where g_i is the statistic weight of the $i-$state, and T_{ex} is the transition excitation temperature. The possible transitions among these levels are:

1. spontaneous emission of a photon, with consequent decay from the upper state to the lower one, with a rate described by the Einstein coefficient A_{ul};
2. stimulated emission of a photon, depending on the external radiation field $\overline{J}$, described by the Einstein coefficient B_{ul};
3. spontaneous absorption of a photon, corresponding to the transition from state l to u. Its rate can be written as $B_{lu}\overline{J}$;
4. collisions with other gas particles, which can cause transitions in both directions, described by the rate coefficients γ_{lu} and γ_{ul}.

The radiative processes (1-2) result in the emission of photons with a frequency $\overline{\nu} = E_{ul}/h$. They are characterised by an emissivity j_ν, which represents the energy density per unit of time, frequency and solid angle. For example, for the spontaneous emission of photons this is:

$$j_\nu = \frac{h\overline{\nu}}{4\pi} n_u A_{ul} \phi(\nu) \tag{1.11}$$

where the line-shape function $\phi(\nu)$ describes the probability of emission of a photon at the frequency ν. It is normalised ($\int \phi(\nu)\, d\nu = 1$) and strongly peaked around the line centre frequency ($\overline{\nu}$). The factor $1/4\pi$ derives from the assumption of radiation isotropy on the solid angle.

If the system is in equilibrium, the populations of the two states must be constant, and therefore the total rate of transitions from the upper to the lower state must equal the rate of the inverse process. Therefore:

$$\gamma_{lu} n_{gas} n_l + B_{lu}\overline{J} n_l = \gamma_{ul} n_{gas} n_u + B_{ul}\overline{J} n_u + A_{ul} n_u \tag{1.12}$$

Two special cases of Eq. 1.12 are represented by systems where collisional processes and radiative ones are negligible, respectively. Analysing these conditions, one can demonstrate that the following relations hold:

$$\frac{B_{ul}}{B_{lu}} = \frac{g_l}{g_u} , \tag{1.13}$$

$$\frac{A_{ul}}{B_{ul}} = \frac{2h\overline{\nu}^3}{c^2} , \tag{1.14}$$

$$\frac{\gamma_{ul}}{\gamma_{lu}} = \frac{g_u}{g_l} \exp\left(-\frac{\Delta E_{ul}}{k_B T_{ex}}\right) . \tag{1.15}$$

These equations link the Einstein and the collisional coefficients to the system physical properties, such as the statistical weights, the transition frequency $\overline{\nu}$, and the excitation temperature.

1.2.2 Radiative transfer of lines

We now want to understand the propagation of radiation through the material present along the line-of-sight (los) to the observer, with particular attention to molecular line emission. To this aim, let us assume to have a slab of material in a molecular cloud of length ds, which partially absorbs the background radiation I_ν (specific intensity), and in turn emits photons with an emissivity j_ν at the frequency ν (see Figure 1.3 for a visual description). The mathematical expression of the arising emission is described by the *radiative transfer equation*, which reads:

$$\frac{dI_\nu}{ds} = -\rho\kappa_\nu I_\nu + j_\nu \ . \tag{1.16}$$

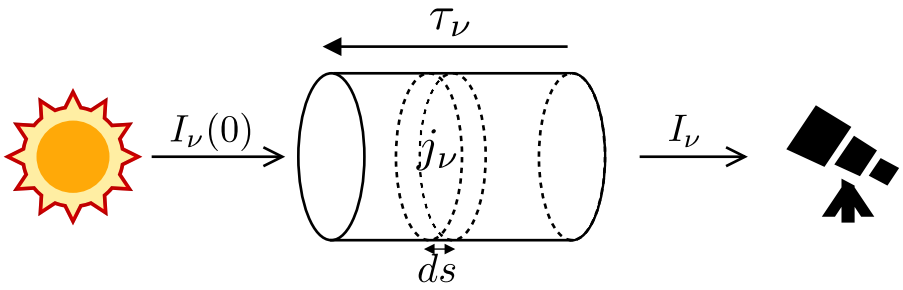

Figure 1.3: Schematic view of the passage of photons through the interstellar medium. The infinitesimal slab ds absorbs the background radiation $I_\nu(0)$ and emits according to its emissivity j_ν. The direction of increasing optical depth is also indicated.

In the right-hand side of the Eq. 1.16, the absorption term depends on the medium density ρ and on the *absorption coefficient per unit of total mass* κ_ν, measured in $\mathrm{cm^2\,g^{-1}}$. The *optical depth* is the integration of the absorption coefficient (or *opacity*) over the line of sight:

$$\tau_\nu = \int_{\mathrm{los}} \rho\kappa_\nu \, ds \ , \tag{1.17}$$

where the integral is computed along the line-of-sight going from the observer to the source. With some little algebra, and introducing the *source function* $S_\nu = j_\nu/\kappa_\nu$, it is easy to integrate Eq. 1.16 in the form:

$$I_\nu = I_\nu(0)e^{-\tau_\nu} + \int_0^{\tau_\nu} S_\nu(\tau'_\nu)\mathrm{e}^{-(\tau_\nu-\tau'_\nu)}\, d\tau'_\nu \ . \tag{1.18}$$

This equation describes the emission of both continuum and line radiation, but we will now focus on the latter. If we assume that the source function is the black-body radiation $B_\nu(T)$ at the

excitation temperature temperature $T_{\rm ex}$, and that the latter is constant along the line of site, Eq. 1.18 becomes:

$$I_\nu = I_\nu(0)\mathrm{e}^{-\tau_\nu} + B_\nu(T_{\rm ex})\left[1-\mathrm{e}^{-\tau_\nu}\right] \ . \tag{1.19}$$

When observing molecular lines, one is mainly interested in the difference between I_ν and the background intensity:

$$\Delta I_\nu = I_\nu - I_\nu(0) = (B_\nu(T_{\rm ex}) - I_\nu(0))\left[1-\mathrm{e}^{-\tau_\nu}\right] = \Big(B_\nu(T_{\rm ex}) - B_\nu(T_{\rm bg})\Big)\left[1-\mathrm{e}^{-\tau_\nu}\right] \ , \tag{1.20}$$

where we have assumed that the background intensity is the cosmic background radiation (CMB), a black-body emission at the temperature $T_{\rm bg} = 2.73\,\mathrm{K}$. Usually, the quantity ΔI_ν is converted into a temperature scale introducing the concept of brightness temperature $T_{\rm B}$:

$$T_{\rm B} = \frac{c^2}{2k_{\rm B}\nu^2}\Delta I_\nu \ . \tag{1.21}$$

$T_{\rm B}$ represents the equivalent temperature that a black-body would have in order to emit the radiation intensity ΔI_ν. Inserting the above definition of brightness temperature in Eq. 1.20, we can arrive to the *detection equation*:

$$T_{\rm B} = \Big(J_\nu(T_{\rm ex}) - J_\nu(T_{\rm bg})\Big)\left[1-\mathrm{e}^{-\tau_\nu}\right] \ , \tag{1.22}$$

to derive which we have introduce the function $J_\nu(T)$ for the sake of simplicity:

$$J_\nu(T) = \frac{h\nu}{k_{\rm B}}\frac{1}{\mathrm{e}^{\frac{h\nu}{k_{\rm B}T}}-1} \ . \tag{1.23}$$

If the source size is smaller than the beam one, Eq. 1.22 must be corrected for the beam filling factor ($\eta_{\rm bf}$).

Eq. 1.22 describes the signal of a line emitted by a molecule with excitation temperature $T_{\rm ex}$ and optical depth τ_ν. The optical depth is clearly related to the density of the emitting material, but how exactly? To answer this question, we have to recall the concepts introduced in the study of the two-level system (§1.2.1). The *absorption coefficient* of the transition ($\alpha_\nu = \rho\kappa_\nu$) is caused by two processes: the spontaneous absorption and the stimulated emission, which can be considered a negative form of absorption. Hence we can write:

$$\alpha_\nu = \frac{h\bar{\nu}}{4\pi}\left(B_{lu}n_l - B_{ul}n_u\right)\phi(\nu) = \frac{h\bar{\nu}}{4\pi}\phi(\nu)n_uA_{ul}\frac{c^2}{2h\bar{\nu}^3}\left[\exp\left(\frac{\Delta E_{ul}}{k_{\rm B}T_{\rm ex}}\right)-1\right] , \tag{1.24}$$

where we have made use of Eqs. 1.13-1.15. This equation relates the absorption coefficient of a specific line to the population of the upper state n_u. This is in turn linked to the total density $n_{\rm mol}$ of the molecule, which considers the populations of all the energetic levels, through the partition function Q:

$$\frac{n_u}{n_{\rm mol}} = \frac{g_u}{Q}\exp\left(-\frac{E_u}{k_{\rm B}T_{\rm ex}}\right) , \tag{1.25}$$

where E_u is the energy of the upper state with respect to the fundamental one. We can now relate the optical depth to the total molecular column density:

$$\tau_\nu = \int_{\rm los} \alpha_\nu \, ds = \frac{A_{ul} c^2}{8\pi\bar{\nu}^2} \frac{g_u}{Q} \exp\left(\frac{E_u}{k_{\rm B} T_{\rm ex}}\right) \left[\exp\left(-\frac{h\bar{\nu}}{k_{\rm B} T_{\rm ex}} - 1\right)\right] \phi(v) N_{\rm mol} \ , \tag{1.26}$$

The observer can then invert Eq 1.22 to obtain τ_ν from the observations, and then use Eq. 1.26 to derive the molecular column density, if the excitation temperature is known. A simple case is when the line is optically thin, which is verified for $\tau_\nu \ll 1$: in this case it is easy to demonstrate that the *integrated intensity* of the line, defined as the integral of the brightness temperature in the velocity v:

$$W = \int_v T_{\rm B}(v) \, dv \ , \tag{1.27}$$

is directly proportional to the column density (Caselli et al. 2002c):

$$N_{\rm mol} = W \frac{8\pi\bar{\nu}^3 Q}{c^3 g_u A_{ul}} \frac{1}{\exp\left(\frac{h\bar{\nu}}{k_{\rm B} T_{\rm ex}}\right) - 1} \frac{1}{J_\nu(T_{\rm ex}) - J_\nu(T_{\rm bg})} \exp\left(\frac{E_u}{k_{\rm B} T_{\rm ex}}\right) \ . \tag{1.28}$$

Eq. 1.28 allows to derive the molecular column density from the observation of a spectral line, once its spectroscopic parameters (frequency, Einstein coefficients,...) are known. To do so, however, one must know also the excitation temperature, which is not directly derivable. A possible method consists of assuming that $T_{\rm ex}$ is equal to the gas or dust temperature. Another widely used approach involves observing several lines of the same molecule. Under the assumption that they all share the same $T_{\rm ex}$, one can derive simultaneously $T_{\rm ex}$ and $N_{\rm mol}$ fitting the observed data. This approach, which is often refereed to as local-thermodynamic-equilibrium (LTE) method[5], presents however strong limitations, as it will be shown in Chapter 3.

1.3 Fractionation processes

All elements in the Universe have usually more than one stable isotope[6]. The abundances of the rarer isotopes with respect to the main ones, called *isotopic ratios*, are characterised by universal elemental values. In most cases, these values are set either by the primordial nucleosynthesis, right after the Big Bang, or by the nuclear reactions in stars interiors. In molecular clouds, there are no processes energetic enough to alter the overall isotopic content, since nuclear reactions are required. Only on long timescales, when the material locked into stars is returned to the ISM via winds or supernovae explosions, the relative abundances of isotopes can change. Therefore, at least locally in time and space, each isotopic ratio is characterised by a reference value. In Table 1.1 we report the elemental values for the isotopic ratios of the most abundant metals in

[5]We highlight that this denomination, which is nevertheless widely used, is actually incorrect. In a proper LTE analysis, one assumes that all the lines share the same $T_{\rm ex}$, and that this is also equal to the gas kinetic temperature ($T_{\rm K}$). In many works, however, the further assumption $T_{\rm ex} = T_{\rm K}$ is not made.

[6]In this work, we only focus on stable atoms, despite recognising that radioactive isotopes and their decays can play significant role in different astrophysical phenomena.

Table 1.1: Elemental values for the isotopic ratios of abundant elements in the Solar System or in the local ISM.

Ratio	Value	Position	Reference
D/H	$(1.56 \pm 0.04) \times 10^{-5}$	Local Bubble[a]	Linsky et al. (2006)
$^{14}N/^{15}N$	441 ± 5	Solar wind	Marty et al. (2011)
$^{12}C/^{13}C$	68 ± 15	Local ISM	Milam et al. (2005)
$^{16}O/^{18}O$	557 ± 30	Local ISM	Wilson (1999)
$^{18}O/^{17}O$	3.2 ± 0.2	Local ISM	Penzias (1981)

[a] The Local Bubble is a structure in the interstellar medium, containing also the Solar System, with a lower density with respect to the average one. Its extension is ≈ 100 pc.

the local ISM. If one took into account all the possible forms of a given element —which in a molecular clouds are all the molecules bearing that element—, these are the values that would be observed. Chemical reactions can however alter the isotopic ratio of individual molecular species, a process known as *fractionation*. This is often driven by the fact that the isotopologues of the same molecule have different zero-point energy, since isotopes differ both by mass and by atomic spin. Molecules with different isotopic compositions with respect to one or more atoms are known as *isotopologues*. For example, H_2O and HDO or CO and $^{13}C^{18}O$ are isotopologues of water and carbon monoxide, respectively.

In the last few decades, isotopic fractionation has raised a great interest in the context of star formation, since it is believed to be a good diagnostic tool to follow the different evolutionary stages of this process, with the ultimate goal of understanding also the origin of our own Solar System (see for instance the review on hydrogen fractionation from Ceccarelli et al. 2014). The underlaying idea is that fractionation only happens in peculiar physical conditions, and once a material is formed it preserves the isotopic composition it had at the moment of its formation. This hence allows us to trace back its origin. Studying the isotopic ratios of prestellar and protostellar sources, and comparing them with those of the Solar System bodies, can therefore help us answering some key questions about when and where our planetary system inherited its composition.

The recent increase in the interest for fractionation processes is also due to the improved observational capabilities, which have made these studies possible. In fact, molecules bearing rare isotopes have usually faint emissions (even though this is not the case for deuterated species, as we will describe), and thus their detection requires high sensitivity. This is achieved by building large single dish radio telescopes, such as the Green Bank Telescope (GBT) in North-America or the 30m IRAM (Institut de Radioastronomie Millimétrique) antenna in Spain, and radio interferometers, the most powerful being the Atacama Large Millimeter and sub-millimeter Array (ALMA, see Figure 1.4). At the same time, revolutionary space missions such as Rosetta, which brought a lander on the surface of the comet 67P/Churyumov-Gerasimenko, allowed to measure

in-situ the isotopic ratio of a pristine Solar System body.

Figure 1.4: The view of the night sky over the ALMA telescope in the Chajnantor plateau, Chile. With its current 53 working antennas, it is the largest and most sensitive telescope in the world for millimetre and submillimetre observations. Credit: ESO/B. Tafreshi.

1.3.1 Deuteration

The fractionation of hydrogen with respect to its only stable isotope, deuterium, is also known as deuteration. Deuterium is one of the few light elements that were produced during the primordial nucleosynthesis, with an abundance relative to hydrogen $D/H_{prim} = (2.5 - 2.8) \times 10^{-5}$ (see, for instance, Spergel et al. 2003; Sánchez et al. 2006). In the gas in the Solar neighbourhood, the observed elemental value is $D/H = 1.6 \times 10^{-5}$, which is lower than D/H_{prim} due to depletion onto dust grains and to astration (Linsky et al. 2007). However, observations performed in different parts of the ISM and within the Solar System unveiled that some molecules are enriched in deuterium up to four orders of magnitude more with respect to the elemental value, as shown in Figure 1.5. In particular, the measured value for the evaporated ocean waters is 1.5×10^{-4} (this is also known as the Vienna Standard Mean Ocean Water, or VSMOW, Lecuyer et al. 1998). Interestingly, the Rosetta space mission reported $D/H = (5.3 \pm 0.7) \times 10^{-4}$ in the water present in the coma of the comet 67P, which is only three times larger than the VSMOW (Altwegg et al. 2015). In general, the deuteration level of meteorites and comets is heterogeneous, with some parts of carbonaceous chondrites[7] —known as *deuterium hot spots*— showing values as large as 1.5×10^{-2} (Gourier et al. 2008). In prestellar sources, the measured deuteration levels are among the highest found in the ISM, with some molecules (especially nitriles) exhibiting $D/H \approx 0.1 - 0.5$ (see e.g. Crapsi et al. 2005; Pagani et al. 2007).

The reason for these extreme deuteration levels has to be found in that prestellar cores host the ideal physical conditions for this kind of fractionation to be very efficient, as studied in detail by Ceccarelli et al. (2014). In the cold gas, deuteration starts with the formation of protonated molecular hydrogen (H_3^+), due to cosmic ray ionisation of H_2. This is followed by the formation of H_2D^+, according to the exothermic reaction:

$$H_3^+ + HD \leftrightharpoons H_2D^+ + H_2 + 230\,K\,. \tag{1.29}$$

[7]Carbonaceous chondrites are a form of non-metallic meteorites. They represent some of the most pristine materials found in the nowadays Solar System.

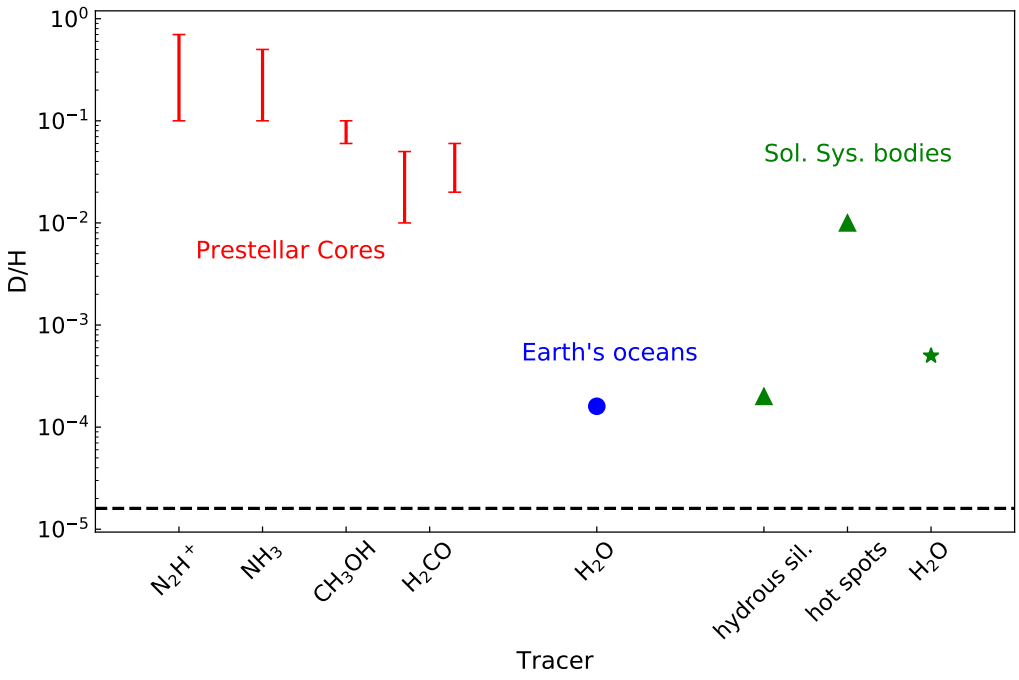

Figure 1.5: A summary of some representative measurements of the D/H values from literature, divided by molecular tracer or material type (for meteorites). The horizontal dashed line corresponds to the elemental value. References for the prestellar cores (in red): Crapsi et al. (2005); Pagani et al. (2007); Bizzocchi et al. (2014); Chacón-Tanarro et al. (2019). Earth's ocean value (in blue): Lecuyer et al. (1998). Meteorites (green triangles): Gourier et al. (2008); Remusat et al. (2009). Comet 67P (green star): Altwegg et al. (2015).

Its reverse reaction, which destroys H_2D^+, has a small energetic barrier that cannot be overcome when the temperature is $\lesssim 15$ K. Therefore, the deuterium fraction of H_3^+ becomes larger than the elemental value. Following processes similar to reaction 1.29, also HD_2^+ and D_3^+ are formed.

The formation of all other deuterated molecules is triggered by these ions. In the gas phase, the dominant processes are ion-neutral isotope exchange reactions, such as:

$$H_2D^+ + N_2 \leftrightharpoons N_2D^+ + H_2\,. \tag{1.30}$$

At the same time, the deuterated forms of H_3^+ can produce deuterium in atomic form via dissociative recombination with free electrons. The D atoms then stick onto the dust grains (see §1.4.3 for more details), where they can react with molecules in the ice mantles (e.g. water or ammonia).

The main process that limits deuteration is the destruction of H_2D^+ (and in general H_3^+ isotopologues), which is mainly due to the reaction with carbon monoxide, producing HCO^+ (Dalgarno & Lepp 1984). Another key factor that can affect deuteration is the ortho-to-para[8] ratio

[8]Molecular hydrogen is present in two forms, according to the relative direction of the spins of the H atoms: when they are in the same direction, the molecule is called ortho-H_2, while in para-H_2 the spins point in opposite directions.

of H_2 molecules. In fact, the zero-point energy (i.e. the lowest energetic level) of ortho-H_2 is ≈ 175 K higher than the one of para-H_2. This energy difference is enough to overcome the barrier of the $H_2D^+ + H_2 \rightarrow HD + H_3^+$ reaction, thus destroying H_2D^+. In prestellar cores, both these processes are heavily suppressed. In fact, at low temperature and high density, the CO molecules start to freeze onto dust grains and they deplete from the gas (see §1.4.3 for more details). In some objects, observational studies concluded that more than 90% of CO is removed from the gas phase (Caselli et al. 1999; Bacmann et al. 2002). Furthermore, the ortho-to-para ratio of H_2 is predicted to drop below 10^{-3} in prestellar objects (Sipilä et al. 2013), as deduced in the prototypical source L1544 (Kong et al. 2015). The low-mass prestellar phases hence host the ideal conditions to make deuteration a very efficient process, as demonstrated observationally.

1.3.2 Nitrogen fractionation

Nitrogen, the fifth element in the Universe in abundance, exists in two stable isotopic forms, ^{14}N (the main one) and the rarer ^{15}N. These isotopes are formed in the interiors of both low-mass and high-mass stars mainly through the CNO cycle, even though the exact production processes and their relative importance are still under debate (see e.g. Romano et al. 2017). As a consequence, also the expected isotopic relative abundance is still quite unclear (Pignatari et al. 2015). However, in the last few decades, nitrogen isotopic ratio $^{14}N/^{15}N$ has raised interest as an important diagnostic tool to follow the evolutionary process of different Solar System materials from the primordial phases up to present. Measurements performed in situ in the Solar wind by the Genesis mission concluded that the nitrogen isotopic ratio in the primitive Solar Nebula was $^{14}N/^{15}N = 440$ (Marty et al. 2011). This result is in well agreement with observations of the Jupiter atmosphere, where $^{14}N/^{15}N = 450$ was found (Fouchet et al. 2004). However, the molecular nitrogen in the terrestrial atmosphere is enriched in ^{15}N, since the measured isotopic ratio is 272 (Nier 1950). In general, many materials in the Solar System are fractionated, with some carbonaceous chondrites showing values as low as $^{14}N/^{15}N = 50$ (Bonal et al. 2010).

In the interstellar medium, measurements of the nitrogen isotopic ratio resulted in values spread on a wide range, depending both on the kind of analysed sources and on the molecular tracer. For instance, Gerin et al. (2009) found $^{14}N/^{15}N = 350 - 810$ using NH_3 in a sample of low-mass dense cores and protostars, whilst Bizzocchi et al. (2013) observed $^{14}N/^{15}N = 1000$ using diazenylium (N_2H^+) in the prototypical prestellar core L1544. On the other hand, nitriles (CN, HCN, and HNC) seem to be generally more enriched in ^{15}N with respect to the Protosolar Nebula, as shown by Hily-Blant et al. (2013) with HCN spectra in prestellar cores, resulting in isotopic ratios in the range $140 - 360$. A summary of the main observations of nitrogen isotopic ratio in low-mass sources is presented in Figure 1.6. In the high-mass regime, on the other hand, results are even more spread: Fontani et al. (2015) found $^{14}N/^{15}N = 180 - 1300$ in N_2H^+, and values in the range $250 - 650$ were reported in HCN and HNC by Colzi et al. (2018a).

From the theoretical point of view, we are still lacking a comprehensive model able to reproduce these observational results. The Protosolar value (440) is assumed to be valid in the local ISM, according to the most recent results (Colzi et al. 2018a,b), even though other works suggest a lower value for the elemental N-isotopic ratio in the solar neighbourhood (e.g. $^{14}N/^{15}N \approx 300$, Kahane et al. 2018, or $^{14}N/^{15}N \approx 330$, Hily-Blant et al. 2017). The ^{15}N-enrichment with respect

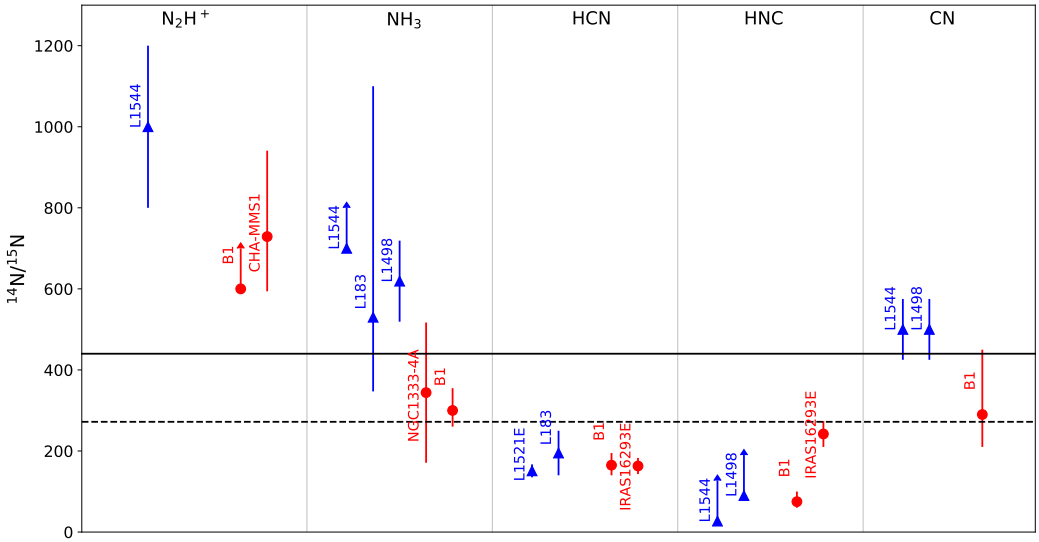

Figure 1.6: A summary of literature values of nitrogen isotopic ratios in low-mass prestellar (blue triangles) and protostellar (red dots) sources, divided by molecular tracer. The horizontal solid line corresponds to the Protosolar Nebula value, assumed to be valid also for the local ISM, while the dashed line represents the isotopic ration of molecular nitrogen in the Earth's atmosphere. Data from Wirström et al. (2016), and references therein.

to the elemental value exhibited by nitriles seems to be in agreement with recent chemical models (see e.g. Roueff et al. 2015). On the contrary, it is very difficult to explain the high isotopic ratios found in N_2H^+. The latter is a species of key interest, since it is directly produced from N_2, which is believed to be the main nitrogen reservoir in the cold molecular gas. However, it cannot be directly observed, and therefore N_2H^+ is usually considered a good proxy for the N_2 abundance. Terzieva & Herbst (2000) published the first chemical models about N-fractionation, and suggested that N_2H^+ should present a modest enrichment in ^{15}N through the reactions:

$$N_2H^+ + {}^{15}N \rightleftharpoons N^{15}NH^+ + N\,, \tag{1.31}$$

$$N_2H^+ + {}^{15}N \rightleftharpoons {}^{15}NNH^+ + N\,. \tag{1.32}$$

A further development of the chemical network made by Charnley and Rodgers led to the so-called *superfractionation* theory (Charnley & Rodgers 2002; Rodgers & Charnley 2008), according to which high enhancements in ^{15}N are expected in N_2H^+ (and also ammonia) when CO is depleted from the gas phase. Recently, however, based on ab initio calculations, Roueff et al. (2015) suggested that the reactions 1.31 and 1.32 do not occur in the cold environments due to the presence of an entrance barrier. As a consequence, no fractionation is expected and the $^{14}N/^{15}N$ ratio in diazenylium should be close to the elemental value. Nonetheless, none of these results is consistent with the anti-fractionation seen for instance in L1544 ($^{14}N/^{15}N$ = 1000). More recently, Wirström & Charnley (2018) included the newest rate coefficients from Roueff et al. (2015) in a chemical model that also takes into account spin-state reactions, but their predictions fail in reproducing both the depletion observed in N_2H^+ and the high fractionation measured in

HCN and HNC. It is therefore clear that more efforts are still needed both from the observational and the theoretical point of view in order to achieve a comprehensive understanding of nitrogen fractionation.

1.4 The interstellar dust

Approximately 1% of the ISM is composed by solid particles known as *interstellar dust grains*. It is still under debate which processes contribute to the formation of these grains. However, it is now widely accepted that the photospheres of evolved stars (especially cool carbon stars) and supernova explosions host dust formation, as observations have also confirmed[9]. In the star formation context, the study of interstellar dust is of crucial interest for many aspects. In particular, the coagulation of these particles into bigger and bigger bodies in the mid-plane of protoplanetary discs give birth to *planetesimals*, the first evolutionary step of planet formation.

Despite representing a small fraction of the total mass of the interstellar medium, dust grains play a key role in many astrophysical processes, due to their interactions both with radiation and with the gas-phase of the ISM. We will now briefly described some of these important phenomena.

1.4.1 Extinction

Dust grains interact with electromagnetic radiation mainly through absorption and scattering of photons. The combination of these two processes is known as *extinction*, the first observed phenomenon related to interstellar dust. In fact, extinction causes the background stellar radiation to be both attenuated and reddened. It is indeed studying the anomalous colours of stellar clusters that Trumpler conclusively discovered interstellar dust early in the XX century (Trumpler 1930).

The degree of extinction as a function of wavelength, also known as extinction in magnitude (A_λ), strongly depends on the dust characteristics, both in terms of chemical composition and of size distribution. It is customary to express it in terms of *total extinction*, this being the ratio between A_λ and the colour excess $E(B-V)$[10]. An example of extinction curves for the Milky Way is presented in Figure 1.7. As one can notice, the extinction becomes stronger at shorter wavelength, which causes the reddening of the radiation. The strong feature at $\lambda \approx 2175\,\text{Å}$ ($\approx 4.5\,\mu\text{m}^{-1}$) is due to the amorphous carbon composition of the dust grains.

1.4.2 Dust thermal emission

Dust grains emit thermal radiation as a consequence of the absorption of the background light field, and this emission can provide important information on the physical properties of the ISM, such as the dust temperature T_{dust} and the gas column density $N_{\text{mol}}(\text{H}_2)$. This thermal radiation,

[9] See the review from Sarangi et al. (2018) for a detailed description of dust formation pathways.

[10] Assuming to perform observations in the optical filters B and V, we define B and V the absolute magnitudes measured in the two bands. Then, the colour index is the quantity $B-V$. The colour excess is the difference between the observed colour index and the intrinsic one: $E(B-V) = (B-V)_{\text{obs}} - (B-V)_{\text{int}}$.

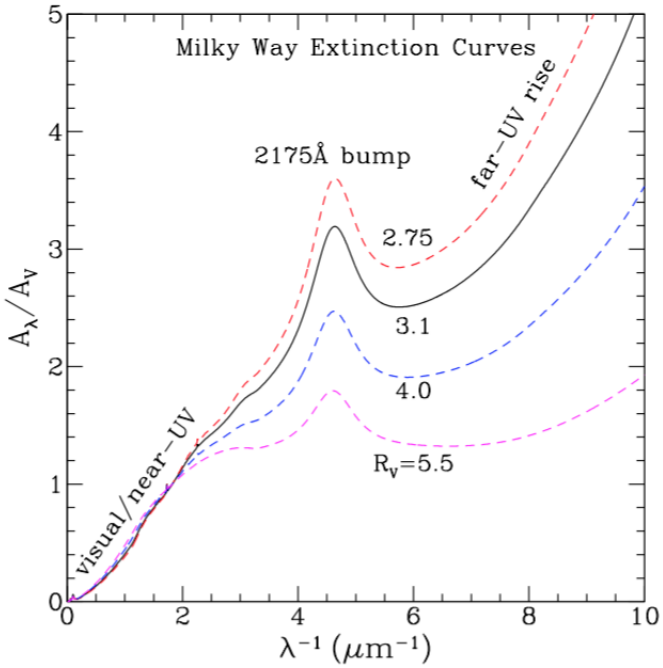

Figure 1.7: Extinction curves of the Milky Way as a function of different values of the parameter $R_V = A_V/E(B-V)$. The black curve corresponds to the Galactic average value $R_V = 3.1$. From Li (2008).

which also plays a fundamental role in the cooling of the ISM, can be understood in the framework of the radiative transfer analysis, in particular referring to Eq. 1.19, which we report here for conveniency:

$$I_\nu = B_\nu(T_{\rm dust})\left[1 - e^{-\tau_\nu}\right] \ , \tag{1.33}$$

where we have assumed for the sake of simplicity that the background radiation term $I_\nu(0)$ is negligible and that dust grains emit as a blackbody radiation at the temperature $T_{\rm dust}$. Eq. 1.33 describes the so-call *gray body* emission, which is a blackbody radiation modified by the factor $[1 - e^{-\tau_\nu}]$. A simplified version of it can be derived assuming optically thin conditions ($\tau_\nu \ll 1$). In this case it holds:

$$I_\nu \approx B_\nu(T_{\rm dust})\tau_\nu = \frac{2h\nu^3}{c^2}\frac{1}{\exp\left(\frac{h\nu}{k_{\rm B}T_{\rm dust}}\right) - 1}\tau_\nu \ . \tag{1.34}$$

Our goal is to relate the arising dust thermal emission to the amount of dust present on the line of sight. From this, assuming the relative abundance of dust to gas (the *gas-to-dust ratio*), we aim to derive the total gas column density:

$$N_{\rm mol}({\rm H_2}) = \int_{\rm los} n_{\rm H_2}\, ds = \int_{\rm los} \frac{\rho_{\rm H_2}}{\mu_{\rm H_2} m_{\rm H}}\, ds = \frac{\tau_\nu}{\mu_{\rm H_2} m_{\rm H} \kappa_\nu} \ , \tag{1.35}$$

where $m_{\rm H}$ is the hydrogen atom mass and $\mu_{\rm H_2}$ is the mean molecular weight per hydrogen molecule, which for typical values of hydrogen mass fraction ($X \approx 0.71$) is equal to 2.8 (Kauff-

mann et al. 2008). To derive the last right-hand side of Eq. 1.35, we have used that $d\tau_\nu = \rho k_\nu ds$ (definition of optical depth, Eq. 1.17). Combining Eqs. 1.34 and 1.35, one comes to:

$$N_{\rm mol}(H_2) = \frac{1}{\mu_{H_2} m_H \kappa_\nu} \frac{I_\nu}{B_\nu(T_{\rm dust})} \,. \tag{1.36}$$

It is important to highlight that in the last equation the opacity κ_ν takes into account the gas-to-dust ratio, for which a value commonly used is 100 (Hildebrand 1983). Eq 1.36 allows to derive the gas column density from the observed dust emission I_ν, once the dust temperature is known. Similarly to the considerations we illustrated for molecular lines, hence, $T_{\rm dust}$ and $N_{\rm mol}$ are degenerate parameters. An approach widely used to derive the dust temperature and column density at the same time consists in performing photometric observations of the thermal emission at multiple frequencies, and then to fit the data with the gray-body model. To this aim, it is usually assumed that the dust opacity κ_ν varies as a power-law with respect to the frequency:

$$\kappa_\nu = \kappa_{\nu_0} \left(\frac{\nu}{\nu_0} \right)^\beta \,, \tag{1.37}$$

where β, known as the *dust spectral index*, is a positive number, since the absorption is stronger at higher frequencies. In star-forming regions, usually adopted values are in the range $\beta = 1 - 2$ (Mezger et al. 1990; Walker et al. 1990; Chen et al. 2016; Chacón-Tanarro et al. 2017; Bracco et al. 2017). When inserting this expression in Eq. 1.33, one obtains that in the Rayleigh-Jeans regime ($h\nu \ll k_B T_{\rm dust}$) the modified black-body emission depends on the frequency as $I_\nu \propto \nu^{2+\beta}$, instead of $I_\nu \propto \nu^2$.

In molecular clouds, typical values for the dust temperature are in the range $10 - 20$ K. As a consequence, the peak of the emission is in the far-infrared range (hundreds of micrometers). The analysis of the dust thermal radiation is hence a powerful diagnostic probe of the ISM physical conditions, but this study can be performed observationally only from space, given the high opacity of the Earth's atmosphere at these frequencies (see also §1.6).

1.4.3 Dust and astrochemistry

Interstellar dust plays a fundamental role also in astrochemical processes. The core of grains is formed by refractory materials, mainly silicates or amorphous carbon. However, in the cold and dense environment of prestellar core, as a consequence of low-velocity encounters, molecules can stick onto the dust surfaces due to weak van der Waals or electrostatic forces. This process, known as *adsorption*, leads to the formation of ice mantles covering the refractory cores of grains. As a consequence, the interested molecule is depleted from the gas phase, sometimes to such an extent that its line emission becomes negligible. Molecular freeze-out therefore affects the observability of certain species.

All elements heavier than helium experience adsorption onto dust grains. However, observations suggest that some species are effected by depletion more than others. C- and O-bearing species seem extremely prone to this process. In prestellar cores, as already mentioned, most of carbon monoxide is depleted (Kramer et al. 1999; Caselli et al. 1999; Bacmann et al. 2002). On

the other hand, N-bearing species (especially nitrogen hydrides, such as N_2H^+ and NH_3) appears to remain in the gas phase also at very high-densities ($n \gtrsim 10^6\,\mathrm{cm}^{-3}$), as observationally found in the prestellar core L1544 (Crapsi et al. 2007). The probability that a molecule sticks onto dust grains is parametrised by the *sticking coefficient*. From the theoretical point of view, we still lack an explanation of the different behaviours of distinct species, especially due to very few available experimental studies on the gas-grain interaction.

Once locked into ices, molecules are still chemically active, which gives raise to a complex solid-state chemistry. In particular, light-particles —such as hydrogen atoms— have high mobility on the grain surfaces, mainly due to quantum-tunnelling effects. As a consequence, hydrogenation processes represent an important source for new species. The hydrogenation of CO, for instance, leads to the formation of methanol (CH_3OH) and formaldehyde (H_2CO).

Molecules can return to the gas phase through *desorption* mechanisms, which are due to a variety of processes. Thermal desorption happens when the temperature rises and the thermal energy available becomes larger than the molecular binding energy to the grain. In protostellar sources, where the activity of the central object heats the surrounding medium, mantle ices start to evaporate, and molecules are released back in the gas. Among the non-thermal mechanisms, the main ones are photo-desorption and chemical-desorption. The former, in dark environments, is due to the interaction of grains with UV photons produced by the reaction of H_2 molecules with cosmic rays (Leger et al. 1985). The latter involves exothermic chemical reactions in the ices which release enough energy for the molecular products to evaporate from the grains (see e.g. Takahashi & Williams 2000; Garrod et al. 2007). Finally, dust particles can be destroyed by sputtering in shocks.

1.5 Magnetic field in star forming regions

In 1949, the first observations of polarised starlight suggested the existence of a diffuse Galactic magnetic field (Hall 1949). We now know that magnetic fields (B) are ubiquitous in the interstellar medium, as the Planck mission unveiled and as shown in Figure 1.8. They therefore represent a fundamental ingredient for star formation, since they provide a source of pressure able to balance the gravitational pull. In fact, due to the Lorentz force, gas motions across the field lines are suppressed, and only those along the lines are allowed. This is the consequence of the magnetic tension, which acts against the compression of the B-field lines.

Magnetic fields exert a direct force only on charged particles. Although most of the ISM phases are neutral, even in the cold gas the ionisation fraction ($x(e)$, i.e. the abundance of free electrons, McKee 1989) is not null, due either to photoionisation at low visual extinction or to collisions with cosmic rays at high densities. Caselli et al. (1998) reported $\langle x(e)\rangle \approx 10^{-7}$ in a sample of low-mass dense cores, and similar results were found also in high-mass counterparts (Bergin et al. 1999). As a consequence of collisions between ions and neutrals, drag forces can transfer the influence of magnetic fields to the whole medium. The ionisation fraction is therefore a key parameter in the physics of molecular clouds, because it determines the degree of coupling between the gas and the field lines.

From the theoretical point of view, the exact role of magnetic fields and their relative impor-

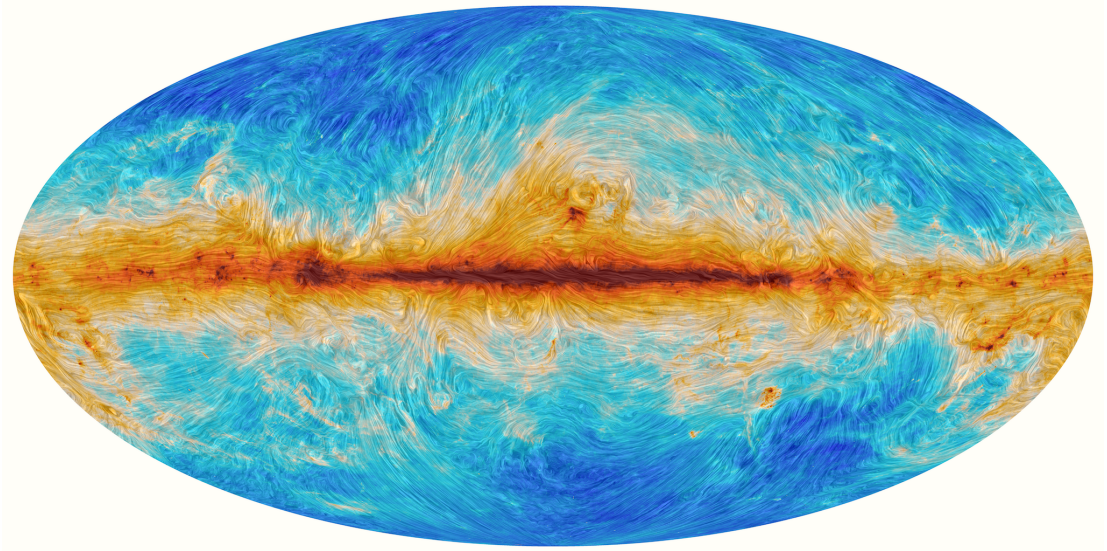

Figure 1.8: The galactic magnetic field as traced by the Planck satellite with observations of the polarised dust thermal emission at 353 GHz. Credit: ESA and the Planck Collaboration.

tance with respect to turbulence, another important force driving the star formation process, are points still under great debate (see for instance the review from Crutcher 2012; McKee & Ostriker 2007). Polarisation observations performed with the Planck telescope suggest that molecular clouds are threaded by ordered magnetic fields, preferentially aligned perpendicularly to the clouds' main axes (Planck Collaboration et al. 2016). In this configuration, *B*-fields regulate star formation more efficiently than turbulence (Mouschovias & Spitzer 1976; Nakamura & Li 2008; Li et al. 2013). Magneto-hydrodynamics theories distinguish two main models, the strong-field case (e.g. Fiedler & Mouschovias 1993) and the weak-field one (e.g. Mac Low & Klessen 2004). The difference between the two is linked to the mass-to-flux ratio (M/Φ), which defines the ratio between the gravitational energy and the magnetic one[11]. In particular, it is relevant to compare this quantity with its critical value $(M/\Phi)_{\rm cr} = 1/2\pi\sqrt{G}$ (Nakano & Nakamura 1978), introducing the parameter $R = (M/\Phi)/(M/\Phi)_{\rm cr}$. The condition $R > 1$ defines supercritical sources, where gravity is strong enough to overcome the magnetic pressure, while in the subcritical state ($R < 1$) the magnetic pressure and tension are enough to halt the contraction.

In the "classic" strong-field theory (see e.g. Mouschovias & Spitzer 1976; Allen et al. 2003), clouds are initially subcritical, and the magnetic field is frozen in the gas. However, due to the low ionisation fraction, neutrals begin to drift with respect to ions. This process, known as gravity-driven ambipolar diffusion, causes an increase of R, until eventually dense cores become supercritical. Initially the contraction happens preferentially along the field lines, forming a flattened structure (*pseudodisc*). However, the gravitational pull becomes strong enough to bend the field lines inwards, giving rise to a characteristic hourglass shape (see Figure 1.9). At the small scales of protostellar envelopes, magnetic fields are expected to be an effective way of removing

[11]The distinction between weak and strong *B*-fields is a blurred one. In most of theoretical works, weak fields are characterised by $R = 10$ or higher.

angular momentum from infalling and rotating material. This magnetic braking effect is very efficient in preventing the envelope fragmentation and the formation of large protoplanetary discs, as demonstrated by simulations performed for instance by Galli et al. (2006). Nonideal MHD effects, caused by the non perfect coupling of B-fields and matter, are responsible for weakening the magnetic braking, allowing the formation of large discs (Mellon & Li 2008).

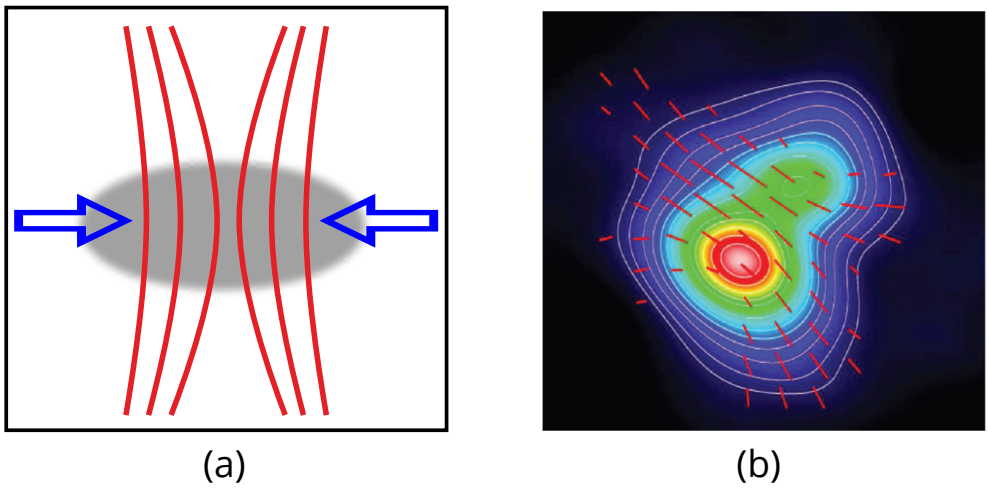

Figure 1.9: The characteristic hourglass shape of the field lines predicted by the theory of magnetically-driven collapse. In (a), a schematic model is shown: the collapse initially proceeds only along the field, flattening the core (in grey), but the increasing gravitational pull (blue arrows) eventually pinches the field lines inwards (in red). In (b) we show the first detection of this morphology in the protostar IRAS 4A. The colorscale and contours represent the dust emission, while the red segments the polarisation vectors rotated by 90° (see §1.5.1). Figure from Crutcher (2012), original data from Girart et al. (2006).

As just shown, magnetic fields represent a fundamental ingredient of the interstellar medium, and studying them is crucial for a complete understanding of star formation. However, observational studies of their properties are difficult to perform, since they are hardly directly detectable. Astronomers relies on magnetic effects on other components of the ISM —gas and dust— to investigate them. In the following, we illustrate some of these techniques.

1.5.1 Observing magnetic fields in the ISM

All the available methods to infer interstellar magnetic fields rely on observations of polarised radiation, either in continuum or in lines. A common formalism used to analyse polarised light is implemented in the Stokes parameters. Let us consider a light radiation with total intensity I. In the most common case, light is partially polarised, meaning that I consists of an elliptically polarised component $I \times P_{\rm E}$ and an unpolarised one $I \times (1 - P_{\rm E})$. $P_{\rm E}$ represents then the fraction

of total polarisation. The wave vector of the polarised light draws an ellipse on the celestial sphere. We now define the angle θ between the major axis of the ellipse and the north direction (also known as *position angle*, *PA*) and the angle α so that $\tan^{-1}(\alpha)$ equals the ratio of the minor to major axis (see Figure 1.10 for a visual representation). We can now introduce the Stokes parameters as follows:

$$I \,, \tag{1.38}$$

$$Q = I \times P_{\rm E} \cos(2\alpha) \cos(2\theta) \,, \tag{1.39}$$

$$U = I \times P_{\rm E} \cos(2\alpha) \sin(2\theta) \,, \tag{1.40}$$

$$V = I \times P_{\rm E} \sin(2\alpha) \,. \tag{1.41}$$

$$\tag{1.42}$$

The quantity $I_{\rm P} = I \times P_{\rm E} \cos(2\alpha)$ represents the linearly polarised intensity, which corresponds to a linear polarisation fraction $P = I_{\rm P}/I$. Similarly, the circularly polarised intensity is $I_{\rm C} = I \times P_{\rm E} \sin(2\alpha)$. The essential quantities in the study of linear polarisation, which will be used later in this work, are:

$$I_{\rm P} = \sqrt{Q^2 + U^2} \,, \tag{1.43}$$

$$\theta \equiv PA = \frac{1}{2} \tan^{-1}\left(\frac{U}{Q}\right) \,. \tag{1.44}$$

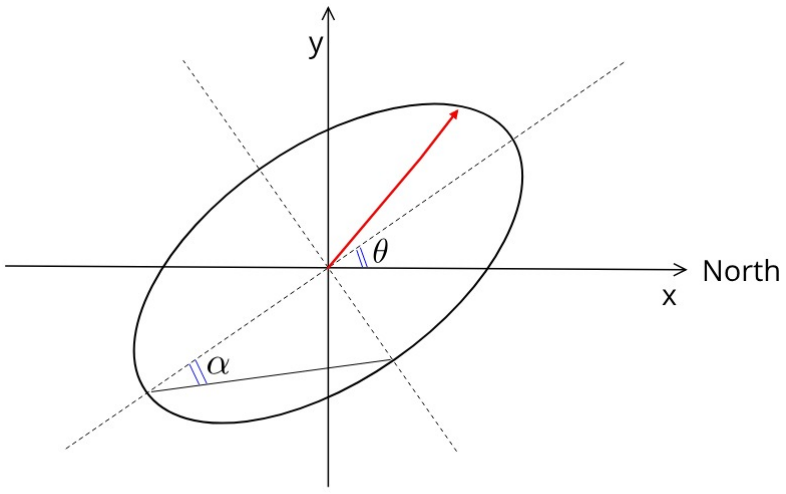

Figure 1.10: Geometry of a polarised light beam. The polarisation vector (in red) describes an ellipse on the celestial sphere. The angle θ is the inclination of the ellipse with respect to the North direction, while α is the arctangent of the ratio between minor an major axis of the ellipse.

Line polarisation

The only direct way of observing magnetic fields in molecular clouds relies on the Zeeman effect, i.e. the magnetic splitting of molecular energy levels. The degree of splitting is determined by the factor Z, which in turn depends on the specific spectral transition. In the normal Zeeman effect, the spectral line is split into three components, a linearly polarised one (π) at the original rest frequency, and two σ components, generally elliptically polarised, shifted in frequency of a factor $\Delta\nu_Z = \pm Z|\vec{B}|$. The strength of the π component is proportional to the field strength in the plane of sky parallel to $\vec{B}$. The elliptically polarised components, instead, arise from a combination of linear polarisation perpendicularly to $\vec{B}$ in the plane of sky and circular polarisation proportional to the field strength on the line of sight. As a result, from the study of all the components one can recover full information about $\vec{B}$ (Crutcher et al. 1993).

Observational studies are however difficult to perform. Only molecules with unpaired electrons have Z factors strong enough to allow for a detection. Furthermore, the $\Delta\nu_Z$ shift is usually smaller than the available spectral resolution of radio telescopes. In practice, from the fit of the Stokes I and V parameters one can derive the field strength along the line-of-sight only. The Stokes U and Q, which could bring some information about the plane-of-sky component, are usually too weak to be detected[12].

The first Zeeman splitting was observed in 1968 in the HI absorption line (Verschuur 1968). Since then, many observational campaigns were performed targeting HI, OH and CN lines in the interstellar medium (see e.g. Troland & Crutcher 2008; Falgarone et al. 2008). Attempts to observe the Zeeman effect in other molecular tracers failed. It is thus clear that, despite being the only direct way to assess the field strength, Zeeman measurements have strong limitations, mainly due to the weakness of the signals. This not only makes the detections difficult, but also limits this kind of investigations to small maps or single-pointing observations, which carry little information about the morphology of the field. We will now show that dust polarisation observations, although relying on strong assumptions for the data analysis, represent a good diagnostic tool of the B-fields properties.

Dust polarisation

The interpretation of dust polarisation observations, either in absorption on in emission, is based on the generally accepted idea that irregular dust grains are aligned with their minor axis parallel to the direction of the local magnetic field. The exact theoretical explanation of the alignment process is still however under debate (see for instance the review from Andersson et al. 2015). The most accredited theory is the so-called Radiative Torque Alignment (RAT, Lazarian 2007; Lazarian et al. 2015), which is based on the Barnett effect (Dolginov & Mitrofanov 1976). The underlying mechanism is that irregular grains exhibit different cross sections when scattering the right- and left-hand polarised light. As a result, grains experience a net torque and start spinning. The Barnett effect predicts that a spinning, charged particle develops a magnetic momentum.

[12] This is in general true for molecular lines in the ISM, with the exception of strong maser signals, where also the π components are sometimes observed (see for instance Green et al. 2015).

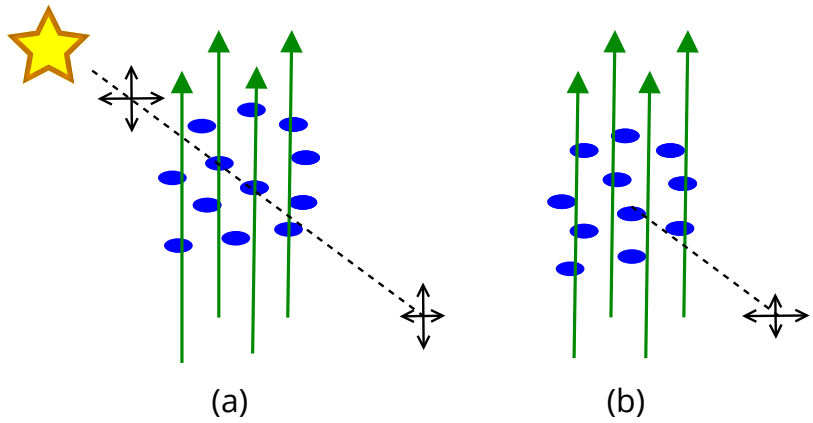

Figure 1.11: Schematic representation of dust polarisation in absorption (a) and emission (b). In blue, dust grains are aligned with their minor axes parallel to the direction of the *B*-field (green arrows).

The interaction of this momentum with the magnetic field causes the grain to precess and align with it, a process known as Barnett relaxation, resulting in the alignment of the dust particle.

If the exact theory of dust alignment is still under discussion, the observable effects of a population of aligned grains are clear, as summarised in Figure 1.11. When interacting with the unpolarised background starlight, grains will absorb the radiation preferentially along their longer axes, resulting in a net polarisation parallel to the direction of the magnetic field. The resulting linear polarisation, produced by the dichroic absorption by foreground grains, can be observed typically at optical and infrared wavelengths, i.e. in the part of the electromagnetic spectrum where star emission is at its peak. This technique has been widely used to trace the magnetic fields at molecular clouds' scale, as done for example by Goodman et al. (1990), Alves et al. (2008), and Franco & Alves (2015). However, it is limited to low visual extinction regions (typically $A_V \lesssim 10$ mag), since at higher column densities the light of background stars is completely absorbed by dust extinction.

A second effect of the grain alignment is the polarisation of the dust thermal emission, since grains emit preferentially in the direction of their major axis. The net linear polarisation is therefore oriented perpendicularly to the direction of the magnetic field, and can be detected with far-infrared and sub-millimetre observations. These have the great advantages of not being limited by visual extinction, allowing to recover information on magnetic fields even in dense cores, despite it is generally observed that dust polarised emission decreases with column density (see Chapter 4 for more details).

There are a few caveats that we would like to highlight regarding using dust polarisation to infer the interstellar magnetic field properties. First of all, they are sensitive only to the magnetic field component on the plane-of-sky, and therefore cannot be use to reconstruct the three-dimensional distribution of the magnetic field. Moreover, the analysis techniques that will be used in Chapter 4 rely entirely on the assumption that magnetic fields are the only responsible

for gran alignment. Recent works however demonstrated that there are other mechanisms able to align dust particles, such as radiative grain alignment (Tazaki et al. 2017) or self-scattering (Kataoka et al. 2015). In these cases, the detected polarisation is not linked anymore to the magnetic fields. However, these effects are relevant only at the very small scales of protoplanetary discs, and will therefore be neglected in this work.

1.6 Elements of radioastronomy

As previously stated, most of the electromagnetic radiation arising from molecular lines or from dust emission in molecular clouds falls in the far-infrared and radio regime. Radio telescopes are therefore the main type of instrumentation used to performed the described studies. Since in general the resolution of a telescope of diameter D at the wavelength λ is $\theta_{\rm res} \propto \lambda/D$, the long radio wavelengths require large facilities to achieve the same resolution of higher frequency observations. A possible alternative to increase the sensitivity and resolution is using interferometers. However, since in this work we did not perform any interferometric observation, we will focus only on single-dish observations.

Luckily for radio astronomers, the atmosphere is transparent in the range 1 cm – 10 m, as shown in Figure 1.12, allowing to build large antennas on Earth ($D \approx 10 - 100$ m). However, at sub-millimetre wavelengths, the atmospheric opacity increases mainly due to the water vapour absorption features. This is the main reason why telescopes working at 100 – 1000 GHz are built at high-altitude, dry places, such as the elevated deserts in Chile. At far-infrared wavelengths (hundreds of micrometres), moreover, the atmospheric transmission is zero, making it impossible to receive astronomical signals in this part of the electromagnetic spectrum from the ground. Satellites are therefore needed, which in turn greatly limit the antenna sizes. A possible compromising solution is represented by airborne facilities, such as the Stratospheric Observatory for

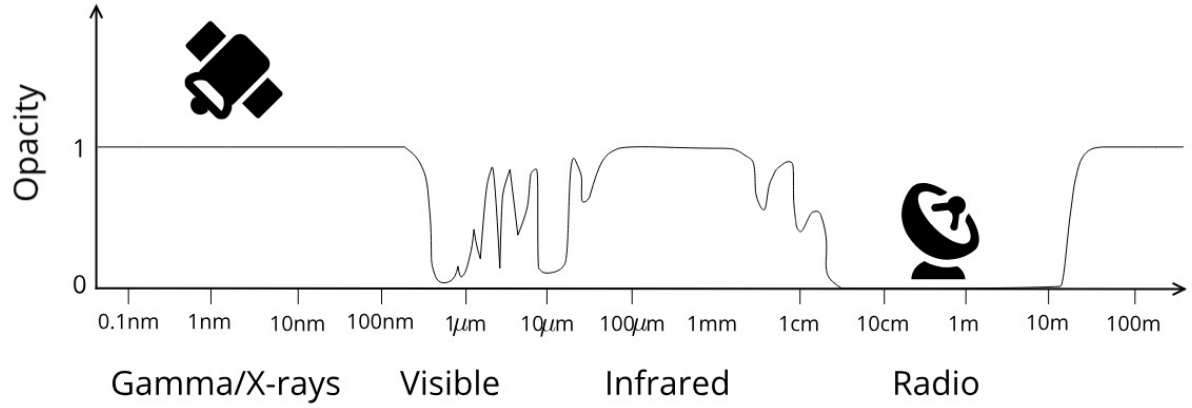

Figure 1.12: The atmospheric opacity as a function of wavelength. The different spectral bands are indicated.Between 5 cm and 10 m, the atmosphere is almost completely transparent.

Infrared Astronomy (SOFIA, shown in Figure 1.13) used to perform the observations presented in Chapter 4. It consists of an infrared telescope mounted on a modified 747SP Boing aircraft. Flying at 11000 – 15000 m, it avoids more than the 99% of atmospheric water vapour, allowing astronomers to access the whole infrared wavelength range (1 – 500 μm).

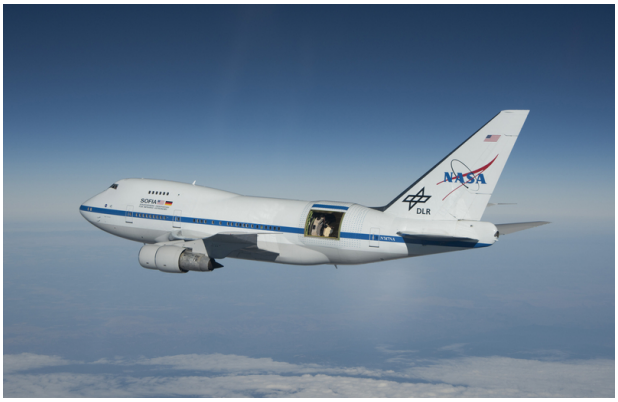

Figure 1.13: SOFIA airborne telescope during flight. Credit: NASA/Jim Ross.

A radio telescope consists of a main mirror which collects the incoming radiation and directs it towards the prime focus. Usually, a second mirror (subreflector) then conveys the wavefront to the secondary focus, where the receivers are placed. This configuration in fact allows to have easier access to the detectors. These are sensible to the electric field of the incoming radiation, and transform it into an electric signal. Most of the modern receivers convert the input frequency to a lower one (Intermediate Frequency, IF), a solution that grants great flexibility in the data analysis. The processing chain is usually divided in *frontends* and *backends*. The former are usually amplifiers and mixers and they operate the frequency downconversion. The signal at the IF frequency is then sent to the backends, such as spectrometers.

One of the main characteristics of a radio telescope is its beam pattern, which describes the antenna capabilities both in emission and in reception. As illustrated in Figure 1.14, a typical beam consists of a *main lobe*, which at the operative wavelengths should contain most of the power, and several *side lobes*. The main beam solid angle (and in particular its width, $\theta_{\rm MB}$) describes the telescope angular resolution. Another key parameter is the *beam efficiency*, which defines the fraction of power concentrated in the main lobe: the lower $\eta_{\rm MB}$ is, the more power is entering from side lobes, hindering the correct localisation of the emitting source. The forward efficiency $F_{\rm eff}$, on the other hand, describes the ratio between the radiation coming from the front of antenna and the total power, distributed over the entire 4π solid angle.

The backend outputs are "counts", arbitrary units which must be calibrated into flux scale. At cm-wavelengths the flux calibration is usually done with noise diodes that add to the incoming signal a known amount of noise. The calibration procedure consists in making an observation with the diode on and one with the diode off: the difference between the two contains only the noisy signal, which is known. The astronomical signals can therefore be calibrated. At mm-wavelengths, however, the atmosphere has larger influence and is rapidly changing. At these frequencies a common calibration procedure is the *chopper wheel method* (Kutner & Ulich 1981). In this case, three measurements are performed: one on-source, one towards the cold sky at a known elevation, and one with a room-temperature load (*ambient load*) in front of the receiver. Combining these observations with an atmospheric model, one can calibrate the on-source signal.

The noise level of the observation is given by the *system temperature* $T_{\rm sys}$, which takes into

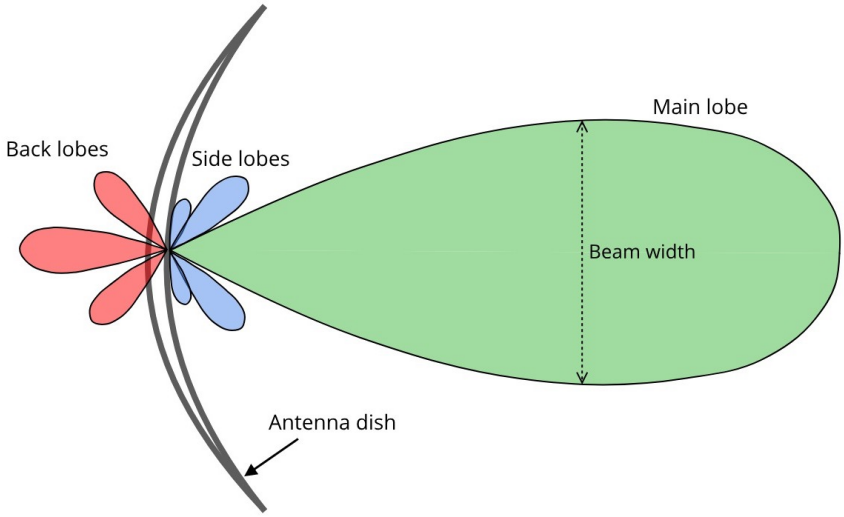

Figure 1.14: A schematic example of an antenna beam pattern, where the main lobe (in green), side lobes (in blue), and back lobes (in red) are visible.

account all the signal contributions in the data acquisition chain. The corresponding noise is:

$$\sigma = k\frac{T_{\rm sys}}{\sqrt{N_{\rm pol}t_{\rm int}\Delta\nu}} \tag{1.45}$$

where k is a constant depending on observing mode, $N_{\rm pol}$ is the number of polarizations to be averaged, $t_{\rm int}$ is the effective integrating time, and $\Delta\nu$ the frequency bandwidth. For spectral line observation, $\Delta\nu$ is the width of a single channel.

Continuum data are usually expressed in Jy/beam, or analogous units. However, spectroscopic data are often expressed in units of *antenna temperature* $T_{\rm A}$, which is the temperature that a resistor would have to emit the same power detected by the receiver. This is linked to the source brightness temperature $T_{\rm B}$ introduce in §1.2.2. The antenna temperature must be corrected for the atmospheric absorption, which is quantified by the line-of-sight opacity $\tau_\nu^{\rm atm}$:

$$T'_{\rm A} = T_{\rm A}e^{\tau_\nu^{\rm atm}} \ . \tag{1.46}$$

Since we are interested only in the radiation coming in the front main lobe, the *main beam temperature* scale is introduced:

$$T_{\rm MB} = \frac{F_{\rm eff}}{\eta_{\rm MB}}T'_{\rm A} \ . \tag{1.47}$$

If the source angular size is comparable to the beam resolution, it then holds that $T_{\rm MB} \approx T_{\rm B}$, and the main-beam temperature scale corresponds directly to the source brightness temperature.

There are two main kinds of observing modes: single-ponting and mapping. In the first, the telescope tracks the position of the source, and one single measurements is performed. The resulting signal comes from the whole beam size, but any spatial information is lost. This mode is used for instance for faint molecular emissions, since it can achieve low noise levels. The observations presented in Chapter 2 are an example of this technique.

In mapping, on the other hand, the telescope acquires data from multiple positions on the sky, allowing to reconstruct a two-dimensional image of the targeted source. One of the most recent techniques used for this is the on-the-fly (OTF) mapping, described for instance by Mangum et al. (2007). In this approach, the antenna slews in the chosen field recording data continuously. This choice minimises the telescope overheads, thus maximising its efficiency. In case of line observations, the resulting data consists of data-cubes, which have two spatial dimensions (positions of the plane-of-sky) and a spectral one (frequency). Chapter 3, for instance, is based on the analysis of OTF maps.

1.6.1 Commonly used frontends

In the radio regime, two widely used kinds of frontends are represented respectively by bolometer and heterodyne systems. *Bolometers*, in their simplest form, measure the incoming radiation through the heating effect of a resistance. The temperature increment is proportional to the radiation power. By using semiconductors or superconductors (which however require additional cooling systems), the sensitivity of these systems can be greatly enhanced. For instance, SOFIA implements modern transition-edge sensors, which consist of a superconductor kept close to its phase transition. This maximises the instrument sensitivity.

Bolometers are incoherent detectors, since they are not sensitive to the phase of the incoming wave front, and therefore they do not preserve any spectral informations. On the contrary, *heterodynes*, an example of which is shown in Figure 1.15, are coherent systems. They basically consist of mixers that mix the frequency of the incident radiation with a known one (*local*

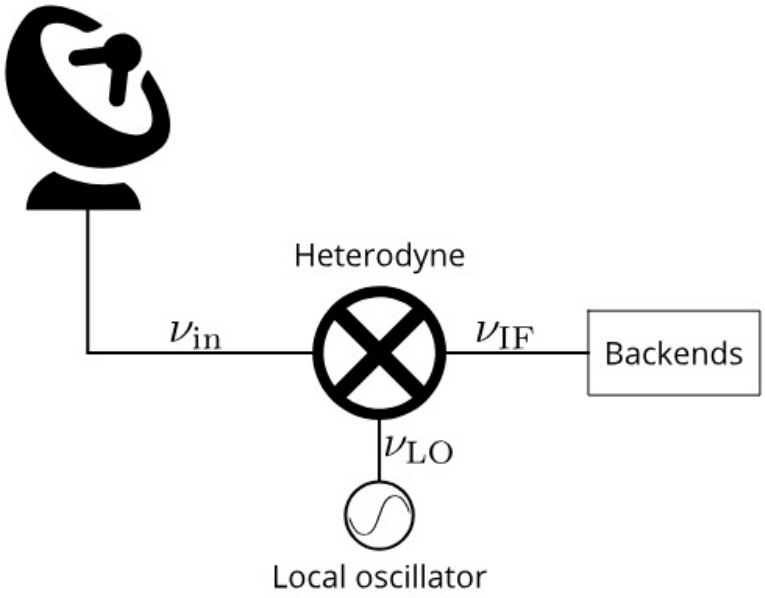

Figure 1.15: A schematic view of a heterodyne system, which mixes the frequency observed by the telescope ($\nu_{\rm in}$) with the one coming from the local oscillator ($\nu_{\rm LO}$), giving as an output the Intermediate Frequency $\nu_{\rm IF}$.

oscillator, or LO). Usually they are programmed to give as an output the difference of the two frequencies: $\nu_{\rm IF} = \nu_{\rm in} - \nu_{\rm LO}$. In this way, they operates a downconversion, since $\nu_{\rm IF} \ll \nu_{\rm in}$. As previously stated, this strategy brings great advantages for the following data analysis, since most of the available backends have better performance at $\nu \approx$ a few GHz.

1.7 This Thesis

After introducing the main theoretical basis involved in this thesis, in the present section we give the summary of the chapters that will follow:

- Chapter 2 discusses the nitrogen isotopic ratio in diazenylium in a small sample of prestellar cores. We use high-quality, single point spectra of N_2H^+, $N^{15}NH^+$, and $^{15}NNH^+$ to obtain the $^{14}N/^{15}N$ values using a non-LTE approach. Our results are inconsistent with the elemental value of $^{14}N/^{15}N = 440$, suggesting that the chemistry of N-bearing species is still poorly understood;

- Chapter 3 focuses on the deuteration maps of two abundant ions, diazenylium and protonated carbon monoxide, in the prototypical core L1544. Combining the non-LTE analysis with a state-of-art chemical network, we are able to assess the excitation state of each transition separately, in order to produce reliable column density maps. In this way, we can recover the deuteration levels not only in the core's centre, but also in its outskirts;

- Chapter 4 analyses the magnetic field properties of a protostellar core, IRAS 15398-3359, by means of its dust thermal emission. The chapter discusses the magnetic field morphology, quantifies its component on the plane-of-sky ($B_{\rm pos}$), and address the source dynamical state calculating the mass-to-flux ratio;

- Chapter 5 contains a brief summary of this work, followed by possible future perspectives of the presented projects.

Chapter 2

$^{14}N/^{15}N$ ratio measurements in prestellar cores with N_2H^+: new evidence of ^{15}N-antifractionation

The contents of this chapter were published in *Astronomy & Astrophysics* Journal.

2.1 Abstract

As illustrated in §1.3.2, in the last few decades the chemistry of nitrogen has raised interest in the context of understanding the formation of interstellar materials and of our own Solar System. Its isotopic ratio $^{14}N/^{15}N$ has been observed to show large variations among astrophysical sources, depending both on the type of target and on the molecular tracer used. However, these variations cannot be reproduced by the current chemical models. In particular, the high level of depletion showed by diazenylium in the prestellar core L1544 ($^{14}N/^{15}N$ = 1000, Bizzocchi et al. 2013) cannot be reproduced by the most recent theoretical results. So far, however, the observational evidence of anti-fractionation in low-mass star forming regions has been sparse due to the difficulty of such investigations, which require very long integration times ($\gtrsim$ 8 h). Diazenylium presents a further complication. Often, the N_2H^+ (1-0) emission is optically thick and presents hyperfine excitation anomalies that deviate from the local thermodynamic equilibrium (LTE) conditions (Daniel et al. 2006, 2013). Therefore, a fully non-LTE radiative transfer approach must be adopted, requiring knowledge of the physical structure of the observed source. This method has thus far been applied to only a few sources at early stages, besides L1544. One is the core Barnard 1b, in which isotopic ratios of $N_2H^+/N^{15}NH^+ = 400^{+100}_{-65}$ and $N_2H^+/^{15}NNH^+ > 600$ were measured by Daniel et al. (2013). A second study was performed in the L16923E core in L1689N, and resulted in $^{14}N/^{15}N = 300^{+170}_{-100}$ (Daniel et al. 2016). These two sources, however, are not truly representative of the prestellar phases. Barnard 1b hosts two extremely young sources with bipolar outflows (Gerin et al. 2015). 16293E in turn is located very close to the Class 0 protostar IRAS 16293-2422, and is slightly warmer than typical prestellar cores (T_{dust} = 16 K,

Stark et al. 2004). We can therefore say that the L1544 $^{14}N/^{15}N$ ratio in N_2H^+ appears peculiarly high, raising the doubt that it could represent an isolated and pathological case.

In this work, we present the analysis of three more objects: L183, L429, and L694-2. These are all *bona fide* prestellar cores according to Crapsi et al. (2005), due to their centrally peaked column density profiles and high level of deuteration. As in the case of L1544, we modelled their physical conditions and used a non-LTE code for the radiative transfer of N_2H^+, $N^{15}NH^+$, and $^{15}NNH^+$ emissions.

2.2 Observations

The observations towards the three prestellar cores L183, L429, and L694-2 were carried out with the Institut de Radioastronomie Millimétrique (IRAM) 30m telescope, located at Pico Veleta (Spain), during three different sessions. The telescope pointing was checked frequently on planets (Uranus, Mars, Saturn) or a nearby bright source (W3OH), and was found to be accurate to within 4″. We used the EMIR receiver in the E090 configuration mode. The tuning frequency for the three observed transitions are listed in Table 2.1. The hyperfine rest frequencies of $^{15}NNH^+$ and $N^{15}NH^+$ were taken from Dore et al. (2009). The single pointing observations were performed using the frequency-switching mode. We used the VESPA backend with a spectral resolution of 20 kHz, corresponding to 0.06 km s^{-1} at 90 GHz. We observed the vertical and horizontal polarisations simultaneously, and averaged them to obtain the final spectra.

Table 2.1: Rest frequencies of the observed transitions and 1σ uncertainties.

Species	Line	Frequency (MHz)
N_2H^+	$J = 1 \rightarrow 0$	93173.3991 ± 0.0004[a]
$N^{15}NH^+$	$J = 1 \rightarrow 0$	91205.6953 ± 0.0006[b]
$^{15}NNH^+$	$J = 1 \rightarrow 0$	90263.8360 ± 0.0004[b]

[a] From our calculations based on spectroscopic constants of Cazzoli et al. (2012);
[b] From our calculations based on spectroscopic constants of Dore et al. (2009).

L694-2 was observed in good weather condition during July 2011, integrating for 1.15 h for the N_2H^+ (1-0) transition, for 8.9 h for $N^{15}NH^+$ (1-0), and for 9.0 h for $^{15}NNH^+$ (1-0). L183 was observed in July 2012 in good to excellent weather conditions. The total integration times were 11 min (N_2H^+) and 4.3 h ($N^{15}NH^+$). L429 was observed during two different sessions (July 2012 and July 2017) in average weather conditions. We integrated for a total of 23 min for N_2H^+ (1-0) and 5.7 h on $N^{15}NH^+$ (1-0). We also observed for 1.2 h at the $^{15}NNH^+$ (1-0) frequency, but we not detect any signal. For all the sources, we pointed at the millimetre dust peak (Crapsi et al. 2005). The core coordinates, together with their distances and locations, are summarised in Table 2.2.

Complementary Herschel SPIRE data, used to obtain the density maps of the sources (see §2.4.1), were taken from the *Herschel Science Archive*. The observation IDs are: 1342203075

(L183), 1342239787 (L429), and 1342230846 (L694-2). We selected the highest-processing-level data, already zero-point calibrated and imaged (SPG version: v14.1.0). Figure 2.1 shows the three cores as seen with the Herschel SPIRE instrument at 350 μm, as well as the positions of the single-pointing observations performed with IRAM.

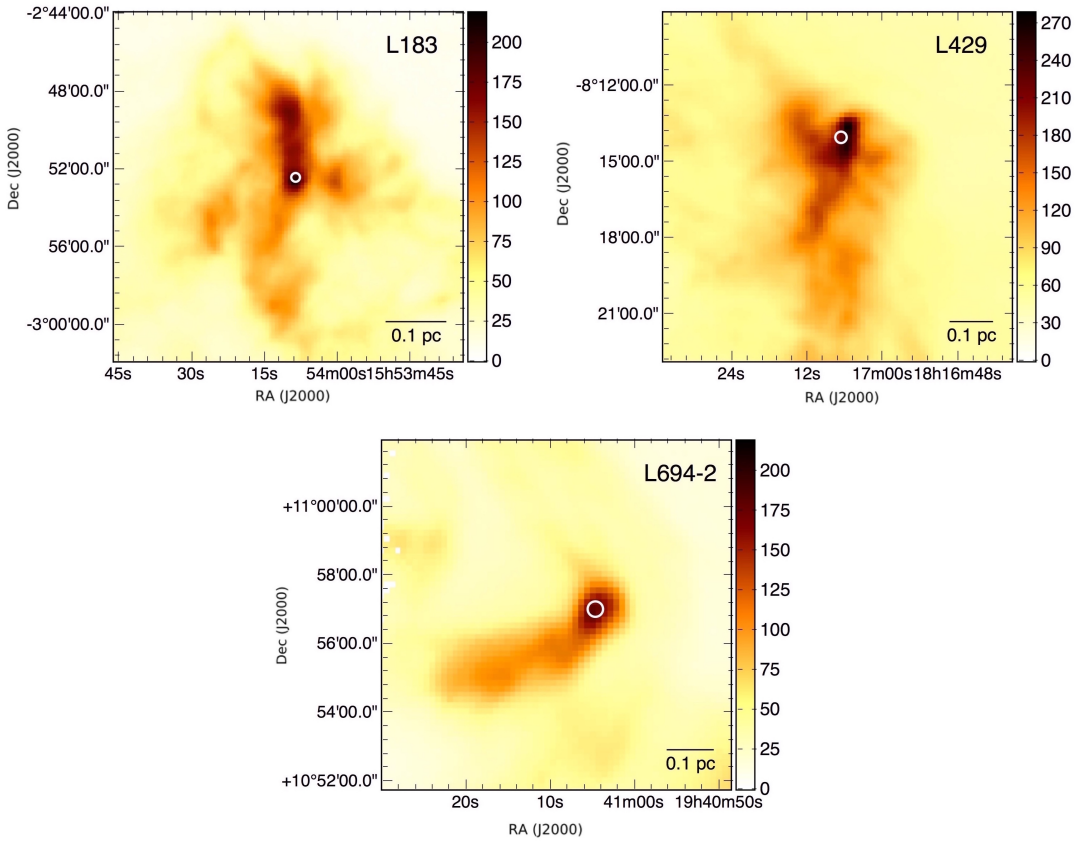

Figure 2.1: The three prestellar cores as seen in dust thermal emission at 350 μm with Herschel SPIRE camera, in units of MJy sr^{-1}. From top to bottom: L183, L429, L694-2. The scale bar is indicated in the bottom-right corner of each panel. The white circles represent the positions of the IRAM pointings and the size of the beam.

2.3 Results

The obtained spectra are shown in the left panels of Figure 2.2 (L183), Figure 2.3 (L429), and Figure 2.4 (L694-2). The data were processed using the GILDAS[1] software, and calibrated in main beam temperature $T_{\rm MB}$ using the telescope efficiencies ($F_{\rm eff}$ = 0.95 and $\eta_{\rm MB}$ = 0.80, respectively) at the observed frequencies. The typical rms is 10 – 20 mK for N_2H^+ (1-0), and

[1] Available at `http://www.iram.fr/IRAMFR/GILDAS/`.

Table 2.2: Sources' coordinates, distances, and locations.

Source	Coordinates[a]	Distance (pc)[b]	Location
L183	$15^h54^m8.32^s$, $-2^\circ52'23''.0$	110	High lat. cloud
L429	$18^h17^m6.40^s$, $-8^\circ14'0''.0$	200	Aquila Rift
L694-2	$19^h41^m4.50^s$, $10^\circ57'2''.0$	250	Isolated core

[a] Coordinates are expressed as RA, Dec (J2000);
[b] Distances taken from: Crapsi et al. (2005) (L429, L694-2), Pagani et al. (2004) (L183).

3 – 4 mK for the spectra of the rarer isotopologues, resulting in good- to high-quality detections. The minimum signal-to-noise ratio (S/N) is ≈ 8, whilst the maximum is ≈ 150.

The CLASS package of GILDAS was first used to spectrally fit the data. We used the HFS fitting routine, which models the hyperfine structure of the analysed transition assuming local thermodynamic equilibrium (LTE). Especially in the case of the N_2H^+ (1-0) line, this routine is not able to reproduce the observed data, due to the fact that the LTE conditions are not fulfilled. This is not due only to optical depth effects, which are taken into account in CLASS routines, but also to the fact that the excitation temperature is not the same for all the hyperfine transitions. A more refined approach that uses non-LTE analysis is therefore needed to compute reliable column densities, and will be discussed later (see §2.4). Nevertheless, the CLASS analysis provides reliable results for the local standard of rest velocity (V_{LSR}), whose values are summarised in Table 2.3. Different isotopologues give generally consistent results, within 3σ, for each source. The values derived from N_2H^+ (1-0) are also in agreement with the literature ones (Crapsi et al. 2005). Table 2.3 also summarises the total line width (full width at half maximum - FWHM) obtained with the CLASS fitting routine.

Table 2.3: Line parameters estimated from the CLASS HFS fitting routine.

Source	Line	V_{LSR} (km s^{-1})	FWHM (km s^{-1})
L183	N_2H^+ (1-0)	2.4145 ± 0.0004	0.222 ± 0.001
	$N^{15}NH^+$ (1-0)	2.390 ± 0.009	0.28 ± 0.03
L429	N_2H^+ (1-0)	6.7141 ± 0.0006	0.401 ± 0.001
	$N^{15}NH^+$ (1-0)	6.77 ± 0.02	0.41 ± 0.06
L694-2	N_2H^+ (1-0)	9.5577 ± 0.00014	0.2635 ± 0.0004
	$N^{15}NH^+$ (1-0)	9.562 ± 0.007	0.32 ± 0.03
	$^{15}NNH^+$ (1-0)	9.563 ± 0.011	0.30 ± 0.02

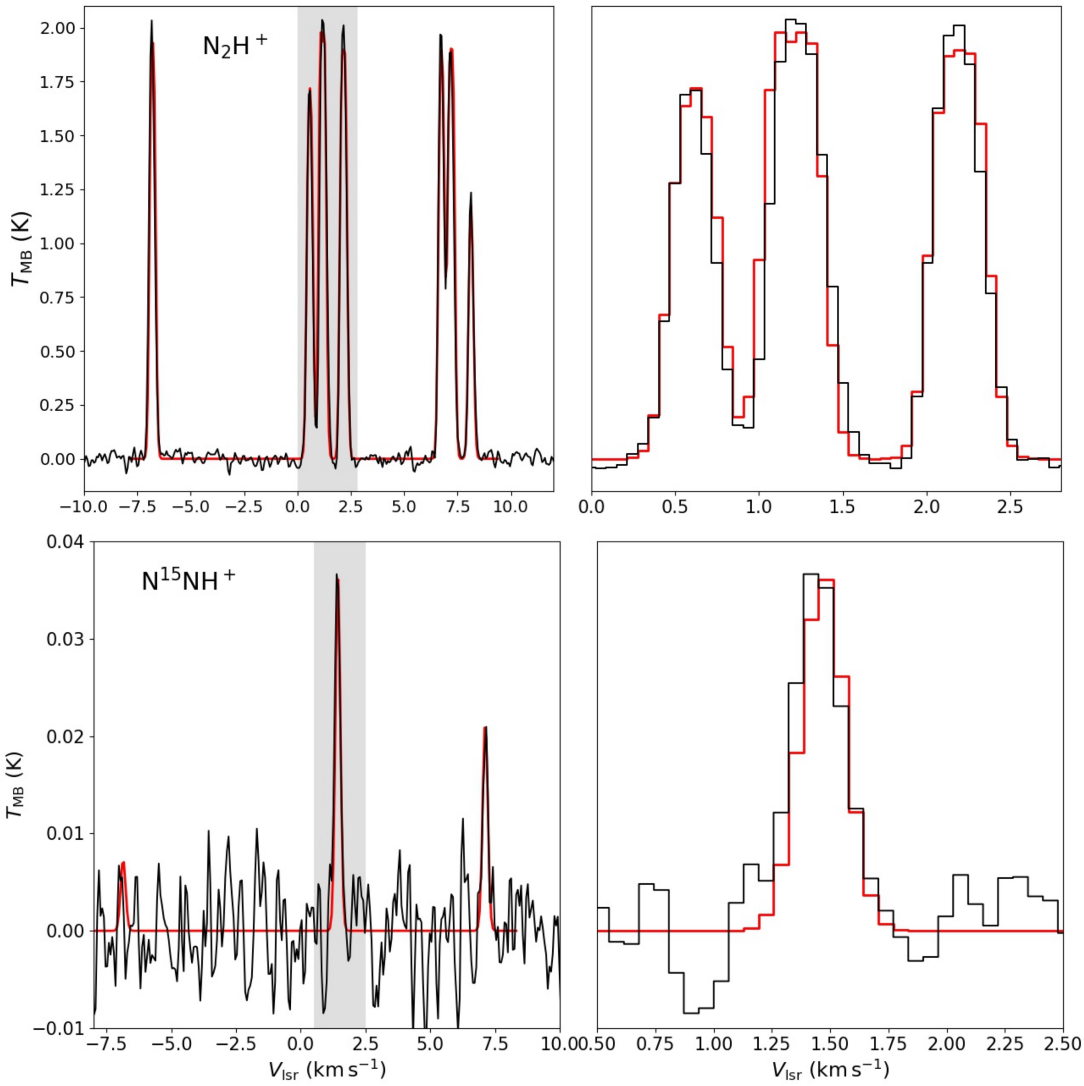

Figure 2.2: Observed (black) and modelled (red) spectra in L183, for N_2H^+ (top) and $N^{15}NH^+$ (bottom). The modelling was performed with MOLLIE as described in §2.4. The left panels show the entire acquired spectra, while the right ones are a zoom-in of the grey shaded velocity range.

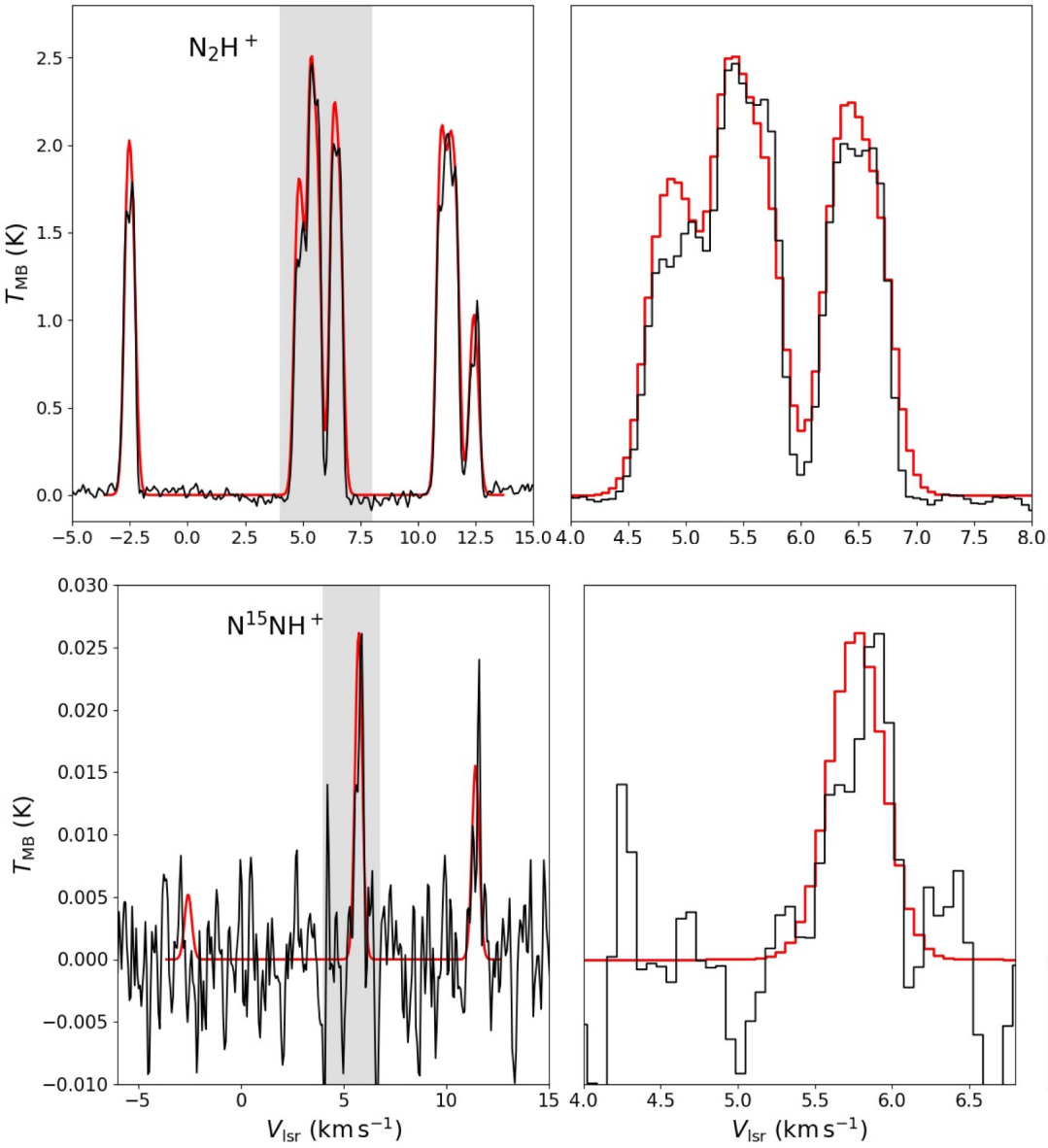

Figure 2.3: Observed spectra (black) and modelled ones (red) in L429, for N_2H^+ (top) and $N^{15}NH^+$ (bottom). The modelling was performed with MOLLIE as described in §2.4, and includes the infall velocity profile. The left panels show the entire acquired spectra, while the right ones are zoom-ins of the grey shaded velocity range.

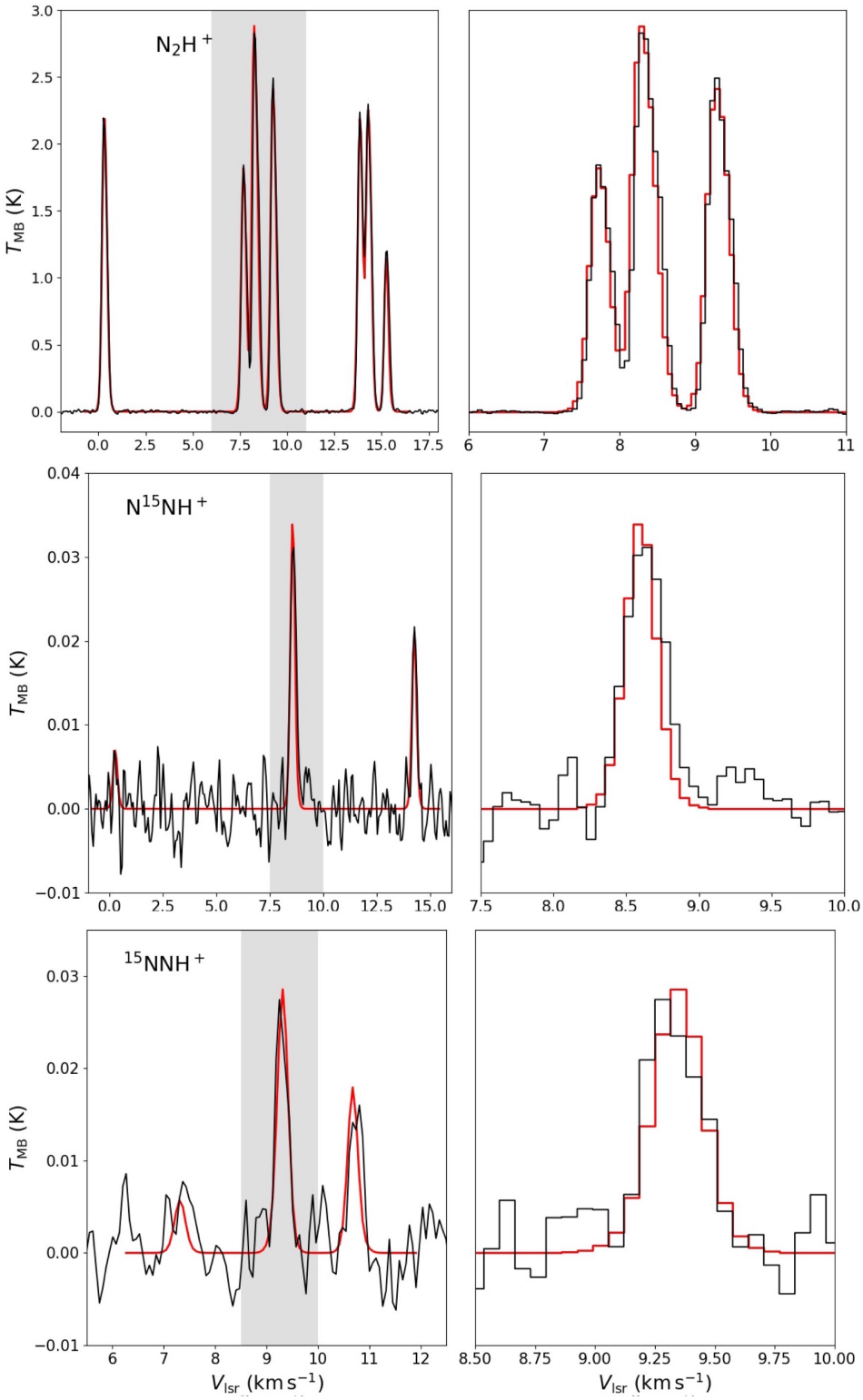

Figure 2.4: Observed (black) and modelled (red) spectra in L694-2, for N_2H^+ (top panel), $N^{15}NH^+$ (middle panel), and $^{15}NNH^+$ (bottom panel). The modelling was performed with MOLLIE as described in §2.4. The left panels show the entire acquired spectra, while the right ones are zoom-ins of the grey shaded velocity range.

2.4 Analysis

Our aim is to derive the column density of the different isotopologues, and to compute from their ratios the values of the corresponding $^{14}N/^{15}N$, assuming that they are tracing the same regions. For the reasons mentioned above, this is not possible using a standard LTE analysis (such as the one presented in Appendix A of Caselli et al. 2002c), as already shown for instance in the analysis of L1544 by Bizzocchi et al. (2013). Therefore, we used a non-LTE method based on the radiative transfer code MOLLIE (Keto 1990; Keto et al. 2004). MOLLIE can produce synthetic spectra of a molecule arising from a source with a given physical model. In particular, it is able to treat the case of overlapping transitions, and therefore can properly model the crowded N_2H^+ (1-0) pattern. In what follows, we first describe the construction of the core models, and then present the analysis of the observed spectra using MOLLIE. The case of L429, which presents peculiar issues, is treated separately.

2.4.1 Source physical models

MOLLIE is able to treat genuine three-dimensional (3D) source models. Nevertheless, for the sake of simplicity, we chose to model the cores in our sample as spherically symmetric (One-dimensional - 1D). As one can see in Figure 2.1, this assumption holds reasonably well for the densest parts of all cores[2]. For L183, a more sophisticated, two-dimensional (2D) model has already been developed in our team (Lattanzi et al., in prep.). This consists of a cylinder, with the axis lying on the plane of sky. In order to be consistent with the analysis of the other two cores, we decided to average this model in concentric annuli on the plane of sky to obtain a 1D profile.

The simplest 1D model consists of a volume density radial profile and a temperature radial profile. We therefore assume that the gas kinetic temperature and the dust temperature are equal. This is strictly true only when gas and dust are coupled ($n > 10^{4-5}$ cm^{-3}, Goldsmith 2001), but we do not have enough information on the spatial distribution of the gas temperature for all the sources, which would require maps of NH_3 (1,1) and (2,2) with JVLA (see Crapsi et al. 2007). On the other hand, the available continuum data allow us to determine reliable values for the dust temperature with a resolution of $\approx 40''$.

The volume density profile is derived from the analysis of the Herschel SPIRE maps at 250 μm, 350 μm, and 500 μm, as follows. Since we are interested in the core properties, we filtered out the contribution of the diffuse, surrounding material with a background subtraction. We computed the average flux of each map in the surrounding of the cores, at a distance of $\approx 500 - 800''$. This was assumed to be the background contribution, and was subtracted from the SPIRE images pixel by pixel. Then, the background-subtracted SPIRE maps were fitted simultaneously using a modified black body emission, in order to obtain the dust column density map of the source (for a complete description of the procedure, see for example Appendix B of Redaelli et al. 2017). We adopted the optically thin approximation, and a gas-to-dust ratio of 100

[2]L694-2 was modelled as an elongated cylinder with the axis almost along the line of sight by Harvey et al. (2003a,b), but for the sake of simplicity, and given the relative roundness of the source at high density (shown in Figure 2.1), we adopted a 1D model.

(Hildebrand 1983) to derive the H_2 column density. The dust opacity is assumed to scale with the frequency following Eq. 1.37:

$$\kappa_\nu = \kappa_{250\mu\mathrm{m}} \left(\frac{\nu}{\nu_{250\mu\mathrm{m}}} \right)^{\beta} , \tag{2.1}$$

where $\kappa_{250\mu\mathrm{m}} = 0.1\,\mathrm{cm^2\,g^{-1}}$ is the reference value at $250\,\mu$m (Hildebrand 1983), and $\beta = 2.0$, a suitable value for low-mass star-forming regions (Chen et al. 2016; Chacón-Tanarro et al. 2017; Bracco et al. 2017). From this procedure, one also gets the line-of-sight averaged dust temperature map of each source. These data, however, were not used in the following analysis.

The obtained column density map was averaged in concentric annuli starting from the densest pixel, and then a Plummer profile was fitted to the obtained points according to:

$$N_{\mathrm{mol}}(r) = \frac{N_{\mathrm{mol}}(\mathrm{H_2})_{\mathrm{peak}}}{\left[1 + \left(\frac{r}{r_0}\right)^2\right]^{\frac{p-1}{2}}} . \tag{2.2}$$

The obtained best-fit values of the free parameters (the characteristic radius r_0, the power-law parameter p and the central column density $N_{\mathrm{mol}}(\mathrm{H_2})_{\mathrm{peak}}$) can be used to derive the volume density profile $n(r)$, according to Arzoumanian et al. (2011), following:

$$n(r) = \frac{n_0}{\left[1 + \left(\frac{r}{r_0}\right)^2\right]^{\frac{p}{2}}} . \tag{2.3}$$

Table 2.4 summarises the best fit values of the Plummer-profile fitting of each source. The values obtained for the p exponent are in the range $\approx 2 - 3.5$, relatively consistent with those found for other cores using similar power-law profile shapes (e.g. in Tafalla et al. 2004; Pagani et al. 2007). The profiles obtained with this method typically show $n_0 \lesssim$ a few $10^5\,\mathrm{cm^{-3}}$, and fall below $10^5\,\mathrm{cm^{-3}}$ within the central ≈ 3500 AU. They thus fail to reach the high volume densities typical of prestellar cores centres. In fact, the integrated $n(r)$ profiles along the line of sight result in column density values lower by a factor of 2-4 compared to the results of Crapsi et al. (2005), although the dust opacity value used in that work is consistent with ours within 15%. This is due to the poor angular resolution of the SPIRE maps, which were all convolved to the beam size of the $500\,\mu$m map ($\approx 38''$). The central regions of dense cores are in fact better traced with millimetre dust emission observations performed with large telescopes, which allow to better see their cold and concentrated structure. In order to correct for this, we artificially increased the density in the central part ($5 - 10\%$ of the total core radius r_c), until the column density derived from this profile is consistent with the value obtained from 1.2 mm observations. The inserted density profile was taken from the central part of the profile developed through hydrodynamical simulations for L1544 in Keto et al. (2015), a model known to work well to reproduce the prestellar core properties.

The volume density profile derived in the previous paragraph is used as an input for the continuum radiative transfer code (CRT) (Juvela et al. 2001; Juvela 2005) to derive the dust temperature (T_{dust}) profile. The CRT is a Monte Carlo code that computes the emerging emission

Table 2.4: Summary of the best fit values for the parameters of the Plummer profiles, for each source.

Source	$n_0\,(\mathrm{cm}^{-3})$	p	$r_0('')$
L 183	$(4.1 \pm 0.7) \times 10^5$	1.95 ± 0.10	29 ± 2
L429	$(4.1 \pm 0.7) \times 10^5$	1.86 ± 0.08	16 ± 1
L694-2	$(1.8 \pm 0.5) \times 10^5$	3.32 ± 0.56	41 ± 6

and the dust temperature, given a background radiation field. For the latter, we used the standard interstellar radiation field of Black (1994). Since we want to model cores embedded in a parental cloud, the background radiation field has to be attenuated. Our team has the tabulated values for the Black (1994) model with an attenuation corresponding to a visual extinction of A_V = 1, 2, and 10 mag. We tested all three options, and found that generally the first two provide overly warm temperatures. We therefore decided to assume that radiation impinging on the cores is attenuated by an ambient cloud, whose thickness corresponds to a visual extinction of $A_V = 10$ mag. The external radiation field can still be multiplied by a factor k, in order to correctly reproduce the emitted surface brightness. To determine this parameter, we tested a number of values in the range $k = 0.5 - 5.0$, and for each one we computed the synthetic flux emitted at the SPIRE wavelengths at the cores' centres. We adopted the model that provides the best agreement with the observations[3]. Typically, we needed to increase the external radiation field by a factor of 2-3, suggesting that the assumed thickness of the ambient cloud was too large, and that the real, correct attenuation is somewhere in between 2 and 10 mag. This assumption is reasonable, as the H_2 column density derived from the SPIRE maps around the cores is usually $\approx 5\,10^{21}\,\mathrm{cm}^{-2}$, although we do not know the 3D structure of the cloud. The dust opacities are taken from Ossenkopf & Henning (1994) for unprocessed dust grains covered by thin icy mantles. This choice is made so that the dust opacity values used in this part are consistent with the one from Hildebrand (1983), used for fitting the SPIRE maps. Figure 2.5 shows the volume density and temperature profiles derived for each source.

The models built so far are static, that is, the velocity field is zero everywhere. However, we know that many cores show hints of infall or expansion motions (Lee et al. 2001). The velocity field can heavily impact the spectral features, and, when possible, it must be taken into account. For L183, in §2.4.2 we will show that the static model is good enough to properly reproduce the observations. For L694-2, we used the infall profile derived in Lee et al. (2007) using high-spatial-resolution HCN data. L429 represents a more difficult case, and will be accurately treated in the following subsections.

2.4.2 Spectral modeling with MOLLIE

The physical models developed in §2.4.1 are used as inputs for MOLLIE. The structure of each core is modelled with three nested grids of increasing resolution towards the centre, each com-

[3]When the observations were available, we also simulated the flux at millimetre wavelengths.

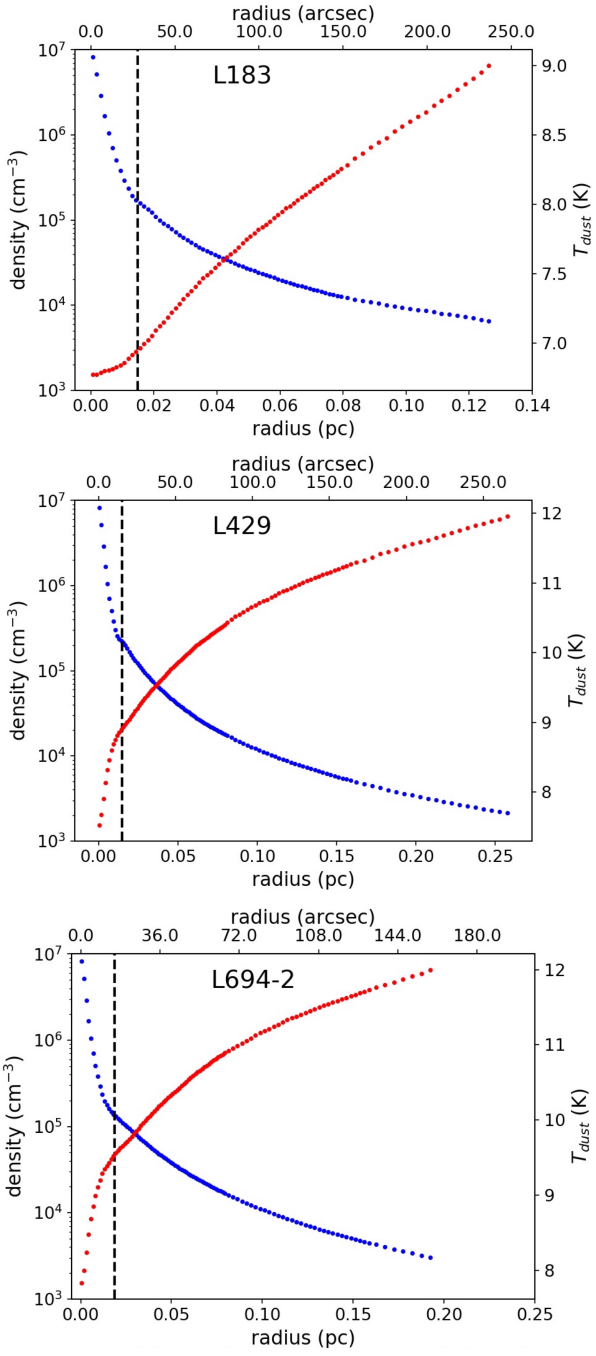

Figure 2.5: The volume density profile (blue dots) and the dust temperature profile (red dots) for the three cores (from top to bottom: L183, L429, L694-2), as a function radius in both pc and arcsec. The vertical, dashed lines represent the radius within which the density was artificially increased (see text for details).

posed of 48 cells, onto which the physical quantities' profiles are interpolated. The collisional coefficients used are from Lique et al. (2015), who computed them for the main isotopologue and the most abundant collisional partner, *p*-H_2. The *o*-H_2 is therefore neglected, which is a reasonable assumption given that the orto-to-para ratio (OPR) in dense cores is expected to be very low (in L1544, OPR $\approx 10^{-3}$, Kong et al. 2015). The collisional coefficients for $N^{15}NH^+$ and $^{15}NNH^+$ have been derived from those of N_2H^+ following the method described in Appendix A.1.

Our fit procedure has two free parameters, the turbulent velocity dispersion, $\sigma_{\rm turb}$, and the molecular abundance $X_{\rm st}$ with respect to H_2, assumed to be radially constant. Since MOLLIE requires very long computational times to fully sample the parameter space and find the best-fit values, we proceeded with a limited parameter space sampling. We first set the σ_{turb} value, testing ≈ 5 values on the N_2H^+ (1-0) spectra. This value is kept fixed also for the $N^{15}NH^+$ and $^{15}NNH^+$ (1-0) lines. We then produced eight synthetic spectra for each transition, varying the initial abundance each time, and convolving them to the 27″ IRAM beam. The results were compared to the observations using a simple χ^2 analysis, that is, computing:

$$\chi^2 = \sum_i \left\{ \frac{\left(T^i_{\rm MB,obs} - T^i_{\rm MB,mod}\right)^2}{\sigma^2_{\rm obs}} \right\}, \qquad 2.4$$

where $T^i_{\rm MB,obs}$ and $T^i_{\rm MB,mod}$ are the main beam temperature in the i-th velocity channel for the observed spectrum and the modelled one, respectively, and $\sigma_{\rm obs}$ is the rms of the observations. The sum is computed excluding signal-free channels. In order to evaluate the uncertainties, we fitted a polynomial function to the χ^2 distribution and set the lower/upper limits on X_{st} according to χ^2 variations of $\approx 20\%$ for the N_2H^+ (1-0) spectra and $\approx 15\%$ for the other isotopologues. We chose these two different limits due to different opacity effects. In fact, the N_2H^+ (1-0) lines are optically thick, and therefore changes in the molecular abundance lead to smaller changes in the resulting spectra compared to the optically thin $^{15}NNH^+$ and $N^{15}NH^+$ lines. Since the χ^2 distribution is usually asymmetric, so are the error bars. In order to evaluate the column densities, we integrated the product $n(H_2) \cdot X_{st}$ (convolved to the IRAM beam) along the line of sight crossing the centre of the model sphere. In Appendix A.2, we report the curves for the χ^2 in the analysed sources.

Figure 2.2 and 2.4 show the best fit spectra (in red), obtained as described above, in comparison with the observed ones (black curve) for L183 and L694-2 , respectively. The overall agreement is good, and most of the spectral features are well reproduced, as seen in the right panels, which show a zoom-in of the main component.

2.4.3 Analysis of L429

L429 represents a more difficult case to model. As one can see in Figure 2.3 and from the last column of Table 2.3, the N_2H^+ (1-0) line is almost a factor of two broader than in the other two sources. This may be due to the fact that this core is located in a more active environment, the Aquila Rift, but could also be a hint of multiple components along the line of sight. Moreover, concerning its velocity field, Lee et al. (2001) listed L429 among the "strong infall candidates" while in Sohn et al. (2007) the analysed HCN spectra show both infall and expansion features. A full characterisation of the dynamical state of the source and its velocity profile would require high-quality, high-spatial-resolution maps of molecular emission, which are beyond the scope of this paper. At the first stage, we tried to fit the observed spectra first increasing $\sigma_{\rm turb}$. The static model is however unable to reproduce the hyperfine intensity ratios, and therefore we adopted the infall profile of L694-2. The agreement with the observations increased significantly, meaning

that a velocity field is indeed required to model the spectra. Due to the difficulties in analysing this source, the χ^2 analysis previously described is not suitable, because it presents an irregular shape and its minimum corresponds to a clearly incorrect solution, due to the fact that it is not possible to simultaneously reproduce the intensity of all the hyperfine components. We therefore determined $X_{\rm st}$ in the same way as for $\sigma_{\rm turb}$, testing multiple values. We then associated the uncertainty to this value using the largest relative uncertainties found in the other two sources (24% for N_2H^+ (1-0) and 25% for $N^{15}NH^+$ (1-0)).

2.4.4 Obtained results

Table 2.5 summarises the values of $\sigma_{\rm turb}$, $X_{\rm st}$, and column density $N_{\rm mol}$ for each line in the observed sample. For a consistency check, since the rare isotopologue transitions are optically thin and do not present intensity anomalies, we derived their molecular densities using the LTE approach of Caselli et al. (2002c), focusing on the main component only. The results of this analysis are shown in the sixth column of Table 2.5 ($N_{\rm mol}^{\rm LTE}$). One can note that these values are consistent with the ones derived through the non-LTE method. The L183 physical structure and N_2H^+ emission have previously been modelled by Pagani et al. (2007). It is interesting to notice that their best fit profiles for both density and temperature are close to ours, even though their model is warmer in the outskirts of the source. Furthermore, despite a different abundance profile, their derived N_2H^+ column density is consistent with our value.

With the values for the molecular column densities found with the fully non-LTE analysis, we can infer the isotopic ratio dividing the main isotolopogue column densities from those of the corresponding rare isotopologue. Uncertainties are propagated using standard error calculation. The results are summarised in the last column of Table 2.5.

2.5 Discussion

Figure 2.6 shows a summary of the obtained isotopic ratios. Since from the analysis of Bizzocchi et al. (2013) the collisional rates for the N_2H^+ system have changed, we re-modelled the literature data for this source. The new results are: $^{14}N/^{15}N = 920^{+300}_{-200}$ (using $N^{15}NH^+$) and $^{14}N/^{15}N = 1000^{+260}_{-220}$ (using $^{15}NNH^+$). They are also shown in Figure 2.6. These values are perfectly consistent with the already mentioned literature value of $^{14}N/^{15}N = 1000 \pm 200$ of Bizzocchi et al. (2013). More recently, De Simone et al. (2018) computed again the nitrogen isotopic ratio from diazenylium in L1544, and found $^{14}N/^{15}N = 228 - 408$, a result inconsistent with ours. The IRAM data analysed by those authors, though, have a spectral resolution of 50 KHz (more than twice as coarse as ours). Furthermore, the authors used a standard LTE analysis, which is not suitable for this case, as already mentioned. This point has been studied in detail in Daniel et al. (2006, 2013), where the authors showed that in typical core conditions ($T \approx 10$ K, $n \approx 10^{4-6}$ cm^{-3}) the hypothesis of identical excitation temperature for all hyperfine components in the N_2H^+ (1-0) transition is not valid. Due to radiative trapping effects, in fact, the hyperfine intensity ratios deviate from the ones predicted with LTE calculations.

Table 2.5: Parameters and results of the modelling with MOLLIE.

Source	Line	σ_{turb}/km s^{-1}	$X_{st}/10^{-13}$	$N_{mol}/10^{10}$cm^{-2}	$N_{mol}^{LTE}/10^{10}$cm^{-2}	$^{14}N/^{15}N$
L183	N_2H^+	0.12	$2.50^{+0.25}_{-0.60}\,10^3$	$1.29^{+0.13}_{-0.31}\,10^3$	-	
	$N^{15}NH^+$	0.12	$3.75^{+0.95}_{-0.75}$	$1.93^{+0.49}_{-0.38}$	$2.24^{+0.54}_{-0.54}$	670^{+150}_{-230}
L429	N_2H^+	0.23	$4.5\,10^3$	$1.82^{+0.44}_{-0.44}\,10^3$	-	
	$N^{15}NH^+$	0.23	5.5	$2.5^{+0.63}_{-0.63}$	$2.46^{+0.44}_{-0.44}$	730^{+250}_{-250}
L694-2	N_2H^+	0.12	$3.50^{+0.60}_{-0.35}\,10^3$	$1.26^{+0.22}_{-0.12}\,10^3$	-	
	$N^{15}NH^+$	0.12	$6.00^{+1.00}_{-1.00}$	$2.17^{+0.36}_{-0.36}$	$2.74^{+0.43}_{-0.43}$	580^{+140}_{-110}
	$^{15}NNH^+$	0.12	$5.00^{+0.90}_{-1.20}$	$1.81^{+0.32}_{-0.44}$	$2.13^{+0.37}_{-0.37}$	700^{+210}_{-140}
L1544[a]	N_2H^+	0.075	$5.50^{+1.25}_{-0.75}\,10^3$	$1.73^{+0.39}_{-0.24}\,10^3$	-	
	$N^{15}NH^+$	0.075	$6.00^{+1.00}_{-1.40}$	$1.89^{+0.31}_{-0.44}$	$2.45^{+0.57}_{-0.57}$	920^{+300}_{-200}
	$^{15}NNH^+$	0.075	$5.50^{+0.95}_{-0.70}$	$1.73^{+0.30}_{-0.22}$	$2.02^{+0.28}_{-0.28}$	1000^{+260}_{-220}

[a] The values for L1544 are based on the data shown in Bizzocchi et al. (2013). The non-LTE modeling uses the updated collisional rates, while the LTE results were derived adopting revised excitation temperature values.

Figure 2.6 shows that the computed values are consistent within the source sample. Due to the large uncertainties, we can conclude that the isotopic ratios are only marginally inconsistent with the value of 440, representative of the Protosolar Nebula (black, dashed curve). Nevertheless, the trend is clear. Despite the fact that L1544 still present the highest values in the sample, its case is now clearly not an isolated and pathological one. This larger statistics therefore supports the hypothesis that diazenylium is ^{15}N-depleted in cold prestellar cores. Instead of "super-fractionation" predicted by some chemistry models, N_2H^+ seems to experience "anti-fractionation" in these objects. As already stressed out, this trend cannot be understood within the frame of current chemical models. Roueff et al. (2015) predict that the $^{14}N/^{15}N$ should be close to the protosolar value ($\approx$ 400). Wirström & Charnley (2018) came to very similar conclusions. In both chemical networks, the physical model assumes a temperature of 10 K for the gas, which is up to 40% higher than the values found for the central parts of the cores (6 – 7 K). However, further calculations have shown that lowering the temperature by 2 – 3 K does not produce significant differences in the results (Roueff, private communications). Visser et al. (2018) highlighted how isotope-selective photodissociation is a key mechanism to understand the nitrogen isotopic chemistry in protoplanetary discs. We can speculate that different levels of selective photodissociation in different environments could reproduce the variety of N-isotopic ratios that are observed. Further investigation of this point from both an observational and a theoretical point of view is merited.

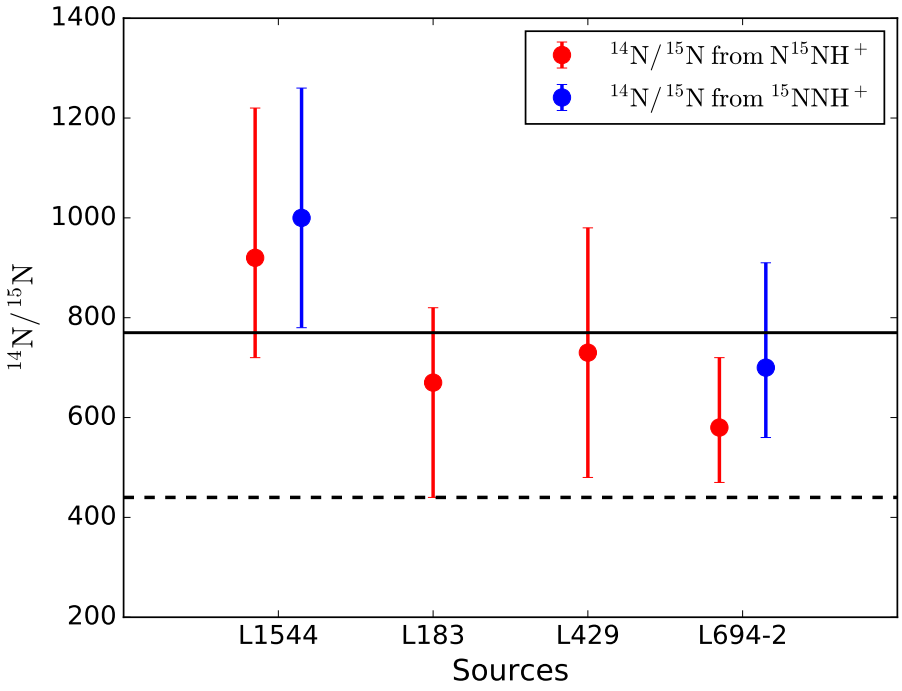

Figure 2.6: The $^{14}N/^{15}N$ values obtained in the sample presented in this paper and re-computed for L1544 with errorbars, determined with the method described in the main text. Red points refer to measurements of $N^{15}NH^+$, while blue ones of $^{15}NNH^+$. The solid line represents the average value found in the whole sample (= 770), while the dashed curve is the Protosolar Nebula value (440).

From the L1544 and L694-2 results, there seems to be tentative evidence that $N^{15}NH^+$ is more abundant than $^{15}NNH^+$. This can be explained by the theory according to which the proton transfer reaction,

$$^{15}NNH^+ + N^{15}N \rightleftharpoons N^{15}NH^+ + N^{15}N\ , \qquad 2.5$$

tends to shift the relative abundance of the two isotopologues, slightly favouring $N^{15}NH^+$ due to the fact that $N^{15}NH^+$ zero-point energy is lower than that of $^{15}NNH^+$ by 8.1 K (see reaction RF2 in Wirström & Charnley 2018). It is interesting that the same trend is found also in a very different environment such as OMC-2 FIR4, a young protocluster hosting several protostellar objects. In this source, Kahane et al. (2018) measured lower values for the isotopic ratio, but in agreement with our result found that $^{15}NNH^+$ is less abundant than $N^{15}NH^+$. However, we emphasise that higher-quality observations and those with better statistics are needed to confirm this point.

2.6 Conclusions

We have analysed the diazenylium isotopologues' spectra in three prestellar cores, L183, L429 and L694-2 in order to derive nitrogen isotopic ratios. Since LTE conditions are not fulfilled, especially for the N_2H^+ (1-0) transition, we have used a fully non-LTE radiative transfer approach, implemented in the numerical code MOLLIE. We have carefully derived the physical models of the sources, computing their volume density and dust temperature profiles. With these, we were able to produce synthetic spectra to be compared with our observations, in order to derive the best-fit values for the molecular abundances and column densities. Using the same method, we have also re-computed the isotopic ratio of L1544. The difference with the literature value of Bizzocchi et al. (2013), due to changes in the molecular collisional rates, is well within the uncertainties.

In our sample of four cores, we derived $^{14}N/^{15}N$ values in the range 580 – 1000. Within the confidence range given by our uncertainties estimation, all our results are inconsistent with the value ≈ 400, predicted by the current theoretical models. L1544 still presents higher depletion levels than the other sources, but in general all the cores are anti-fractionated. The theoretical bases of such a trend are at the moment not understood. A deep revision of our knowledge of the nitrogen chemistry is required in order to understand the chemical pathways that lead to such low abundances of $N^{15}NH^+$ and $^{15}NNH^+$ compared to the main isotopologue.

2.7 Future perspectives

As the work of this Chapter has shown, nitrogen chemistry is still far from being completely understood. In particular, at the moment only two possible explanations have been proposed by chemical models for the observed $^{14}N/^{15}N$ values of N_2H^+. The first one, proposed by Furuya & Aikawa (2018), involves selective photodissociation mechanisms. In the early prestellar stages, when the visual extinction is still moderate ($A_V \lesssim 3$ mag), the low optical depth of $N^{15}N$ makes it more prone to be photodissociated with respect to N_2. The resulting ^{15}N atoms quickly freeze-out onto the dust grains, when they are hydrogenated into ammonia ($^{15}NH_3$). The net result is that the gas phase is depleted of ^{15}N, leading to high $^{14}N/^{15}N$ measurements in N_2H^+, whilst ammonia ices are enriched in ^{15}N. Currently, the composition of dust ices is not observable. However, one would expect that when the temperature rises and the ices sublimate, or when shocks destroy the dust grains, $^{15}NH_3$ molecules are released back into the gas phase, where they can be detected. In order to test this hypothesis we have obtained observing time at the Green Bank Telescope to detect NH_3 and $^{15}NH_3$ lines towards three sources: a prestellar core, a protostar and a shocked region. If the theory of Furuya & Aikawa (2018) is correct, the data analysis should lead to lower $^{14}N/^{15}N$ measurements in the two more evolved sources with respect to the cold prestellar object.

A second theoretical model that predicts the anti-fractionation of N_2H^+ was developed by Loison et al. (2019). They used the 3-phase chemical model Nautilus (Ruaud et al. 2016) to follow the nitrogen chemistry during the star formation process. They suggest that the observed $^{14}N/^{15}N$ values in N_2H^+ can be due to a difference in the dissociative recombination (DR) rates for the different isotopologues. The main N_2H^+ destruction pathways, according to their model,

are in fact:

$$N_2H^+ + e \rightarrow N_2 + H \ ,$$
$$N_2H^+ + CO \rightarrow N_2 + HCO^+ \ .$$

When gas-phase CO abundance is low, such as in the cold and dense prestellar cores —where CO is mainly frozen onto dust grain surfaces— the dominant reaction is the DR one. If the DR rate of N_2H^+ is lower than those of $N^{15}NH^+$ and $^{15}NNH^+$, the $N_2H^+/N^{15}NH^+$ and $N_2H^+/^{15}NNH^+$ ratios can be significantly larger than the elemental value. When on the other hand CO abundance is high, its reaction with N_2H^+ becomes competitive and the molecular isotopic ratio decreases back to the elemental value. Recent laboratory work showed that N_2H^+ isotopologues exhibit DR rates that vary up to 20% in value, even though no data are available at the ISM low temperatures (Lawson et al. 2011). There are a few observational hints that point towards this direction: for

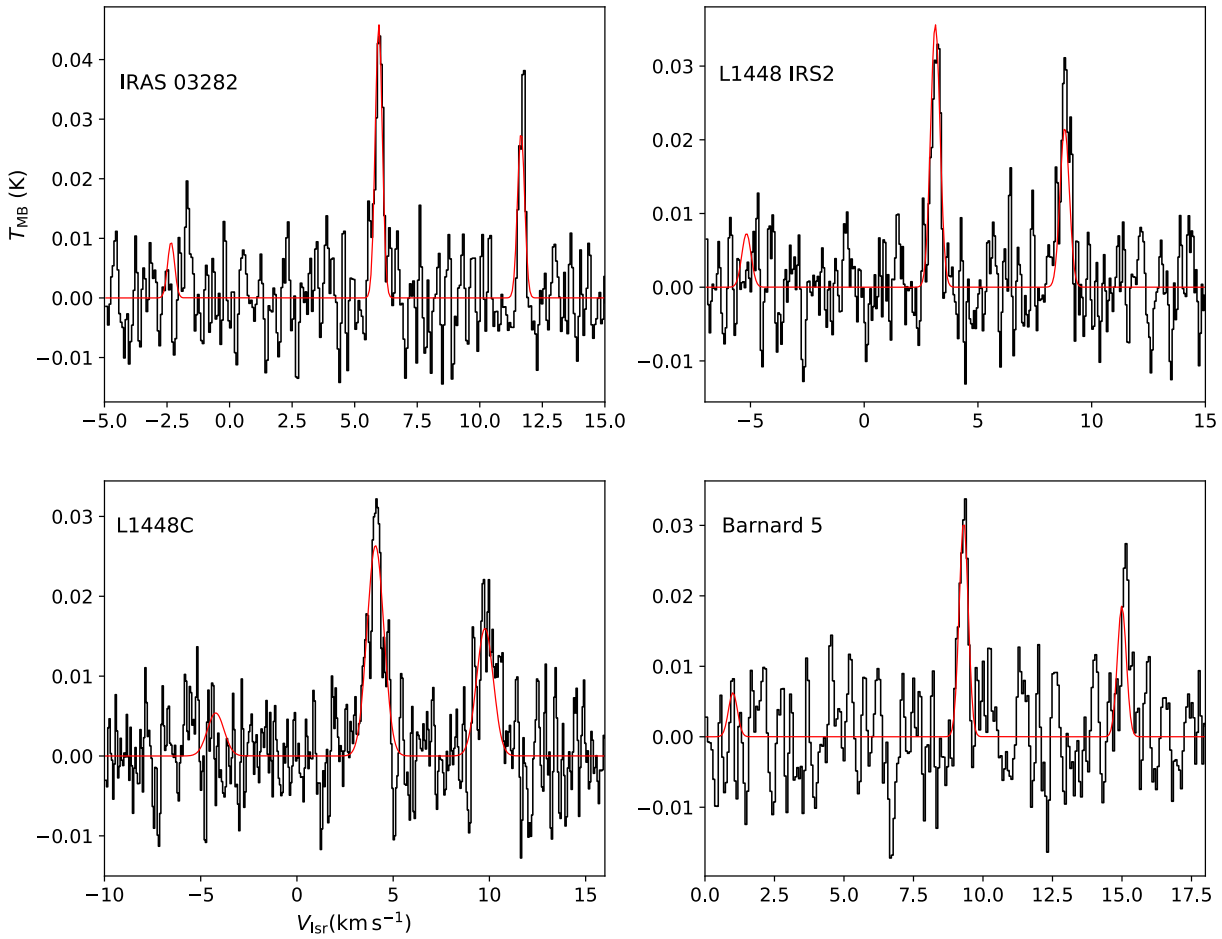

Figure 2.7: The $N^{15}NH^+$ (1-0) spectra detected towards four protostars in Perseus (in black) with overlaying the best-fit model obtained with CLASS (in red). The source name is labeled in the top-left corner of each panel.

instance, the $^{14}N/^{15}N$ values measured in OMC-2, a protocluster containing several protostars and thus relatively warm, are significantly lower than the ones measured in the prestellar core sample just presented (Kahane et al. 2018). In the high mass regime, Fontani et al. (2015) found an anti-correlation between $N_2H^+/N^{15}NH^+$ and N_2H^+/N_2D^+. Since the deuteration process is highly favoured by the CO depletion (Dalgarno & Lepp 1984), these results also suggest that $N_2H^+/N^{15}NH^+$ is larger where CO is mostly absent from the gas-phase.

In order to test this hypothesis, we have successfully asked to perform observations of the $^{14}N/^{15}N$ ratio in N_2H^+ in a sample of five low-mass protostars with the IRAM 30m telescope. Due to the warming by the protostellar activity, in the envelope of these objects CO starts to evaporate and returns back into the gas-phase. We thus expect the $^{14}N/^{15}N$ to decrease and become closer to the elemental value (≈ 400). To our knowledge, this will represent the first sample of isotopic ratio measurements of N_2H^+ in low-mass protostars. Observations are still ongoing. The rare isotopologue $N^{15}NH^+$ has been detected in all the four sources already targeted. The observed spectra are presented in Figure 2.7, together with the best fit of the hyperfine structure obtained with the HFS routine from CLASS. The missing observations, and in particular the N_2H^+ spectra, do not allow us to determine consistently the nitrogen isotopic ratios. However, we can use literature data to obtain preliminary results. Emprechtinger et al. (2009) published the column densities and excitation temperatures of N_2H^+ for a sample of protostars that include also our sources. These values are summarised in Table 2.6, where we report also the dust temperature measurements from that paper. We can have a preliminary estimation of the column density of the rarer isotopologue using the optically thin approximation (see Eq. 1.28), applied to the hyperfine main component only, similarly to how $N_{\rm mol}^{\rm LTE}$ was derived in §2.4.4. To calculate the integrated intensity (W) of this component, we model it with a Gaussian profile. The resulting $N_{\rm mol}(N^{15}NH^+)$ can be used to derive the isotopic ratios, which are also reported in Table 2.6.

The resulting isotopic ratios are found in the range 470 – 1000, the average being $^{14}N/^{15}N$ = 680. These values are consistent with those found in the prestellar core sample. Furthermore, no clear trend with the dust temperature is found. We want to highlight that to derive robust

Table 2.6: Column densities, dust temperature, excitation temperature, integrated intensity of the main line, and isotopic ratio values derived for the four protostar detected in $N^{15}NH^+$. See the Text for more details.

Source	$N_{\rm mol}(N_2H^+)$[a]	$T_{\rm dust}$[a]	$T_{\rm ex}$[a]	W	$N_{\rm mol}(N^{15}NH^+)$	$^{14}N/^{15}N$
	10^{13} cm^{-2}	K	K	10^{-2} K km s^{-1}	10^{10} cm^{-2}	
IRAS 03282	1.6 ± 0.2	23	8.6 ± 0.2	1.80 ± 0.19	2.9 ± 0.5	550 ± 120
L1448 IRS2	3.1 ± 0.5	27	6.8 ± 0.2	1.59 ± 0.17	3.1 ± 0.5	1000 ± 230
L1448C	2.4 ± 0.4	32	7.3 ± 0.2	2.81 ± 0.23	5.1 ± 0.8	470 ± 110
Barnard 5	1.6 ± 0.2	50	7.2 ± 0.2	1.21 ± 0.15	2.3 ± 0.4	700 ± 150

[a] Values taken form Emprechtinger et al. (2009).

conclusions it is necessary to observe also the main isotopologue lines and to derive the column densities of both N_2H^+ and $N^{15}NH^+$ in a consistent way. However, if confirmed by future analysis, our results seem to disprove the theoretical model of Loison et al. (2019).

Chapter 3

High-sensitivity maps of molecular ions in L1544: Deuteration of N_2H^+ and HCO^+ and primary evidence of N_2D^+ depletion.

The contents of this chapter were published in *Astronomy & Astrophysics* Journal.

3.1 Abstract

The deuterium fraction is a good diagnostic indicator of the initial phases of star formation, as it was shown in the Introduction. In particular, in prestellar cores deuterated molecules are abundant, due to a combination of physical conditions that makes this fractionation process very efficient (see §1.3.1 for more details). Furthermore, deuteration is linked to another key parameter: the ionisation fraction $x(e)$, which as illustrated in §1.5 plays an important role in the evolution of star forming regions. This quantity, in fact, determines the timescale for the ambipolar diffusion of neutrals across the magnetic field lines, which is the main process that allows the gravitational collapse of magnetised cores (Mouschovias & Spitzer 1976). In molecular clouds, the deuteration fraction is in general considered a good indicator of the ionisation degree (Guelin et al. 1977; Caselli et al. 1998, 2002c; Dalgarno 2006), as the hydrogen isotopic ratio in species such as HCO^+ is a function of $x(e)$. As a consequence, accurate measurements of the D/H ratio allow the ionisation degree in prestellar cores to be determined. In particular, N_2H^+ and HCO^+ represent ideal tracers (Caselli et al. 1998, 2002a); these molecules —and their deuterated counterparts— are abundant in low-mass cores. It has been shown that N_2H^+ is usually highly concentrated in the central parts, whereas HCO^+ traces the outer layers (e.g. Punanova et al. 2018). Combined, they can provide information on the ionisation degree in the whole source.

In this Chapter, we focus on one specific source: the prestellar core L1544, which is one of the most studied objects of its kind. Its vicinity ($d \approx 135$ pc, Schlafly et al. 2014) and bright continuum emission at mm and sub-mm wavelengths (Ward-Thompson et al. 1999; Doty et al. 2004; Spezzano et al. 2016) make it the ideal environment to study the early stages of low-

mass star formation. The central part of the core is cold ($T \approx 6$ K, Crapsi et al. 2007) and dense ($n > 10^6$ cm^{-3}, Tafalla et al. 2002; Keto & Caselli 2010). L1544 is centrally peaked and shows signatures of contraction (Caselli et al. 2002b; Lee et al. 2001; Caselli et al. 2012), suggesting that it is on the verge of gravitational collapse. In the last 20 years, a vast observational campaign combined with theoretical efforts has led to a deep knowledge of its physical and chemical structure (see e.g. Crapsi et al. 2007; Caselli et al. 2012; Keto et al. 2015; Spezzano et al. 2017). Previous works (Caselli et al. 1998, 2002c) have already investigated the deuteration level and ionisation fraction in this source, using the telescope capabilities available at that time. In this Chapter, we present new high-sensitivity maps of N_2H^+, N_2D^+, $HC^{18}O^+$, and DCO^+ across the whole core performed with the on-the-fly method. For the first time, we can analyse the first three rotational transitions of N_2D^+ and DCO^+ and the N_2H^+ (1-0) and (3-2) lines[1] simultaneously. In this paper we report the deuteration fraction maps of N_2H^+ and HCO^+ in L1544, obtained with a detailed non-LTE modelling of the molecular spectra at the centre of the core. The Chapter is structured as follows: in §3.2 we present the observations. The analysis is described in §3.3, divided into chemical modelling (§3.3.1), non-LTE modelling (§3.3.2), and column density derivation (§3.3.4). We discuss the results in §3.4, and draw a summary of the work in §3.5.

3.2 Observations

All the data presented in this Chapter were collected with the IRAM 30m single dish telescope. We used the four receivers of the frontend EMIR (E0, E1, E2 and E3), which allow us to cover the required frequency range. The N_2H^+ (1-0) data were acquired in summer 2015. Observations of N_2H^+ (3-2), N_2D^+ (1-0), (2-1), and (3-2), $HC^{18}O^+$ (1-0), and DCO^+ (1-0), (2-1), and (3-2) were performed during winter 2015/2016 using four different spectral setups. The VESPA backend, with a spectral resolution of 20 kHz, was used for all data except for the DCO^+ (1-0) transition, which was acquired with the FTS backend (resolution: 50 kHz). In all the sessions, the pointing was frequently checked on nearby planets or bright quasars, and found to be accurate within 2″ and 5″ (at the high and low frequencies, respectively). In order to encompass the whole core, all the transitions were acquired in the OTF map mode with a $2' \times 2'$ ($\approx 0.08 \times 0.08$ pc^2) footprint centred at the L1544 dust peak (R.A.(J2000)= $05^h04'17''.21$, Dec.(J2000)= $25^\circ10'42''.8$, Ward-Thompson et al. 1999). The N_2H^+ (1-0) data, observed in a different session, consist of a $4' \times 4'$ ($\approx 0.16 \times 0.16$ pc^2) map across the dust peak.

The spectra, originally calibrated to antenna temperature (T_A^*), were converted to main beam temperature (T_{MB}) using the tabulated values for the 30m forward efficiency (F_{eff}) and main beam efficiency (η_{MB}). The main features of the observed lines, such as their frequency, angular resolution (θ_{MB}), and spectral resolution (ΔV_{ch}), are summarised in Table 3.1.

In addition to these data, we also make use of a single pointing observation of the HCO^+ (1-0) line performed with the FCRAO 14m telescope towards the dust peak of L1544. These data

[1]The N_2H^+ (2-1) transition is difficult to observe (although not impossible, Daniel et al. 2007), because it falls in the vicinity of a strong atmospheric line.

have a spectral resolution of 0.07 km s^{-1} and an angular resolution of 55″, and were previously published in Tafalla et al. (1998). We refer to their paper for further details.

Table 3.1: Main properties of the lines observed at the IRAM 30m telescope.

Line	ν (GHz)[a]	$\Delta V_{\rm ch}$ (km s^{-1})	$\theta_{\rm MB}$ (″)	$F_{\rm eff}/\eta_{\rm MB}$	Int. time (h)[b]	Ref.[c]
N_2H^+ (1-0)	93.173	0.06	27	0.95/0.81	2.8	1
N_2H^+ (3-2)	279.512	0.02	11	0.87/0.49	11.3	1
N_2D^+ (1-0)	77.109	0.08	34	0.95/0.82	7.5	2
N_2D^+ (2-1)	154.217	0.04	16	0.93/0.72	6.7	2
N_2D^+ (3-2)	231.322	0.03	12	0.92/0.59	9.4	2
DCO^+ (1-0)	72.039	0.20	36	0.95/0.82	7.1	3
DCO^+ (2-1)	144.077	0.04	17	0.93/0.73	6.6	3
DCO^+ (3-2)	216.113	0.03	12	0.94/0.63	2.8	3
$HC^{18}O^+$ (1-0)	85.162	0.07	31	0.95/0.81	10.2	4

[a] The references for the rest frequencies are found in Table B.1 in Appendix B.1;
[b] Total observing time;
[c] References used for the collisional coefficients (see §3.3.2): [1] Lique et al. (2015); [2] scaled from Lique et al. (2015); [3] Pagani et al. (2012); [4] scaled from Flower (1999).

Results Figures 3.1 and 3.2 show the observed spectra at the millimetre dust peak for each transition (in black). Considering only the emission-free channels, we computed the mean rms per channel for each transition, obtaining: 0.05 K for N_2D^+ (1-0), 0.18 K for N_2D^+ (2-1), 0.26 K for N_2D^+ (3-2), 0.14 K for N_2H^+ (1-0), 0.32 K for N_2H^+ (3-2), 0.04 K for $HC^{18}O^+$ (1-0), 0.08 K for DCO^+ (1-0), 0.07 K for DCO^+ (2-1), and 0.23 K for DCO^+ (3-2). Thus, at the dust peak the observed spectra have a signal-to-noise ratio ranging from $\approx$ 4.0 to $\approx$ 40.0. Figure 3.3 shows the integrated intensity maps for each transition, computed integrating over all the hyperfine components when present.

3.3 Analysis

Our main goal is to derive the deuterium fraction across the source, and for this aim we need reliable measurements of the column density for each isotopologue. In principle, the knowledge of multiple transitions of a species can allow both its column density and excitation condition (i.e. the line excitation temperature, $T_{\rm ex}$) to be determined, as stated in §1.2. This approach, implemented in the population diagram method (Goldsmith & Langer 1999), has been extensively

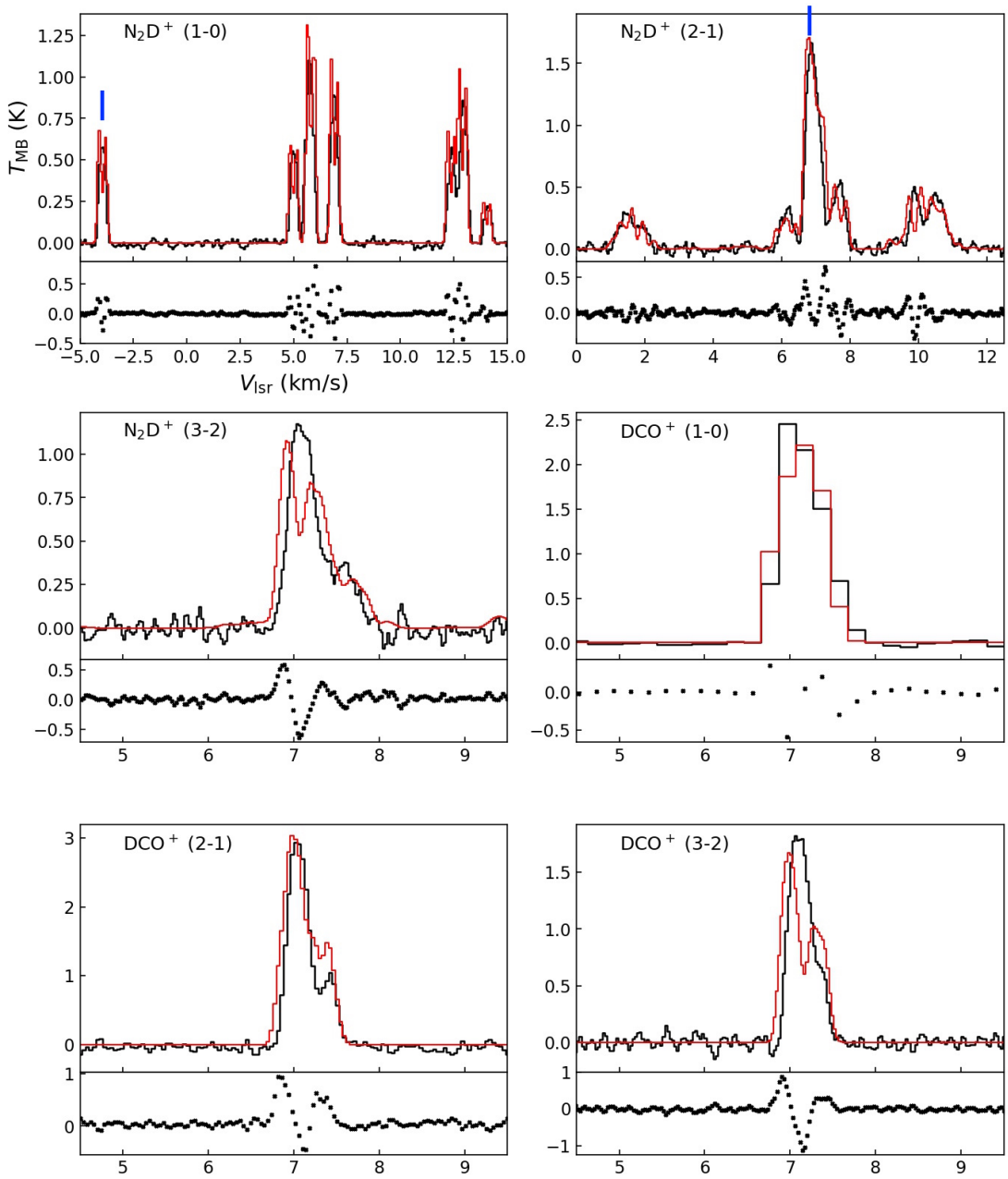

Figure 3.1: Observed spectra at the dust peak of N_2D^+ and DCO^+, with the original angular resolution (in black histograms). The transition is labelled in the upper-left corner of each panel. In red, the best-fit solution found with MOLLIE is shown overlaying the observations (see §3.3.2). Underneath each line we present the residuals of the fit (difference between the model and the observation). The vertical blue bars show which hyperfine component has been used to derive the molecular column density, when the hyperfine structure has not been neglected.

used in the literature, but it is valid only in the assumption that all the lines share the same $T_{\rm ex}$. This assumption extends to all the hyperfine components, when present. However, we know from previous studies (Daniel et al. 2006, 2013) that this is often not the case for the molecules considered here. There are multiple possible reasons for this, such as selective photon trapping in very crowded hyperfine structure, or a significant difference in critical density for the different rotational transitions of the same molecule (the Einstein coefficient A_{ul} scales with the third power of the frequency). In this case, the column density and the excitation temperatures of the different transitions are degenerate parameters, and cannot be constrained simultaneously. Therefore, an approach that does not assume LTE is needed to determine the $T_{\rm ex}$ of each transition and thus the molecular column density.

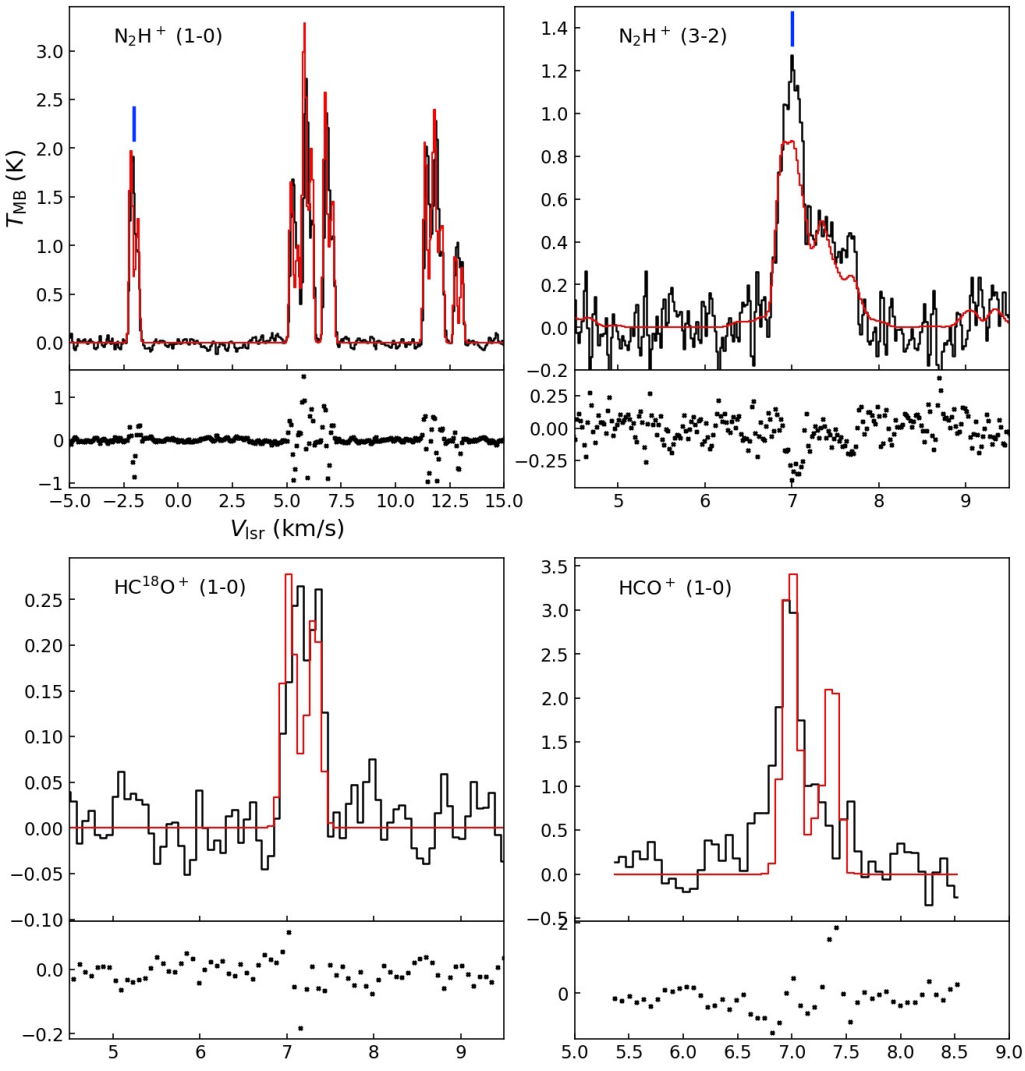

Figure 3.2: As in Figure 3.1, but for N_2H^+, $HC^{18}O^+$ and HCO^+ transitions.

A full non-LTE analysis is on the other hand not feasible on maps, because it requires the

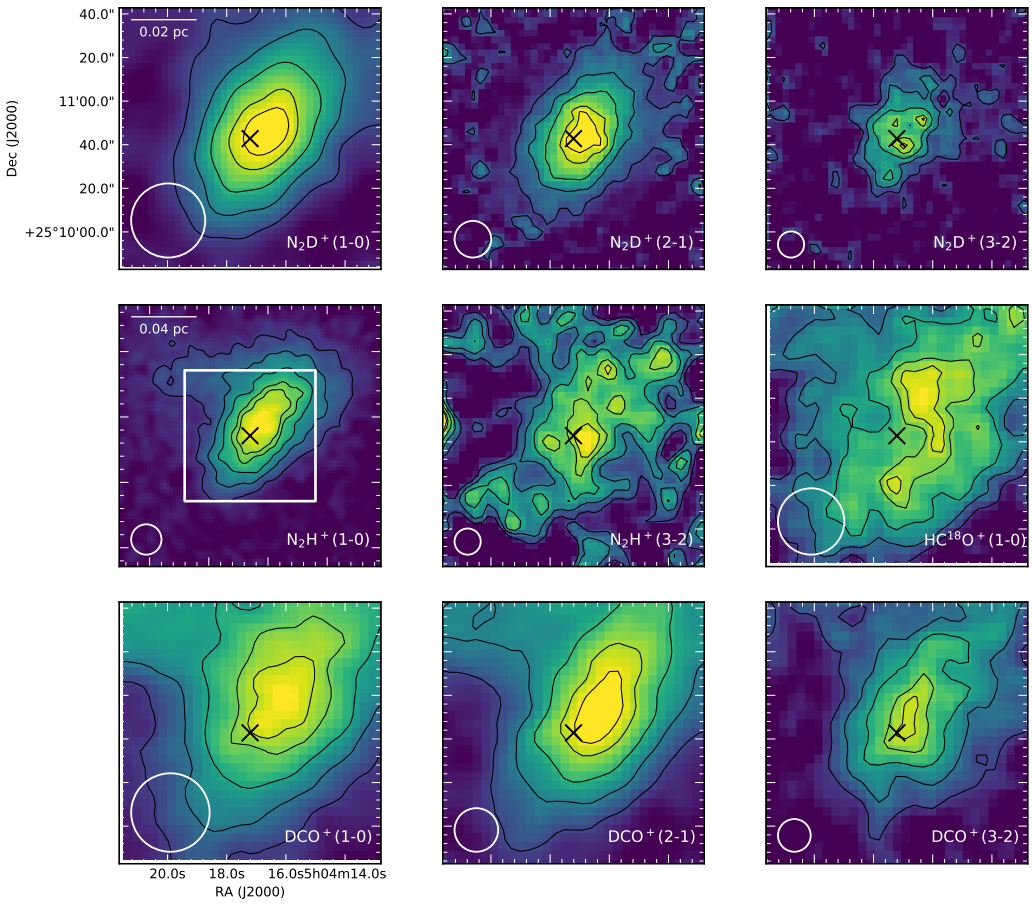

Figure 3.3: Integrated intensity maps of all the observed transitions, which are labelled in the bottom-right corners. The contours show 20, 40, 60, 80, and 90% of the peak values, which are in order from top-left to bottom-right panels: 2.0, 2.0, 0.7, 4.6, 0.7, 0.15, 1.8, 1.1, 0.7 K km s^{-1}. The black cross represents the dust peak position, and the white circle is the beam size. All the maps have the same size ($2' \times 2'$), with the exception of N_2H^+ (1-0), which is $4' \times 4'$: in this map the white rectangle shows the smaller coverage of the other transitions. Scalebars are shown in the top-left corners of the N_2D^+ (1-0) and N_2H^+ (1-0) maps.

knowledge of the full three-dimensional temperature and density structure of the core. For L1544, however, Keto et al. (2015) developed a one-dimensional physical model based on a collapsing Bonnor-Ebert sphere that provides a good fit to several molecules at the dust peak (Caselli et al. 2012; Bizzocchi et al. 2013; Caselli et al. 2017; Redaelli et al. 2018). We thus decided to model the spectra at the dust peak of the core with a full non-LTE analysis. In this way, we are able to constrain the column density of each molecule at the dust peak. At the same time, we can use the equations of radiative transfer to derive $N_{\rm mol}$ in the whole map. Since these two approaches must return the same result at the centre of the core, the $T_{\rm ex}$ (which is involved in the radiative transfer equations) is treated as a free parameter to be tuned in order to obtain the expected agreement of the two methods. The non-LTE modelling allows us to break the degen-

eracy between $N_{\rm mol}$ and $T_{\rm ex}$ mentioned in the previous paragraph. In the following sections we provide a detailed description of the required steps.

3.3.1 Chemical models

The non-LTE modelling of line emission requires the knowledge of molecular abundance ($X_{\rm mol}$) profiles. To derive these, we used the gas-grain chemical model discussed in Sipilä et al. (2015a,b), which has recently received an extensive update (Sipilä et al. 2019). Briefly, we employ the static physical core model from Keto et al. (2015), divided into concentric shells, and solve the chemical evolution separately in each shell. We then combine the results at different time steps to produce radius-dependent abundance profiles for the molecules of interest. The adopted initial conditions are summarised in Table 3.2. More information on typical model parameters can be found for instance in Sipilä et al. (2015a).

In this work we considered five different time steps: $t = 10^4$ yr, $t = 5 \times 10^4$ yr, $t = 10^5$ yr, $t = 5 \times 10^5$ yr, and $t = 10^6$ yr. We tested the influence of external UV radiation by considering three different visual extinction values for the cloud embedding the core: $A_{\rm V} = 1, 2$, or 5 mag. This amounts to a total of 15 modelled abundance profiles per molecule. We show the complete set of profiles in Appendix B.2. Simulated lines were produced based on these profiles as described in the following section.

Table 3.2: Initial abundances (with respect to the total hydrogen number density $n_{\rm H}$) used in the chemical modelling. The initial H_2 ortho/para ratio is 1.0×10^{-3}.

Species	Abundance
H_2	5.00×10^{-1}
He	9.00×10^{-2}
HD	1.60×10^{-5}
C^+	1.20×10^{-4}
N	7.60×10^{-5}
O	2.56×10^{-4}
S^+	8.00×10^{-8}
Si^+	8.00×10^{-9}
Na^+	2.00×10^{-9}
Mg^+	7.00×10^{-9}
Fe^+	3.00×10^{-9}
P^+	2.00×10^{-10}
Cl^+	1.00×10^{-9}

3.3.2 Non-LTE modelling at the dust peak

The non-LTE approach was implemented using the radiative transfer code MOLLIE (Keto 1990; Keto et al. 2004), which allows us to derive synthetic spectra from a given physical model. MOLLIE is able to treat the line overlap that occurs in a crowded hyperfine structure, such as those of N_2H^+ and N_2D^+. As an output, it also provides the molecular column density, obtained by integrating the abundance profile multiplied by the gas density, eventually convolved to a desired beam size.

The physical model of the source, as already mentioned, is taken from Keto et al. (2015). It is an unstable quasi-equilibrium Bonnor-Ebert sphere, with a central density $n_0 \approx 10^7$ cm^{-3} and a central temperature of 6.5 K and 6.3 K for the gas and the dust, respectively. Figure 3.4 shows the profiles of the main quantities for this model. Recently, Chacon-Tanarro et al. (2019) proposed a new density and (dust) temperature model for L1544, analysing new millimetre continuum observations of L1544. However, the authors did not develop a new model for the velocity field, a crucial quantity to correctly reproduce molecular spectra. Therefore, we prefer to use the previous model, which also includes the velocity profile.

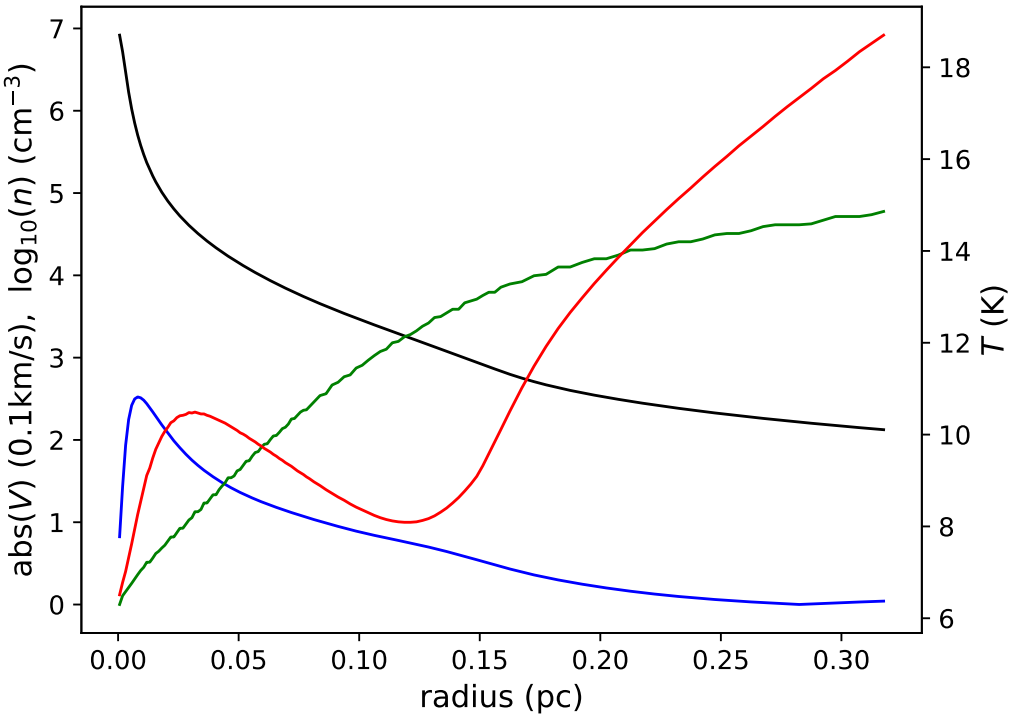

Figure 3.4: Profiles of dust temperature (green), gas temperature (red), H_2 volume density (black, in logarithmic scale), and velocity (blue, in units of 0.1 km s^{-1}) for the L1544 model developed in Keto et al. (2015). The velocity in the model is negative (it represents contraction motions), but it is shown here as positive for improved readability.

For the line radiative transfer, the collisional coefficients are of great importance, and we used

the most recent ones. When they are available only for one isotopologue, we scaled them taking into account the different reduced mass of the collision system. The collisional coefficients for N_2H^+ are taken from Lique et al. (2015), who computed them for the N_2H^+/p-H_2 system. The rates for the DCO^+/p-H_2 system were computed by Pagani et al. (2012), who take into account the hyperfine structure given by the deuterium nucleus. Finally, the collisions of HCO^+ with p-H_2 were published by Flower (1999), from which we scaled the coefficients for $HC^{18}O^+$. In all cases, the o-H_2 is neglected, which is a reasonable assumption given that the ortho-to-para ratio (OPR) in L1544 is found to be as low as OPR = 10^{-3} (Kong et al. 2015).

We tested all the 15 models described in Table 3.3. The abundance profiles produced by the chemical model often systematically overestimate or underestimate the observed fluxes, and need to be multiplied by a numerical factor to find a good agreement with the observations. However, MOLLIE requires too much computational time to allow a full sampling of the parameter space. For each molecule, we therefore proceeded as follows: first, we test all the original models, varying the evolutionary stage and the thickness of the surrounding cloud, and we select the one that best reproduces the trend of the different transitions (e.g. the ratio between the peak temperatures of the brightest component of each line). We then multiply the whole profile by a numerical factor, testing approximately five values until the observed fluxes are matched. This is considered the best fit to the observations. We want to highlight that our goal is to obtain a simultaneous fit for all molecules that is roughly consistent with the observations, and a full parameter-space search for the best possible fit within the model uncertainties is beyond the scope of the present paper. In the following text, we focus on the abundance profiles that provide the best-fit solution for each molecule. As an example, we present in §3.3.3 the resulting spectra from several of the 15 abundance profiles for N_2D^+.

Best-fit solution for the observed molecules at the dust peak

The best-fit solutions for each molecule are shown in red in Figs. 3.1 and 3.2 overlaying the observations. We also include here the analysis of a single-pointing observation of HCO^+ (1-0) performed at the dust peak (see §3.2 for details). Despite the fact that a map for this transition is not available, it is important to check the behaviour of the chemical model for HCO^+, the main isotopologue of its family. The observed spectrum of HCO^+, together with the best fit from MOLLIE, is shown in the bottom-right panel of Figure 3.2.

N_2H^+ The chemical network systematically underestimates the emission of N_2H^+, for any combination of chemical time and external visual extinction. We find that in general the spectra are best reproduced at late evolutionary times (10^6 yr), when the molecules at the centre of the core start to be affected by depletion. This allows the observed ratio between the (1-0) and the (3-2) line to be reproduced. Our simulations show that varying the thickness of the external layer does not have a significant impact on the synthetic spectra due to the high critical density of N_2H^+ whose emission arises only from the central regions ($n_{\rm crit} \gtrsim 10^5\,{\rm cm}^{-3}$; see Shirley 2015). Furthermore, N_2 is a late-type molecule that can take about ten times longer than CO to form (e.g. Hily-Blant et al. 2010). Therefore, the outer less dense envelope may not be rich enough

in N_2 for N_2H^+ to form efficiently. The abundance profile for $t = 10^6$ yr and $A_V = 1$ had to be multiplied by 2.7 to match the observed fluxes.

N_2D^+ Similar considerations to the ones made for the main isotopologue hold also for N_2D^+. The best fit is found for $t = 10^6$ yr and an external visual extinction of $A_V = 1$ mag, even though this last parameter does not significantly affect the simulated spectra (see §3.3.3 for more details). The models again tend to underestimate the observed fluxes, and we had to increase the abundance profile by a factor of 3.0 to obtain a good agreement.

HCO^+ In general, the original abundance profiles coming from the chemical network result in a better agreement with the observations of the HCO^+ isotopologues with respect to the N_2H^+ ones. The best agreement for the main isotopologue is found for the model with $t = 10^6$ yr and an external visual extinction of $A_V = 5$ mag, multiplied by a factor 0.5. This model presents a high molecular abundance in the external layers of the cores ($X_{mol} \gtrsim 10^{-7}$), which is important to correctly reproduce the strong blue asymmetry of the (1-0) line due to self-absorption (Tafalla et al. 1998).

$HC^{18}O^+$ In the chemical model, the abundance profile for the $HC^{18}O^+$ is derived from that of HCO^+ using the scaling factor valid for the local ISM $^{16}O/^{18}O = 557$ (Wilson 1999). This choice however leads to an underestimation of the observed flux. The best fit is found with the model at $t = 10^6$ yr and $A_V = 1$ mag, multiplied by 6.0. This late evolutionary stage is important to be able to reproduce the double-peak feature seen in the (1-0) spectrum, but we had to decrease the external visual extinction with respect to the main isotopologue. If the abundance of $HC^{18}O^+$ is too high in the external layers of the core, as in the models with $A_V = 5$ mag, the resulting synthetic spectra present a blue asymmetry due to the self-absorption, which is not seen in the observations.

DCO^+ The three transitions of DCO^+ are best reproduced with the model at $t = 10^6$ yr and $A_V = 1$ mag. In this case, we decrease the original abundance profile by 50% to match the observed peak temperatures.

The abundance profiles that provide the best-fit solution for each species are shown in Figure 3.5, after the multiplication for the corrective factors. The adopted models and scaling factors, together with the molecular column density computed by MOLLIE at the centre of the core (N_{mol}^{MOLLIE}), are summarised in Table 3.3. It is not surprising that the chemical model results do not provide a perfect match to the observations, and that the various lines cannot be fitted with a single model. There are many sources of uncertainty, such as the source model (density and gas/dust temperature structures), chemical modelling parameters, and rate coefficients. Our model does not consider the self-shielding of CO, which would affect the HCO^+ abundance in the outer core, for example. A detailed parameter-space exploration of the abundance profiles is beyond the scope of the present paper.

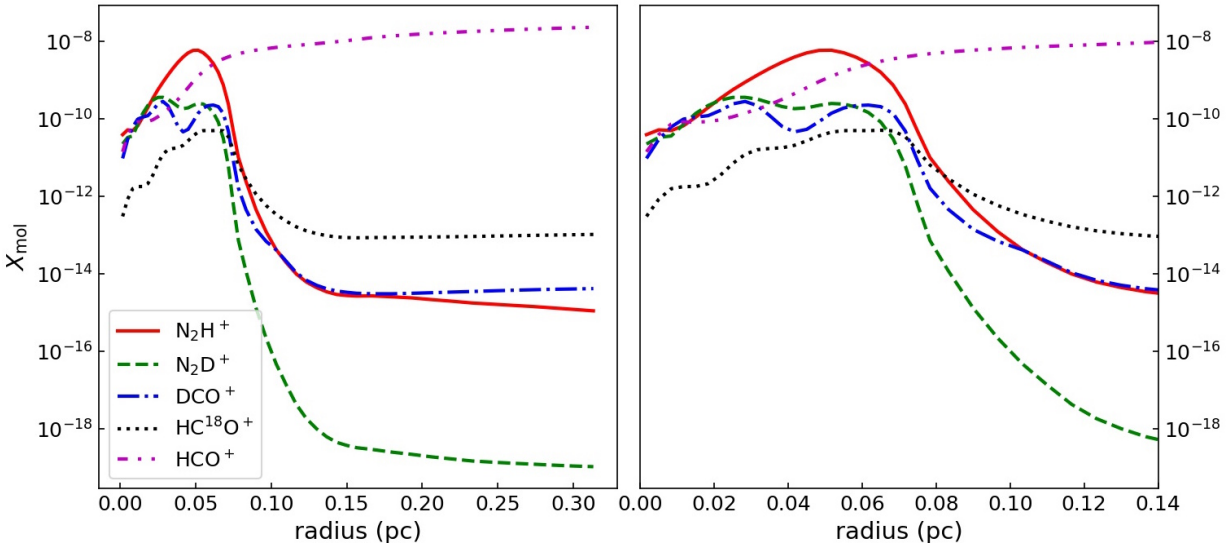

Figure 3.5: *Left panel:* Molecular abundances that provide the best fit to the spectra at the dust peak for the different species as a function of the core radius. *Right panel:* Zoom-in of the molecular abundances in the inner 0.14 pc.

3.3.3 N_2D^+ depletion

In this section, we analyse in detail the case of N_2D^+, showing the non-LTE radiative transfer results for 6 out of the 15 abundance profiles that we tested at the dust peak. The abundance profiles are all multiplied by a factor of 3.0 to allow an easier comparison with the observations. The obtained spectra are shown in Figure 3.6 and 3.7 overlaying the observations.

The rows of Figure 3.6 and the first one from the top in Figure 3.7 show increasing evolutionary times, keeping the external extinction fixed to $A_V = 1$ mag. The difference between the observations and the model can be quantified by comparing the relative ratio of the peak temperatures of the three lines. In the observations, this ratio is $T_{peak}(1-0) : T_{peak}(2-1) : T_{peak}(3-2) = 1 : 1.5 : 1.1$. In the models with the earlier times ($t = 5 \times 10^4$ and $t = 10^5$ yr), the obtained ratios are 1 : 3.3 : 2.5 and 1 : 2.6 : 1.9, respectively. This means that these abundance profiles overestimate the (2-1) and (3-2) with respect to the (1-0) line. In the later evolutionary stages ($t = 5 \times 10^5$ and $t = 10^6$ yr), the ratios are 1 : 1.2 : 0.7 and 1 : 1.3 : 0.8, closer to the observed one. This trend can be understood by looking at the behaviour of the different abundance profiles in the inner 10000 AU, shown in Figure 3.8. At earlier times, the N_2D^+ abundance peaks within the central 2000 – 3000 AU, where the molecular hydrogen density is $n(H_2) \gtrsim 10^5$ cm^{-3}. Since the critical densities of the (1-0), (2-1), and (3-2) transitions are $n_{crit} = 7.6 \times 10^4$ cm^{-3}, 8.7×10^5 cm^{-3}, and 3.8×10^6 cm^{-3}, respectively (Shirley 2015), this is also the region where the (2-1) and the (3-2) lines are emitting the most. At later evolutionary times, N_2D^+ is depleted and the abundance decreases by more than a factor of five for $r \lesssim 2000$ AU. This is due to the fact that its precursor species, N_2, starts to freeze-out onto dust grains, and as a consequence the formation rate of N_2D^+ is reduced. The N_2D^+ abundance peak moves outwards to $r \approx 5000$ AU, where $n(H_2) \approx 5 \times 10^4$ cm^{-3}. Therefore, the (2-1) and (3-2) lines are less excited, while the (1-0)

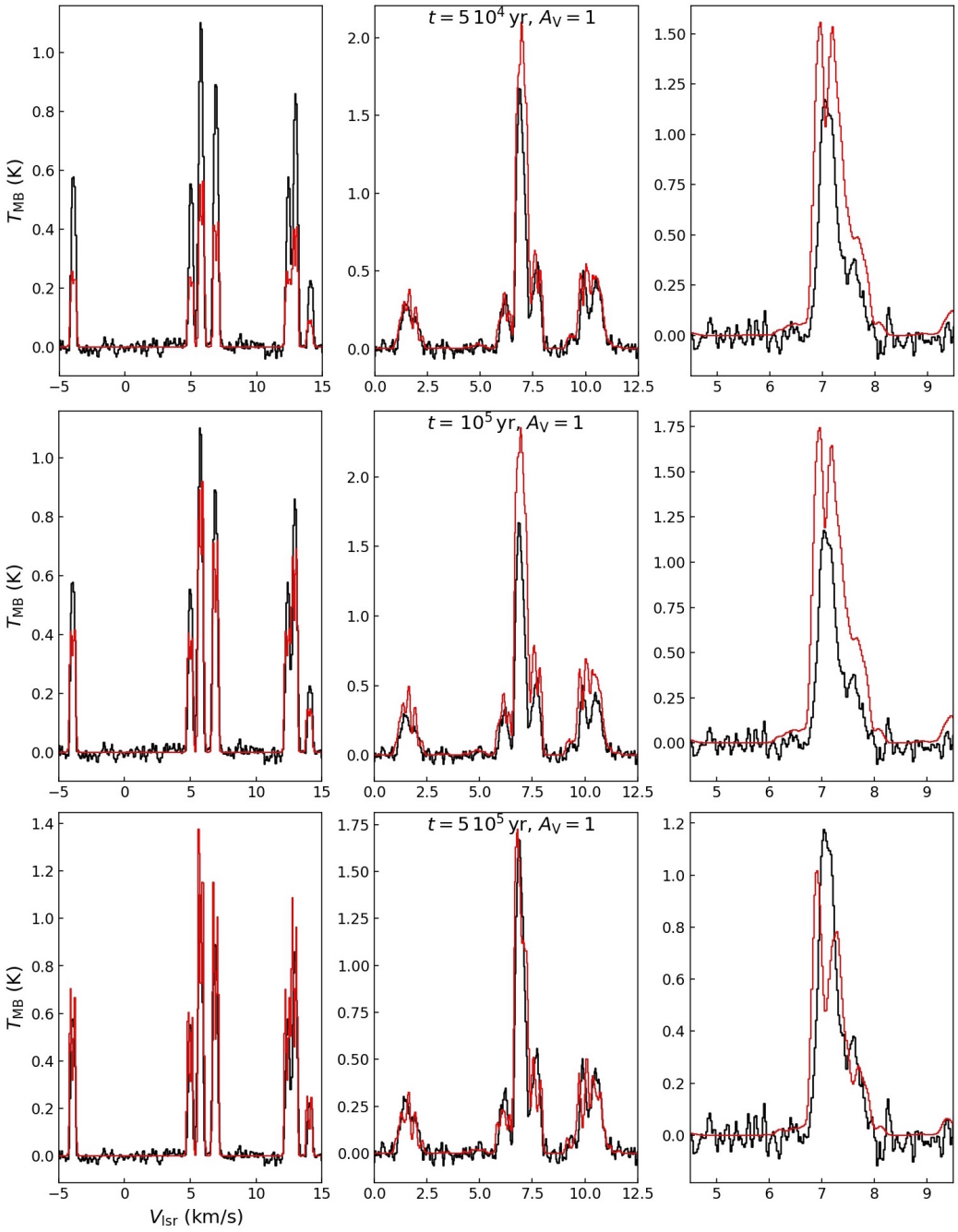

Figure 3.6: Results of the line radiative transfer for three chemical models on the three transitions of N_2D^+, respectively (1-0), (2-1), and (3-2) from left to right in each panel. The external visual extinction is fixed ($A_V = 1$), whilst the evolutionary time increases from top to bottom. The synthetic spectra are shown with red histograms overlaying the observations (in black).

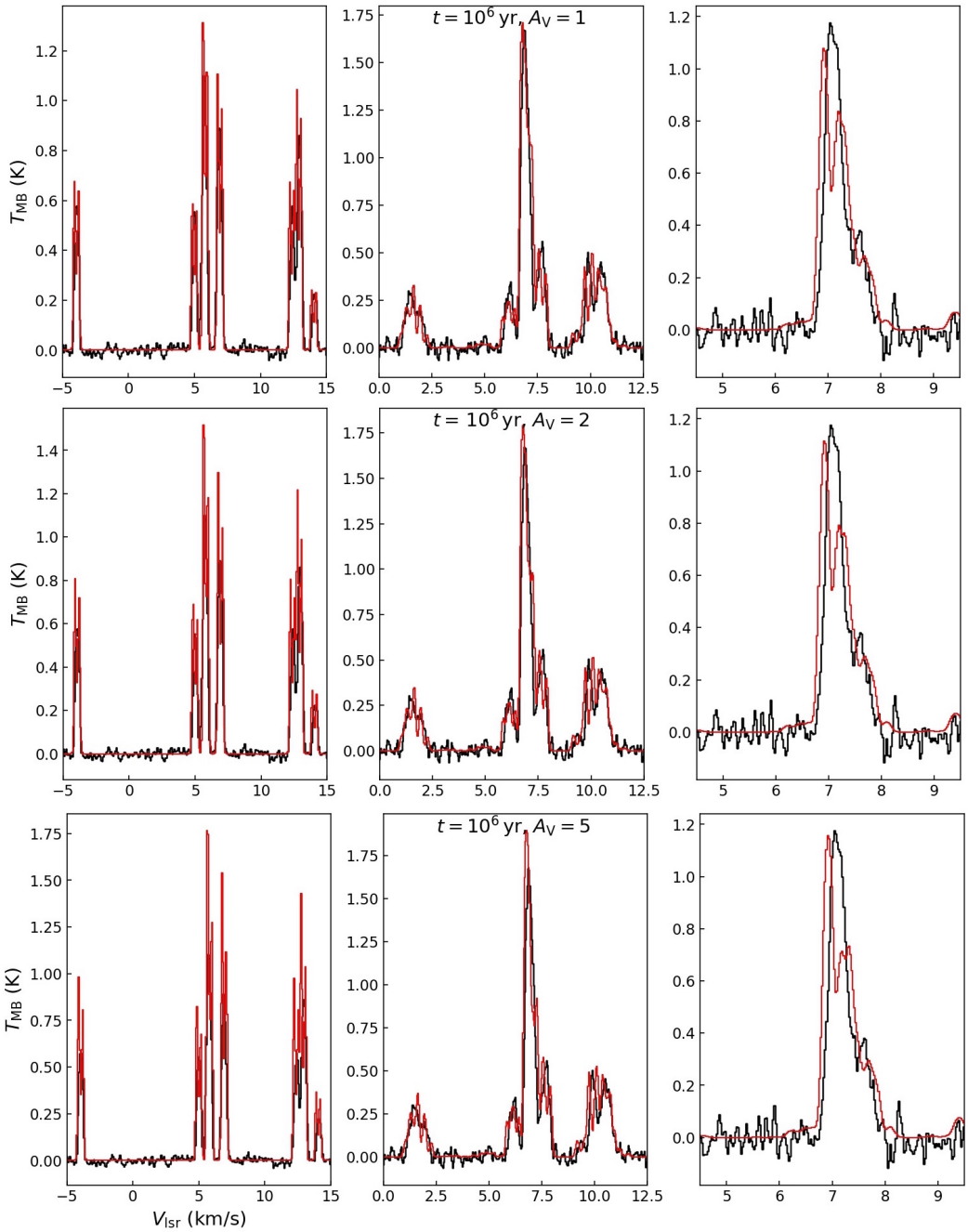

Figure 3.7: Same as in Figure 3.6, but for a fixed evolutionary stage ($t = 10^6$ yr) and different external visual extinction.

flux keeps rising. This is the first observational confirmation of N_2D^+ partial depletion in cold and dense environments.

We now focus on the influence of the external embedding layer, keeping the evolutionary stage fixed ($t = 10^6$ yr) and varying the external visual extinction (see Figure 3.7). The synthetic

spectra are not very sensitive to this change, both in the flux level and in the spectral profiles, especially concerning the (2-1) and (3-2) lines. This is again due to a combination of molecular abundance and excitation conditions. In fact, increasing A_V significantly changes the abundance only for $r \gtrsim 10000$ AU, where the molecular hydrogen density is $n(H_2) \lesssim 10^4\,cm^{-3}$. Therefore, the high-frequency transitions are not significantly affected by the change of A_V.

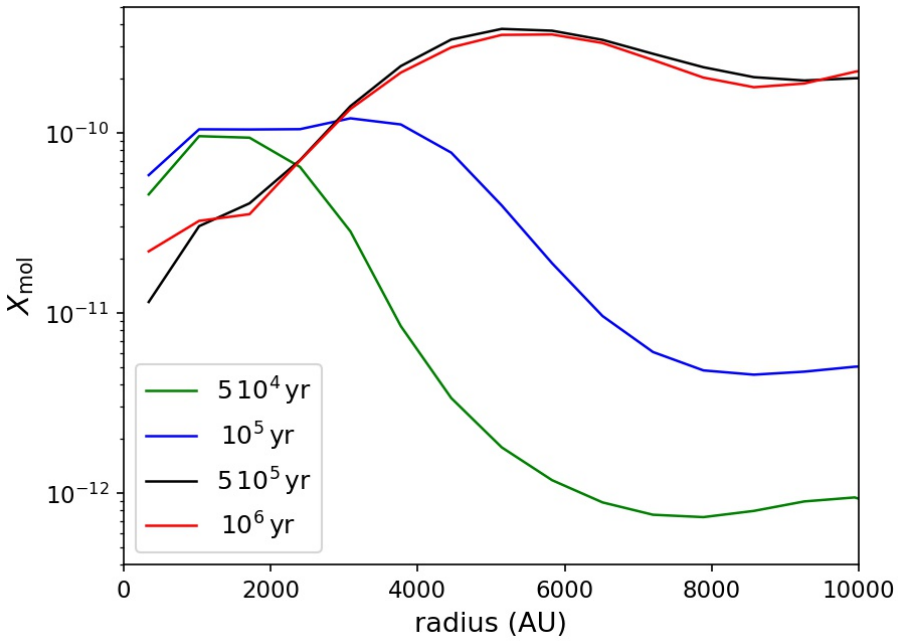

Figure 3.8: Zoom-in of the central 10000 AU of the N_2D^+ abundances predicted by the chemical code for $A_V = 1$ mag at four evolutionary stages: $t = 5\,10^4$ yr (green), $t = 10^5$ yr (blue), $t = 5\,10^5$ yr (black), and $t = 10^6$ yr (red). The abundance profiles are multiplied by a factor of 3.0.

3.3.4 Column density and deuteration maps

In the following, we describe how we derive the column density map of each species, knowing the N_{mol} value at the centre of the core from the non-LTE modelling, via the radiative transfer equations. The spectra of the analysed molecules greatly differ due to their opacity properties and hyperfine structure. For instance, we have optically thin transitions ($HC^{18}O^+$ (1-0)), or optically thick ones (HCO^+ (1-0)). Some species present crowded hyperfine structures (such as N_2H^+ and N_2D^+), while others show a much simpler profile (e.g. DCO^+, where the hyperfine splitting due to the deuterium spin is not detectable at the given spectral resolution; Caselli & Dore 2005). As a result, we tackle the problem of deriving the column density maps by developing a specific approach for each species individually. In all cases, we make use of the following well-known relations already introduced in 1.2.2:

$$T_{MB} = \eta_{bf} \left[J_\nu(T_{ex}) - J_\nu(T_{bg}) \right] (1 - e^{-\tau_\nu}) \ , \qquad 3.1$$

and

$$\tau_{\nu}^{\rm peak} = \sqrt{\frac{\ln 2}{16\pi^3}} \frac{c^3 A_{ul} g_u}{\overline{\nu}^3 Q(T_{\rm ex}) \Delta V} \exp\left(-\frac{E_u}{k_{\rm B} T_{\rm ex}}\right)\left(\exp\left(\frac{h\overline{\nu}}{k_{\rm B} T_{\rm ex}}\right) - 1\right) N_{\rm mol} \ . \tag{3.2}$$

In Eq. 3.1, we assume that the beam filling factor is equal to 1.0 due to the large extension of the core emission compared to the beam size. Eq. 3.2 is derived from Eq. 1.26, assuming that the optical depth of the line τ_ν has a Gaussian shape with standard deviation $\sigma_\tau = \Delta V/2\ln(2)$, centred at the transition frequency $\overline{\nu}$. Equation 3.2 depends on several spectroscopic constants: the line frequency ν , the upper state energy E_u and degeneracy g_u, the Einstein coefficient A_{ul} , and the partition function Q. This latter equation holds both for an entire rotational transition and for an individual hyperfine component, depending on the splitting considered for the levels in the calculation of the partition function and the corresponding level degeneracy used. We emphasise that Eqs. 3.1 and 3.2 represent the integrated form of the (differential) radiative transfer equations. This is the appropriate approach since observations yield essentially integrated quantities (such as column density, fluxes, etc.).

Table 3.3: Summary of the models that provide the best fit of each molecule, with the adopted scaling factor for the abundance profile.

Molecule	Chemical model for $X_{\rm mol}$	Scaling factor	$N_{\rm mol}^{\rm MOLLIE}$ [a] 10^{12} cm^{-2}	$T_{\rm ex}$ [b] line[c]	K
N_2H^+	$t = 10^6$ yr, $A_V = 1$	2.7	17	(1-0)	5.6
				(3-2)	5.0
N_2D^+	$t = 10^6$ yr, $A_V = 1$	3.0	3.5	(1-0)	7.7
				(2-1)	5.0
				(3-2)	4.8
$HC^{18}O^+$	$t = 10^6$ yr, $A_V = 1$	6.0	0.18	(1-0)	5.5
DCO^+	$t = 10^6$ yr, $A_V = 1$	0.5	2.5	(1-0)	7.8
				(2-1)	5.8
				(3-2)	5.7

[a] Column density predicted by MOLLIE at the dust peak, computed integrating the molecular abundance, multiplied by the H_2 volume density, along the line of sight and convolving to the beam size of the observation;
[b] Excitation temperature values for each line derived as described in the main text and used to derive the column density maps;
[c] The transitions are labelled with the rotational convention (J-J'), even when a single hyperfine component is used.

Column density maps of individual molecules

To derive the column density of each molecule, we first smooth the angular resolution of the high-frequency transitions to the one with the largest beam. We then fit $N_{\rm mol}$ pixel by pixel, minimising the residuals between the values of $T_{\rm MB}$ obtained through Eqs. 3.1 and 3.2 and the observed peak temperatures for all the available transitions.The observed peak temperatures are obtained with a Gaussian fit to the observed spectra, deriving in this way both $T_{\rm MB}$ and ΔV at the same time. When the line presents hyperfine structure, we select a single component. The choice of the $T_{\rm ex}$ value to be used in Eqs. 3.1 and 3.2 is made so that this approach at the centre of the core agrees with the $N_{\rm mol}$ value obtained with MOLLIE, within the uncertainties. The $T_{\rm ex}$ values obtained in this way are used to model the whole map. The chosen method to select $T_{\rm ex}$ for each line and the assumption that this quantity is spatially constant are discussed in detail in Appendix B.3. We now describe in detail on which spectral features we focus to fit $N_{\rm mol}$ for each species.

N_2H^+ The (1-0) transition of N_2H^+ presents a single, isolated component at the high-frequency end of its spectrum, which is a perfect candidate for our analysis, also providing reliable values for the line width. On the contrary, the hyperfine structure of the (3-2) line collapses in a very complicated structure, with a strong shoulder on the red side. For this transition we thus use the peak temperature of the observed spectra combined with the ΔV value obtained from the analysis of the (1-0) transition[2]. For the spectroscopic constants needed in Eq. 3.2, we selected the brightest hyperfine component according to the spectroscopic catalogues (see Appendix B.1).

N_2D^+ The N_2D^+ (1-0) transition also presents a single isolated component suitable to our purposes. This is not the case for the other two transitions. For the (2-1) line, we find that the best solution is to consider the brightest feature of the spectra, which is composed by four components separated in total by only ≈ 90 kHz (see Appendix B.1 for details). We fit a single Gaussian to this spectral feature in the observations, and we use the additive property of Eq. 3.2, according to which $\tau_\nu^{\rm tot} = \sum_i \tau_\nu^i$, where i labels the hyperfine components. Finally, in the (3-2) spectra the hyperfine structure is closely blended, and therefore we consider it a single line[3].

$HC^{18}O^+$ This is the only molecule for which we have a single transition, and thus we cannot fit $N_{\rm mol}$ using the procedure described above. However, this transition is optically thin, as confirmed by the radiative transfer performed by MOLLIE, which predicts a maximum value of $\tau_\nu \approx 0.20$ at the dust peak. Therefore, we use the optically thin approximation of Eqs. 3.1 and 3.2, reported in §1.2.2. We therefore fit a Gaussian to the spectrum in each pixel; we subsequently compute its integrated intensity W and then derive $N_{\rm mol}$ using Eq. 1.28.

[2]Several other approaches, such as trying to fit a Gaussian avoiding the red-wing component, were tested but proved to be unsuccessful.

[3]We tested this hypothesis at the emission peak by comparing our results with those coming from fitting the complete hyperfine structure using GILDAS/CLASS package. We find consistent results within our uncertainties.

DCO^+ The spectra of DCO^+ are the simplest to analyse since the hyperfine structure due to the deuterium atom is compact if compared to our spectral resolution. We consider the three transitions as single lines, fit a Gaussian profile to each of them, and fit the molecular column density minimising the residuals between the synthetic spectra and the Gaussian fits to the observations.

Figure 3.9 shows the column density maps obtained for each molecule as described immediately above, while their peak values are summarised in Table 3.4. Our results are consistent with those of Caselli et al. (2002c), which are quoted to be accurate within a factor of two. We however highlight that a direct comparison with other works is difficult (see §3.4). We report in Appendix B.1 the spectroscopic values used for each transition. The values of T_{ex} that ensure that the above method provides the same peak column density as computed by MOLLIE are reported in the last column of Table 3.3. These values confirm that the assumption of a single T_{ex} value for all transitions is incorrect, since the (3-2) lines present excitation temperatures that are ≈ 2 K lower than the respective (1-0) ones. For most transitions, T_{ex} is lower than the gas kinetic temperature, suggesting that many of the detected lines are subthermally excited.

One strong assumption of our method is the line Gaussianity. This neglects any spectral asymmetry due for example to the contraction motions, which are clearly visible in some spectra. We want to emphasise that any improvement of our analysis is strongly related to the development of a better physical model for L1544. In fact, the one-dimensional model of Keto et al. (2015) allows us to solve the radiative transfer problem only at the dust peak, since the fact that L1544 is not spherically symmetric becomes critical moving away from the central point. Since our goal is to investigate the deuteration properties in the whole extended core, we are forced to make further assumptions and simplifications.

Table 3.4: Peak values of the column densities for the different molecules.

Molecule[a]	N_{mol}/cm^{-2}
N_2H^+	$1.8^{+1.1}_{-0.3} \times 10^{13}$
N_2D^+	$3.5^{+2.0}_{-1.0} \times 10^{12}$
$HC^{18}O^+$	$1.7^{+0.1}_{-0.1} \times 10^{11}$
HCO^+	$9.5^{+0.6}_{-0.6} \times 10^{13}$
DCO^+	$2.6^{+1.2}_{-0.8} \times 10^{12}$

[a] The column density of HCO^+ is derived from the one of $HC^{18}O^+$ using the standard isotopic ratio $^{16}O/^{18}O = 557$ (see main text).

Once the column density maps are ready, we can compute the deuterium fraction, dividing the column density of the D-bearing species and that of the main isotopologue pixel by pixel. First, the beam sizes of the maps are matched to allow a fair comparison. The column density of HCO^+ is derived from that of $HC^{18}O^+$ using the standard isotopic ratio: $N_{mol}(HCO^+) = N_{mol}(HC^{18}O^+) \cdot 557$. Figures 3.10 and 3.11 show the resulting images for the D/H ratio.

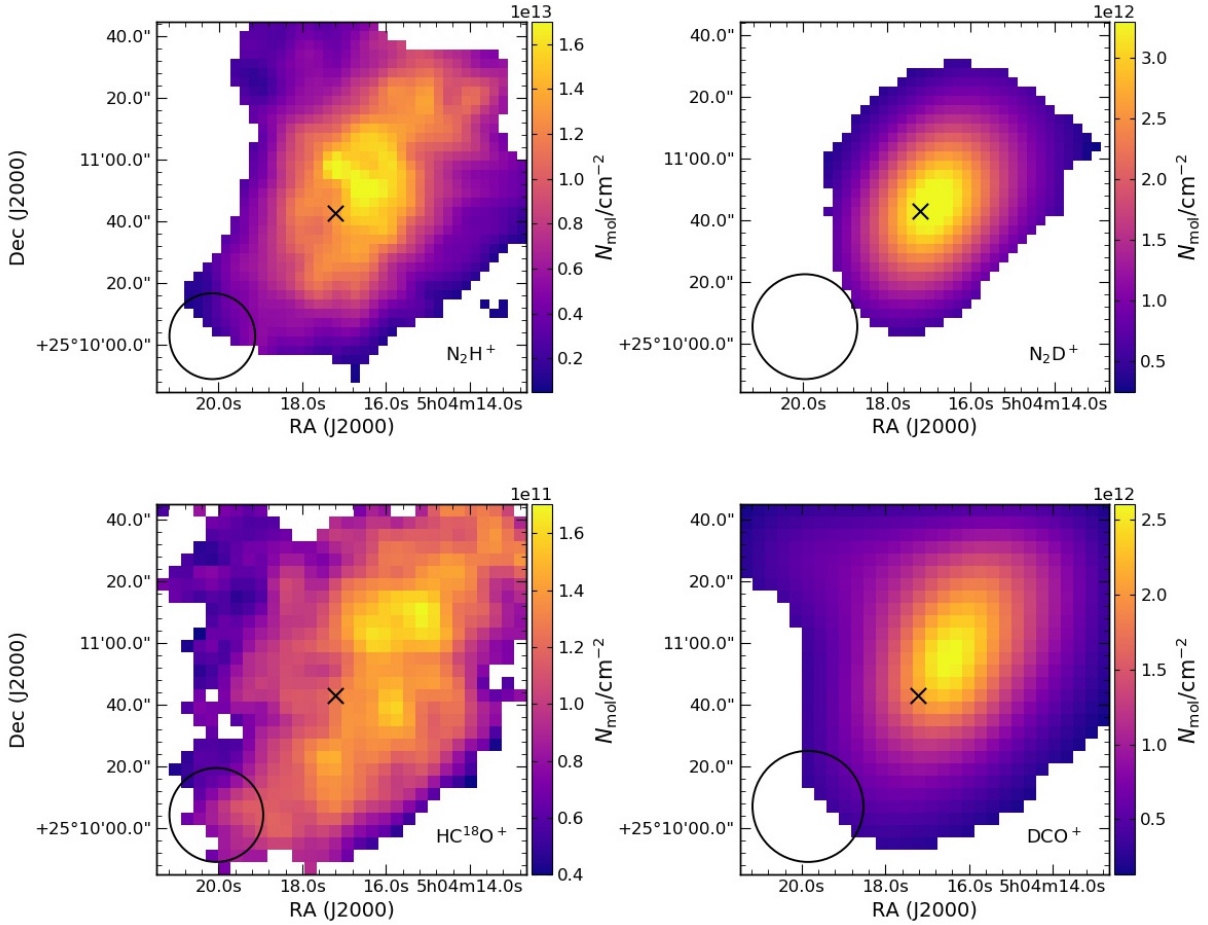

Figure 3.9: Column density maps obtained for each molecule (labelled in the bottom-right corner of each panel). The beam sizes are shown in the bottom-left corners. The black cross represents the position of the millimetre dust peak.

Evaluation of the uncertainties

In the approach adopted to compute the molecular column densities, the main source of uncertainty is found in the excitation temperature values. In fact, they depend on several other parameters, such as the assumed physical and chemical models. We choose a conservative approach, and decide that the T_{ex} values in Table 3.3 are accurate within 0.5 K. This choice is supported by the following considerations. First of all, such a variation in T_{ex} translates into an average variation of 20 $\sim$ 30% in the computed column densities, which corresponds to an equal variation of the molecular abundance. We ran MOLLIE again, modifying the abundance profiles by 30%, and the resulting modelled spectra deviate significantly from the observed ones. This means that our data are indeed sensitive to a variation of 0.5 K in T_{ex}. Furthermore, this variation in T_{ex} is the limit suggested by our analysis on the possible spatial variation of this quantity (see Appendix B.3).

The column density maps, computed with the T_{ex} values modified by 0.5 K, therefore provide

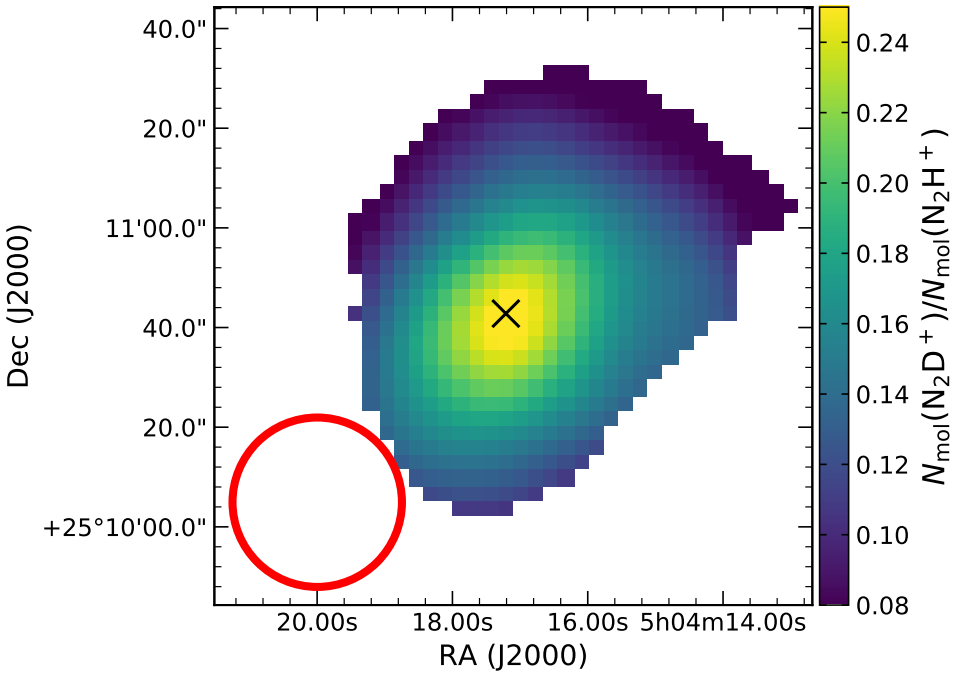

Figure 3.10: D/H ratio obtained for N_2H^+ in L1544. The beam is shown in red, and the black cross represents the dust peak position.

the sought-after uncertainties. The uncertainties on the D/H ratios are derived through standard error propagation from the ones on the molecular column density. The median relative errors are 41% for $D/H_{N_2H^+}$ and 22% for D/H_{HCO^+}. The lower mean uncertainty on the HCO^+ results depends on how sensitive N_{mol} is to T_{ex} variations, according to Eq. 3.2. The column density of N_2D^+, for example, is more heavily affected than that of $HC^{18}O^+$ by a T_{ex} change of 0.5 K, and therefore its relative error is higher.

3.4 Discussion

The column density maps presented in Figure 3.9 show that different molecules exhibit different morphologies. In particular, one can see differences in the position of the column density maxima with respect to the dust peak. Both $N_{mol}(N_2H^+)$ and $N_{mol}(N_2D^+)$ peak close to the millimetre dust peak, and while the former has a more extended distribution, the latter is highly concentrated in the densest part of the core (as already noted in Caselli et al. 2002c). The abundance profiles in Figure 3.5, despite referring to a one-dimensional core model, confirm these trends. The peak of N_2H^+ abundance is found at a larger radius with respect to N_2D^+.

Despite the fact that N_2D^+ is concentrated in the central region, it is interesting to notice that the chemical model that provides the best fit to its transitions predicts some extent of molecular depletion due to freeze-out, as described in §3.3.3. This is to our knowledge the first time that

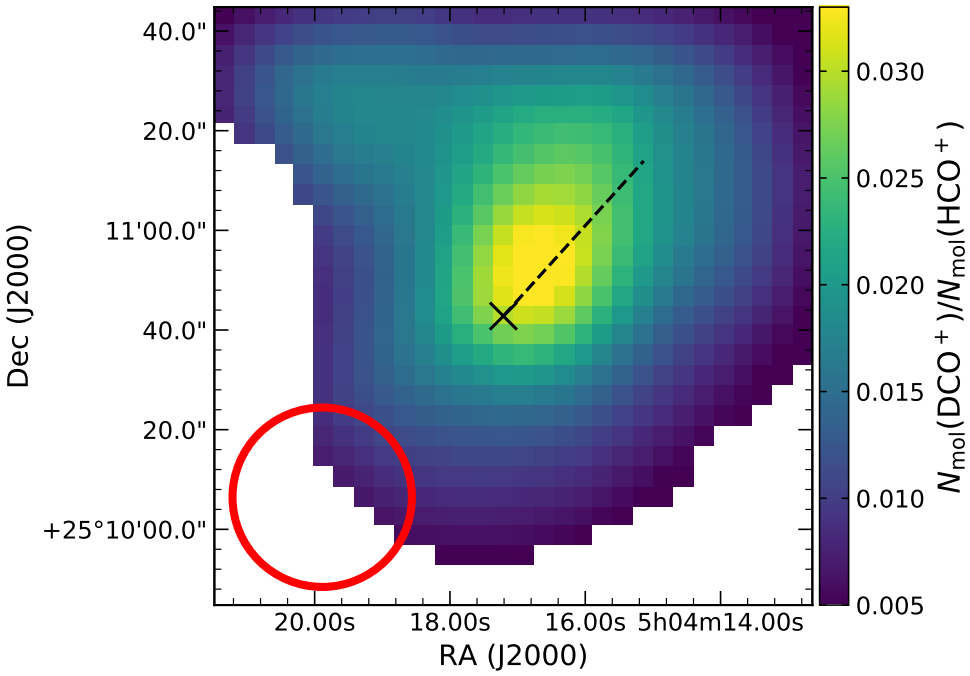

Figure 3.11: Deuterium fraction of HCO^+ obtained in L1544. The beam is shown in red, and the black cross represents the dust peak position. The dashed line is the cut used to produce Figure 3.13.

N_2D^+ depletion, which is often predicted by chemical models, is confirmed by observational data. We are aware that our spatial resolution (35″ corresponds to ≈ 0.03 pc at the distance of L1544) is not sufficiently high to investigate this point exhaustively. However, the fact that we need a model with some central depletion to reproduce the observed spectra is clear confirmation. As a further test, we tried to model all the N_2H^+ and N_2D^+ spectra with MOLLIE using a flat abundance profile with no depletion, which only decreases in the outskirts of the source due to photodissociation. This model is able to accurately reproduce the (1-0) lines, but overestimates the fluxes of the higher-J transitions, which have a higher critical density and are thus sensitive to the abundance in the central part of the core. Furthermore, we derived the molecular column density of N_2D^+ analysing only the (3-2) transition in the optically thin approximation, using Eq. 1.28. This allows us to obtain a map of higher resolution, since the beam size at 1 mm is ≈ 12″ (corresponding to ≈ 0.01 pc at L1544 distance). The results are shown in Figure 3.12. Understandably, the absolute values of N_{mol} are different from those obtained via our complete analysis. However, in this case we are more interested in the morphology of the molecular distribution. Figure 3.12 shows that N_2D^+ column density is not particularly concentrated around the centre of the core and that it does not peak exactly at this position. Instead, it presents multiple secondary peaks, which are significant with respect to our noise level. These features support our hypothesis of an abundance profile which is not increasing or constant in the innermost part of the core, but that on the contrary is decreasing due to the depletion of the molecule from the

gas phase.

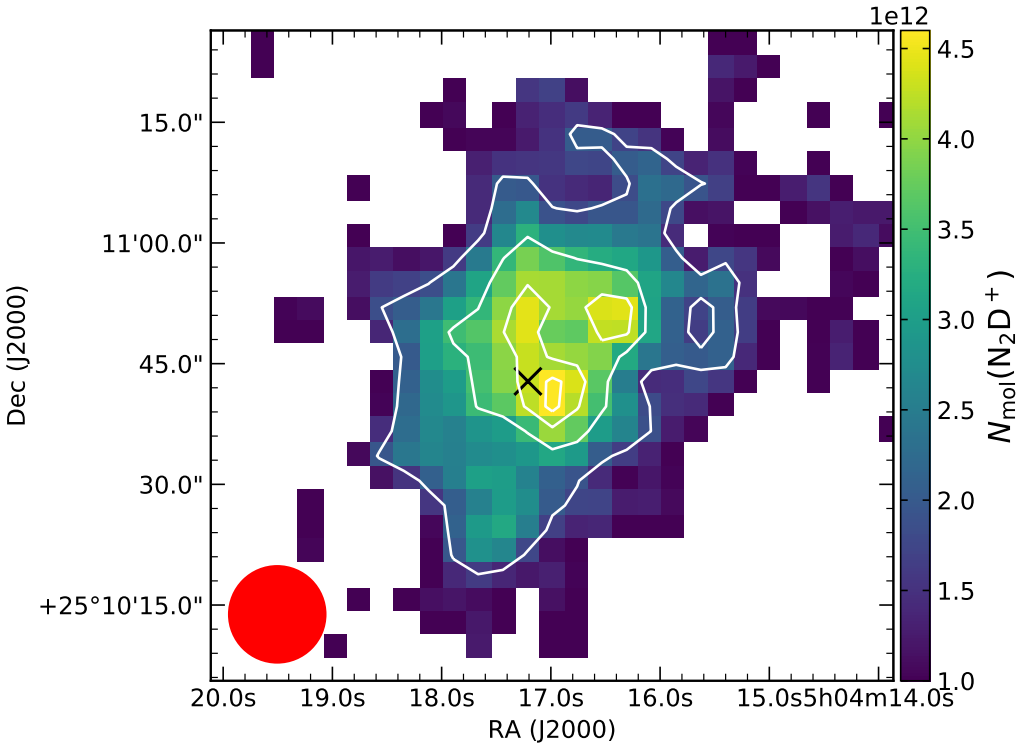

Figure 3.12: N_2D^+ column density obtained analysing only the (3-2) transition, thus obtaining a spatial resolution that is almost three times higher with respect to the corresponding panel in Figure 3.9. The white contours represent the integrated intensity of the line, at levels of $[5, 9, 11, 12]\sigma$ ($1\sigma = 0.05\,\mathrm{K\,km\,s^{-1}}$).

Future observational follow-ups with higher resolution will help us to better understand the extent of N_2H^+ and N_2D^+ depletion, which is of particular interest since both molecules (and N_2D^+ in particular) are expected to preferentially trace the central regions of prestellar cores. Moreover, this provides clues on the freeze-out of the parent molecule N_2, which is not observable in cold and dense environments. It is also interesting to mention that ammonia, in comparison, does not exhibit any sign of depletion at the centre of L1544 (Crapsi et al. 2007).

The DCO^+ morphology is also relatively concentrated, similarly to N_2D^+, but its peak is shifted in the northwest direction. This is confirmed by the integrated intensity maps shown in the bottom panels of Figure 3.3. In particular the integrated intensity map for DCO^+ (3-2), which has the best angular resolution (12″), shows that the molecular emission peaks $\approx 15''$ away from the dust peak. This morphology is due to the counter-balance of two chemical mechanisms: namely (i) the freeze-out onto dust grains of the C- and O-bearing species, which makes them depleted at very high densities and low temperatures (Caselli et al. 1999; Tafalla et al. 2002); and (ii) the fact that deuterated molecules prefer exactly these physical conditions, as described in §3.1. This explanation additionally gives a straightforward interpretation of the $N_{mol}(HC^{18}O^+)$

map. This molecule presents the highest depletion level of those analysed here, as also confirmed by the abundance profile predicted by our chemical network. Its column density peak is found $\approx 35''$ away from the dust peak, in the northwest direction.

Another interesting point is that, as described in §3.3.2, we could not reproduce the HCO^+ and $HC^{18}O^+$ (1-0) spectra using the same abundance profile, simply scaled by the oxygen isotopic ratio. To reproduce the strong blue asymmetry shown by the main isotopologue, we needed to adopt a model with a thick envelope, where the molecule is very abundant ($X_{\rm mol}(HCO^+) \gtrsim 10^{-7}$). On the contrary, if we use this dense outer layer also for the rare isotopologue, we are not able to correctly fit the spectral profile, since we overestimate the $HC^{18}O^+$ abundance in the envelope. We believe that this is a consequence of the selective photodissociation of $HC^{18}O^+$. While the main isotopologue is so abundant that it is able to self-shield effectively at large radii, the $HC^{18}O^+$ abundance is not high enough to block the photodissociating photons that can therefore penetrate deeper into the core.

The morphological features previously described for the different column density maps reflect directly on the deuterium fraction maps. Since the D-bearing isotopologues peak closer to the dust peak than the corresponding main species, the D/H maps exhibit a compact morphology around the dust peak. The maximum values that we found are $D/H_{N_2H^+} = 0.26^{+0.15}_{-0.14}$ and $D/H_{HCO^+} = 0.035^{+0.015}_{-0.012}$, which are in good agreement with previous estimations (see e.g. Caselli et al. 2002c; Crapsi et al. 2005). It is however difficult to make a direct comparison with previous works. For example, Caselli et al. (2002c) used a constant $T_{\rm ex}$ approach with different excitation temperatures with respect to ours (e.g. $T_{\rm ex} = 5.0$ K for N_2H^+ and 4.9 K for N_2D^+). These latter study also lacked some important transitions such as N_2D^+ (1-0) and DCO^+ (1-0), their frequencies being too low for the receivers used at the time.

We find that N_2H^+ is more deuterated than HCO^+, as expected since N_2 (and N_2H^+ in turn) is a late-type molecule and is less affected by depletion (Nguyen et al. 2018). Therefore, N_2H^+ appears in conditions where CO is already depleted and H_2D^+ is more abundant. The deuteration level of N_2H^+ decreases from 26% to 10% in $45''$, while D/H_{HCO^+} varies from 3.5% to 2.0%. Figure 3.13 shows the D/H values for the two tracers as a function of radius for a cut crossing the dust peak and the D/H_{HCO^+} maximum, shown with a dashed line in Figure 3.11. The deuteration level thus decreases faster for N_2H^+ than for HCO^+, mainly as a consequence of the fact that DCO^+ is more extended than N_2D^+ with respect to their main isotopologues and that HCO^+ and DCO^+ are more affected by freeze-out in the core centre compared to N_2H^+ and N_2D^+.

3.5 Conclusions

In this work we performed a detailed analysis of multiple transitions of N_2H^+, N_2D^+, $HC^{18}O^+$, DCO^+ with recent high-sensitivity observations, which allow us to investigate the molecular properties with high-S/N data across the whole L1544 core. Using a non-LTE approach combined with the molecular abundances computed with chemical models, we derived the excitation conditions of the molecules at the dust peak. Our resulting $T_{\rm ex}$ values confirm that the assumption of a common excitation temperature for different rotational transitions or even for different hyperfine components does not hold for these molecular ions. The molecular abundances derived

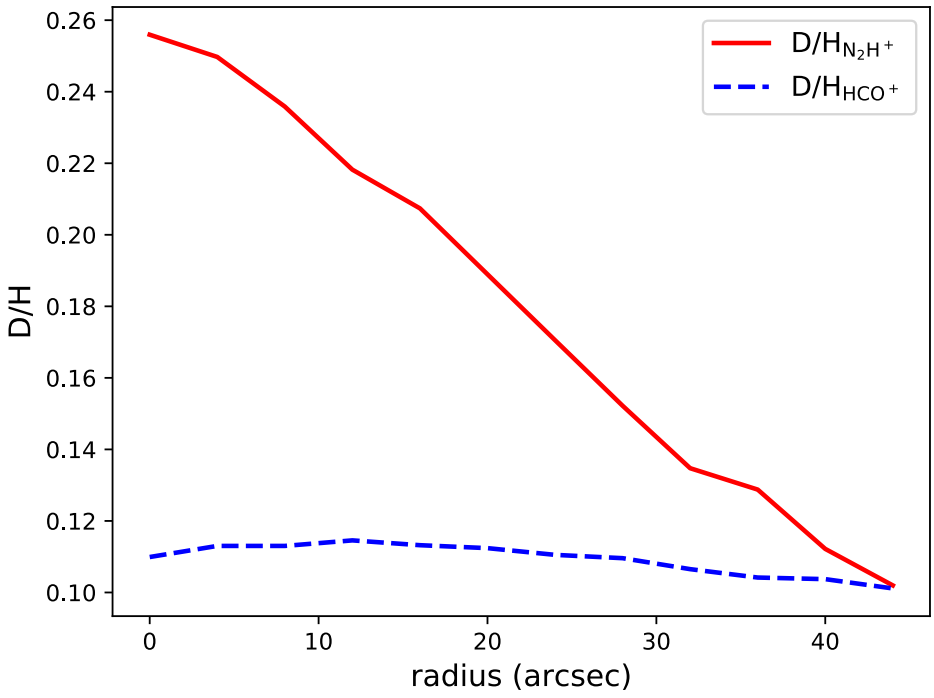

Figure 3.13: Comparison of the trends of $D/H_{N_2H^+}$ (red) and D/H_{HCO^+} (blue) along the cut shown in Figure 3.11. The data points of HCO^+ have been shifted upwards by 0.10 for readability.

with our chemical models are in general not able to reproduce the observations, especially for N_2H^+ and N_2D^+ for which we had to increase the predicted abundance by up to 300% to obtain a good fit to the observed spectra. Despite these discrepancies, we are able to draw some important conclusions.

All the analysed molecules show some level of depletion in the very central parts of the core due to freeze-out onto the dust grains. This phenomenon is most prominent for HCO^+ and its isotopologues, but it is seen also for N_2H^+ and to a lesser extent for N_2D^+. This is of particular interest because it is the first time that N_2D^+ depletion, which is often predicted by chemical models, finds confirmation in observational data. Further higher-resolution observations will help us investigate this point. The D/H ratios are peaked very close to the dust peak of L1544, and show different values, the deuteration of N_2H^+ being higher than that of HCO^+(26% and 3.5%, respectively). In an upcoming paper, we will use the results derived here to obtain spatially resolved information on the ionisation degree, a key parameter in the early stages of star formation.

Chapter 4

Magnetic properties of the protostellar core IRAS 15398-3359

The contents of this chapter were published in *Astronomy & Astrophysics* Journal.

4.1 Abstract

As shown in the Introduction (§1.5), magnetic fields (B) are expected to play an important role in the star formation process, for instance providing a source of non-thermal pressure against the gravitational pull, and this point has been broadly investigated from the theoretical point of view. In particular at the core scales ($\approx 0.1 - 1$ pc), the theory of spherical cores in uniform fields predicts the formation of a flattened structure because the collapse happens preferentially along the field lines. Due to the coupling of matter and field lines, the latter can bend inwards as a result of the gravitational pull, exhibiting a characteristic hourglass shape. In low-mass star forming regions this feature has only been detected in 30% of young stellar objects in polarisation (9 sources out of 32; Hull & Zhang 2019), suggesting that this is not a universal picture. Furthermore, out of these 9 detections only 2 show a clear hourglass shape, namely IRAS 4A (Girart et al. 2006) and L1448 (Kwon et al. 2018).

IRAS 15398-3359 (hereafter IRAS15398) appears to be the ideal candidate for a magnetically-driven collapse. This is the only Class 0 object (see §1.1.3) found in the Lupus I molecular cloud, at a distance of 156 pc (Dzib et al. 2018). Lupus I represents the least evolved cloud belonging to the Lupus complex —which consists of four components—, because it has the highest rate of prestellar to protostellar cores (Rygl et al. 2013). It has been studied with optical polarimetry in band R, which traces the large-scale magnetic fields, by Franco & Alves (2015). Their data unveiled an ordered morphology of the B-field, which is oriented preferentially perpendicularly to the filamentary structure of the cloud (see Figure 4.1). IRAS15398 has a luminosity of 1.8 $L_{\odot}$ and an envelope mass of 1.2 $M_{\odot}$. Oya et al. (2014) and Yen et al. (2017) modelled the protostellar envelope rotation to derive the mass of the central object, which is subsolar $M_{*} < 0.1\,M_{\odot}$). In particular, Yen et al. (2017) performed high-resolution interferometric observations with ALMA,

and posed an upper limit of 30 AU on the size of the protoplanetary disc, which is not resolved. Nevertheless the presence of a central object is indicated, beside by the detection of its infrared emission, by the fact that it is powering a bipolar outflow detected in CO lines both with single dish and interferometric observations (Tachihara et al. 1996; Bjerkeli et al. 2016).

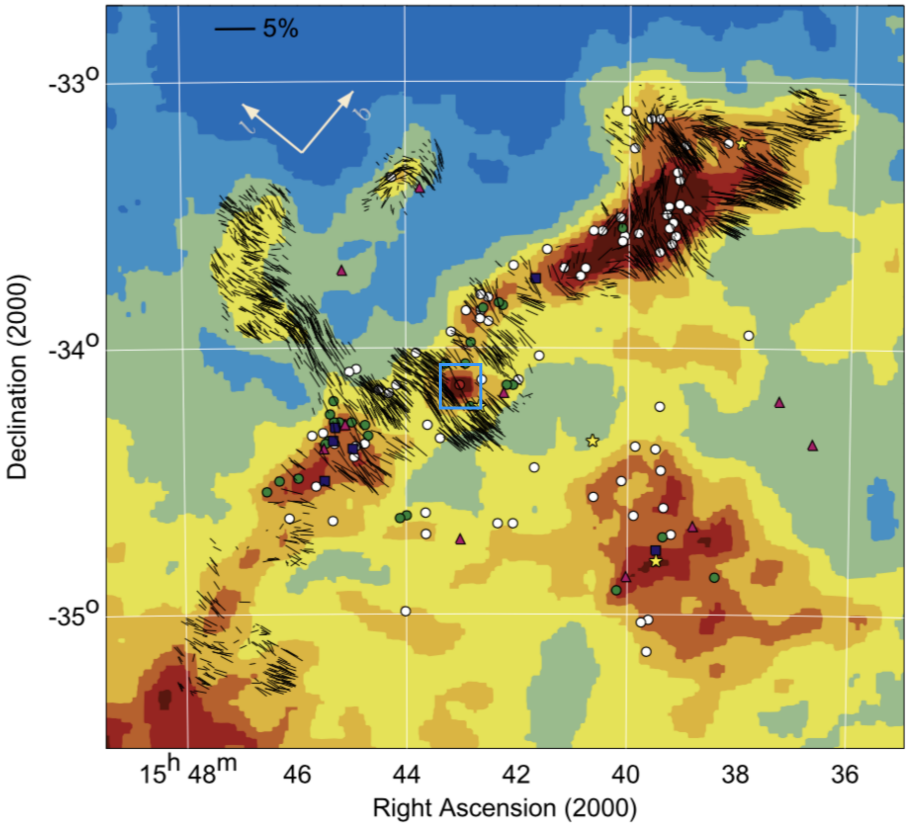

Figure 4.1: IRAS 100 μm map with overlaid the polarisation vectors in the R-band in Lupus I. The vector length is proportional to the polarisation fraction, accordingly to the scale-bar indicated in the upper left corner. The symbols indicate different core types, from Rygl et al. (2013): starless cores (white circles), prestellar cores (green circles), Class 0 (red circles), Class I (triangles), Class II (squares), and Class III (stars). The position of IRAS15398 is highlighted with a cyan box. Figure from Franco & Alves (2015)

The optical data are sensitive only to low visual extinction, as shown in §1.5.1. In order to investigate the magnetic field properties in the denser part of the core ($A_V \gtrsim 10$ mag), we have performed polarimetric observations at terahertz frequency using the Stratospheric Observatory for Infrared Spectroscopy (SOFIA) telescope. The data are presented in §4.2 and §4.3. The data analysis, which involves also the estimation of the field strength and of the mass-to-flux ratio, is reported in §4.4. In §4.5 we draw the conclusions of this work, whilst in §4.6 we describe possible future developing of this project.

4.2 Observations

4.2.1 Polarimetric data

The polarimetry observations were carried out with the SOFIA telescope, using the High-resolution Airborne Wideband Camera Plus (HAWC+) instrument (Harper et al. 2018) in summer 2018. We used the band E, which has a nominal wavelength of 214 μm (1.4 THz). At this frequency, the SOFIA beam full width half maximum FWHM $\approx$ 19″ (corresponding to $\approx$ 0.01 pc at the distance of the source) and the field of view is 5.0′ × 6.3′. The data were processed with the standard pipeline (HAWC DRP, version 1.3.0), and we used the flux-calibrated Level 4 data products (already flux calibrated and mosaicked). The total integration time was $\approx$ 1h15min, and the sensitivity achieved in the Stokes I is 65 mJy/beam. In order to increase the signal-to-noise ratio (S/N) of the data and to have significant detections over a large percentage of the source, we smoothed the Stokes parameter I, Q, and U to 42″ resolution ($\approx$ 0.03 pc), before producing maps of polarisation intensity and position angle (see §4.3). The final mean sensitivity is rms = 48 mJy/beam (Stokes I), 77 mJy/beam (Stokes Q), and 77 mJy/beam (Stokes U). Since we found no indication of spatially correlated noise, the smoothing technique as a tool to increase S/N is justified.

4.2.2 H_2 column density maps

To obtain the gas column density $N_{\rm mol}(H_2)$ and the visual extinction $A_{\rm V}$ maps of the source, we used the archive data of the Gould Belt Survey, performed with the *Herschel* space telescope (André et al. 2010). These data provide directly the H_2 column density map of Lupus I, obtained with a spectral fitting of the dust emission at five wavelengths (70, 160, 250, 350, and 500μm). This map has a resolution of $\approx$ 38″, which allows for a fair comparison with the SOFIA smoothed data. We derived the visual extinction map using the standard relation $A_{\rm V}/{\rm mag} = 1.06 \times 10^{-21} \times N_{\rm mol}(H_2)/{\rm cm}^{-2}$ (Bohlin et al. 1978).

4.3 Results

Appendix C.1 reports the maps of the three Stokes parameters I, Q, and U. From these, we derive the polarised flux ($I_{\rm P}$), polarised fraction (P), and polarisation angle (PA), following the standard equations (see §1.5.1 for more details):

$$I_{\rm P} = \sqrt{Q^2 + U^2 - \sigma^2_{I_{\rm P}}}\,, \tag{4.1}$$

$$P = \frac{I_{\rm P}}{I}\,, \tag{4.2}$$

$$PA = \frac{1}{2}\tan^{-1}\left(\frac{U}{Q}\right)\,. \tag{4.3}$$

In order to remove the bias of the polarised intensity, in Eq. 4.1 we removed the contribution of the flux uncertainty ($\sigma_{I_{\rm P}}$). This procedure is necessary since $I_{\rm P}$ is biased to positive values,

while the Stokes U and Q parameters can be positive or negative (Vaillancourt 2006). To avoid oversampling, after smoothing the data we re-gridded the maps to a pixel size of 9.1″ (≈ 4 pixels per smoothed beam). Table 4.1 summarises the peak and mean values for the derived parameters. Figure 4.2 shows the Stokes I emission, with polarisation vectors already rotated by 90° to indicate the plane-of-sky component of the magnetic field. We masked data points with a S/N in a polarisation fraction lower than 3.

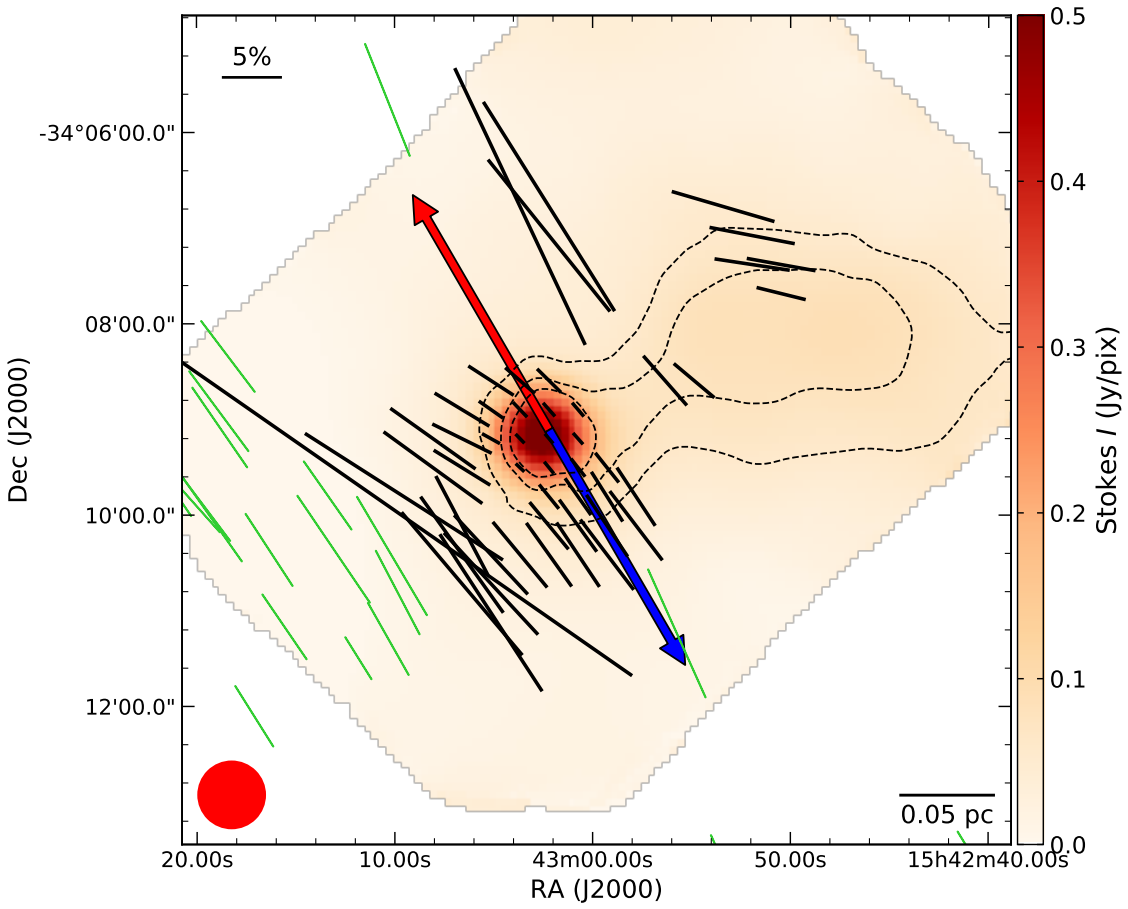

Figure 4.2: Colour-scale map of the Stokes I flux observed by SOFIA. The dashed contours represent $N_{\rm mol}(H_2)$ column density as derived from *Herschel* data (levels = [1.0, 1.5, 2.0] × 10^{22} cm^{-2}). The black vectors show the polarisation angles, tilted by 90° to trace the magnetic field direction, and their length is proportional to the polarisation fraction (scale bar in the top left corner). To show statistically independent data, we plot only two vectors per smoothed beam. The smoothed beam size is shown in the bottom left corner. In green, we show the polarisation vectors from optical observations from Franco & Alves (2015). The red and blue arrows indicate the direction of the outflow.

Table 4.1: Peak and mean values of the polarised flux, polarised fraction, and position angle.

Parameter	Peak	Mean[a]
$I_{\rm P}$ (Jy/beam)	0.53±0.07	0.28±0.07
P (%)	28±8	6.6±1.8
PA (°)	-	45±7

[a] The mean values are computed over positions satisfying $\sigma_P/P > 3.0$ and $P < 30\%$.

4.4 Analysis and discussion

4.4.1 Magnetic field direction

Figure 4.2 shows the magnetic field direction traced by the SOFIA data. The field at sub-parsec scale is aligned with the large (parsec) scale field observed in starlight optical polarisation. The histograms of the two position angle distributions are presented in Figure 4.3. The mean values of the two distributions differ by $\approx 5°$, which is less than the mean uncertainty on the SOFIA position angles ($\langle\epsilon_{PA}\rangle = 7°$). Since the two datasets are sensitive to two different regimes, i.e. the optical data trace large cloud scale, whilst the SOFIA data are sensitive to the core scales, this means that the uniform magnetic field of the cloud has been inherited by the core and that the gravitational collapse was magnetically driven.

In Fig. 4.2 we also show that the outflow direction ($PA = 35°$, Bjerkeli et al. 2016) lies almost parallel to the magnetic field, which has a mean direction of $\langle PA\rangle = (45 \pm 7)°$. This behaviour is consistent with the prediction of the theory of the magnetically driven collapse, according to which a strong magnetic field can efficiently remove the excess of angular momentum from rotating cores, thus aligning the rotation axis with the magnetic axis (see e.g. Li et al. 2014, and references therein).

Another prediction of the theory is the hourglass shape of the magnetic field lines. In IRAS15398 this is not clearly visible, even though we detect a bending of the field lines which may hint to a partial hourglass shape. On the side of the core facing south-east, the field lines pinch inwards towards the centre of the object. The mean position angle north-east of the source is $PA = (55 \pm 7)°$, whilst $PA = (36 \pm 7)°$ is derived south-west of the source. The change in angle is thus 19°, significantly larger than the uncertainty. We do not detect the north-west side of the hourglass, possibly for two reasons. First of all, on that side we lack the sensitivity to detect a bend in the field lines, since the polarised flux is less prominent. This can be due to the presence of the filamentary structure that extends towards the west. This filament provides more shielding from the external radiation field with respect to the other side of the core, which is more exposed. Since this radiation is responsible for the grain alignment, according to the RAT theory, grains are less efficiently aligned on the north-west side of IRAS15398, which results in a lower polarised flux. Moreover, the presence of the filament can affect the detected morphology of the field lines in a second way. The presence of the extended dust emission in the west direction

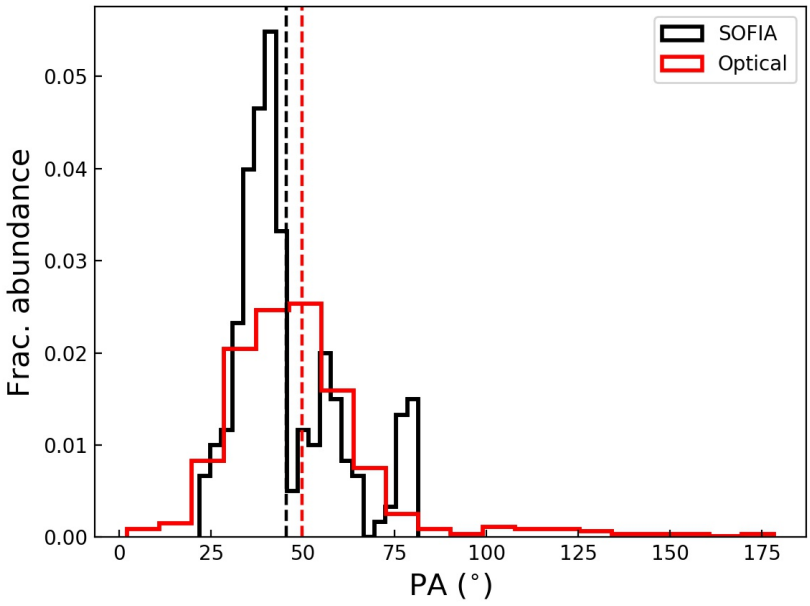

Figure 4.3: Fractional abundance distribution of the magnetic field direction angles as traced by the THz data (black) and optical data (red).The distributions mean values, shown with vertical dashed lines, are 45°(SOFIA) and 50°(optical). The SOFIA data present a three peaked distribution, with peaks being at ≈ 40°, ≈ 55°, and ≈ 77°. These correspond to vectors coming from the two halves of the presumed hourglass shape and filament, respectively.

could have played a role in disturbing the spherical collapse of the core. This scenario is supported by the few detections along the filament, which reveal a significant twist in the B direction ($PA \approx 69°$). This suggests that in this portion of the source the magnetic field morphology has been perturbed, likely by accretion motions towards the central object.

4.4.2 Depolarisation at high column densities

Figure 4.2 shows that the emission is less polarised as the column density gets higher, towards the centre of the core. This effect has been widely observed in the literature (Matthews et al. 2009; Alves et al. 2014; Jones et al. 2015, 2016). In Figure 4.4 we show the scatter plot of the polarisation fraction as a function of the visual extinction. We also report the polarisation efficiency for the optical data, which is defined as the polarised fraction normalised by the visual extinction (see the Introduction in Santos et al. 2017). In this way, we correctly take into account the attenuation of the background stellar light. We use the data from Franco & Alves (2015), limiting ourselves to the galactic latitude range $16.2° < b < 17.0°$ (the "Middle" region in Franco & Alves 2015).

There are a number of possible explanations for the depolarisation at high column densities. In general, if the alignment is dominated by radiative torque due to the interstellar radiation

field, at higher visual extinction less and less radiation penetrates the core and dust grains are less aligned. Moreover, the alignment efficiency is highly sensitive to the dust grain population (Bethell et al. 2007; Pelkonen et al. 2009; Brauer et al. 2016). In particular, Brauer et al. (2016) showed that polarisation can decrease by up to 10% when grains are submillimetre or millimetre in size. Grain growth is expected in Class 0 objects, as shown by Jørgensen et al. (2007); Kwon et al. (2009); Chiang et al. (2012). Finally, geometrical smearing is possible. Close to the central object, a highly perturbed magnetic field is likely to be present because of the dominant effect of gravity at the small scales which are unresolved by the SOFIA data. Higher angular resolution observations are needed to disentangle these scenarios.

We fitted a linear relation in the log-log space for the polarisation efficiency versus visual extinction in each dataset, deriving the slope of the relation $P_{\rm eff} \propto A_{\rm V}^{-\gamma}$ (Figure 4.4). For the optical data, tracing the cloud scales, we find $\gamma = 0.57 \pm 0.07$, which is consistent with modelling of RAT alignment in molecular clouds (see e.g. Whittet et al. 2008, who also report the measurements in Taurus and Ophiucus clouds). For the FIR data, we find a steeper slope ($\gamma = 1.21 \pm 0.12$), implying a strong depolarisation for $10 \lesssim A_{\rm V}\,({\rm mag}) \lesssim 50$. Values of $\gamma \approx 1$ are often found in literature for prestellar and young Class 0 objects (Alves et al. 2014; Jones et al. 2015, 2016). The different slopes exhibited by the optical and FIR data suggest that the two datasets are probing two different regimes in the grain alignment. This in turn can be related to two different grain populations, in which the larger grains in the core are less efficiently aligned to the *B*-field than

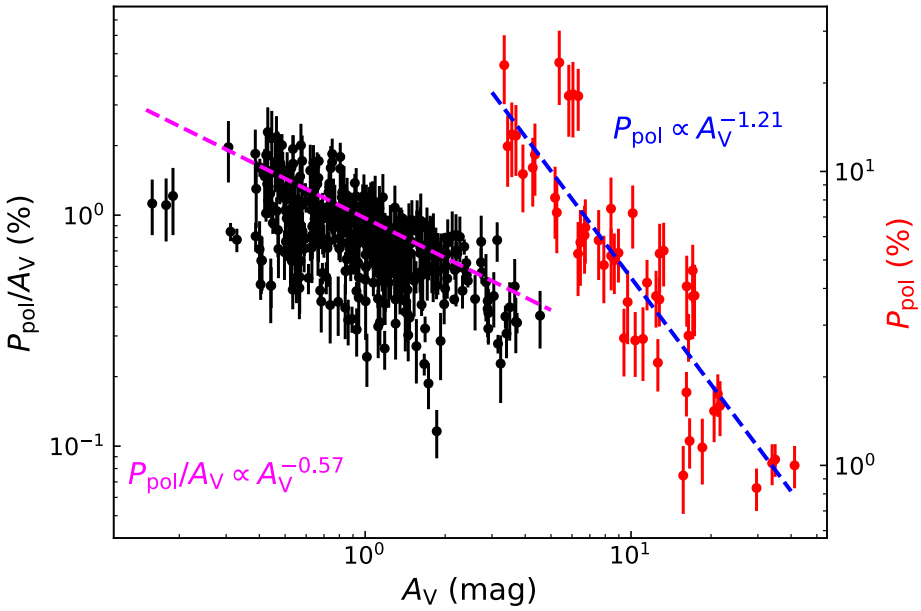

Figure 4.4: Scatter plots of the polarisation efficiency as a function of the visual extinction in magnitudes for the optical data (in black) and for the FIR data (in red, only one point every other is shown), in logarithmic scale. The best fit to each dataset, as described in the main text, is shown with the pink and blue dashed curve, respectively. The best-fit equations are also shown in the bottom left and top right corners.

those in the cloud (see e.g. Sec. 3 in Andersson et al. 2015), or it can be due to a less efficient RAT, in which the grains traced by SOFIA are more shielded from the interstellar radiation field with respect to those traced by the optical data. Another possibility is a more entangled magnetic field lines, as mentioned before. According to recent results, a slope of $\gamma \approx 1$ can be a consequence of biases introduced by the S/N cut (Wang et al. 2019). To exclude this possibility, we fitted the linear relation lowering the threshold to S/N > 0.5, obtaining $\gamma = 1.26 \pm 0.09$, in agreement the previous result, thus suggesting that no significant bias is introduced by the data selection.

4.4.3 Angular dispersion function and field strength

The angular dispersion function (ADF) method, introduced by Hildebrand et al. (2009) and Houde et al. (2009), involves the computation of the autocorrelation function of the position angles. It allows us to derive quantitative information on the *B*-field without depending on an assumption concerning the field morphology. The method assumes that the magnetic field is composed by an ordered component (B_0), slowly changing spatially, and a turbulent or random component (B_t), which is characterised by a correlation length scale δ. We now consider the autocorrelation function of the position angles $\Delta\Phi$, i.e. the difference in angle of every pair of vectors separated by the distance l as follows:

$$\langle \Delta\Phi^2(l) \rangle = \frac{1}{N} \sum_{i=1}^{N} [\Phi(x) - \Phi(x+l)]^2 \ . \tag{4.4}$$

Hildebrand et al. (2009) showed that on scales d such that $\delta < d << \Delta$, where Δ is the physical scale of the analysed source, the structure function has the form

$$\langle \Delta\Phi^2(l) \rangle = b^2 + a^2 l^2 + \sigma_M^2 \, , \tag{4.5}$$

where σ_M is the uncertainty on the measurements. The parameter a is linked to the large-scale variations of the *B*-field, while b is related to the ratio of the turbulent and uniform magnetic field components via $B_t/B_0 = b/\sqrt{2-b^2}$.

Houde et al. (2009) further expanded the analysis, in particular including the effects introduced by the telescope beam size. In case of a Gaussian beam with standard deviation $W_{\rm beam}$, they found the following expression:

$$\langle \Delta\Phi^2(l) \rangle = 2\sqrt{2\pi} \left(\frac{B_t}{B_0} \right)^2 \frac{\delta^3}{(\delta^2 + 2W_{\rm beam}^2)\Delta'} \times \left[1 - \exp\left(-\frac{l^2}{2(\delta^2 + 2W_{\rm beam}^2)} \right) \right] + m^2 l^2, \tag{4.6}$$

where Δ' is the cloud effective thickness and m is a parameter related to the large-scale structure of the magnetic field, which does not involve turbulence.

In order to fit Eq. 4.6 to derive the B_t/B_0 parameter, we computed $\Delta\Phi^2$ for all the available pairs of points with $0'' < l < 180''$, divided in 9 bins $20''$ wide. The choice of binning is determined by the angular resolution of the observations, as we did not want to oversample the beam size, and by the map size; each bin should contain a fairly constant number of points. We

computed the uncertainty σ_M in each bin propagating the uncertainties on the position angles, assumed to be uncorrelated. They are usually within 3-5%. The FWHM of SOFIA smoothed beam (42″) corresponds to a standard deviation of $W_{beam} = 18'' = 13$ mpc.

Because of the limited number of data points available for the fit, we fixed the turbulence correlation scale on $\delta = 20$ mpc. This value is in good agreement with previous estimation of this quantity in other star forming regions: for instance Houde et al. (2009) found $\delta = 16$ mpc in OMC-1, Frau et al. (2014) derived $\delta = 13 - 33$ mpc in the high-mass star forming region NGC 7538, and Coudé et al. (2019) reported $\delta = 7$ mpc in Barnard 1. Furthermore, we assumed the cloud thickness Δ' to be equal to the source effective radius (r_{eff}), defined as the radius of a circular region of identical surface area. To compute the latter, we considered only positions with Stokes $I > 0.05$ Jy/pix. This threshold roughly corresponds to the lowest contour in $N_{mol}(H_2)$ in Figure 4.2 (1×10^{22} cm^{-2}), and it is the first closed contour that comprises both the central core and filamentary structure towards west. We obtained $r_{eff} = 0.1$ pc, a result which is also in agreement with the typical size of cores and filamentary structures in molecular clouds (see e.g. Arzoumanian et al. 2011; André et al. 2014). In §4.4.4 we explored the effects of these assumptions on the results.

In Figure 4.5 we show the resulting data points and their uncertainties. We also show the best-fit solution found for Eq. 4.6. The obtained best-fit parameters are reported in Table 4.2. We emphasise that while figures and tables are expressed in degree and arcsecond units, the actual fit is performed in radiant and parsec units.

To estimate the strength of the magnetic field, we applied a modified version of the method proposed by Chandrasekhar & Fermi (1953) (CF). The CF approach assumes the equipartition of kinetic and perturbed magnetic field energy to link the magnetic field strength on the plane of sky (B_{pos}) to the velocity dispersion of the gas (σ_V) and to the dispersion of the polarisation angle ($\delta\phi$), which in turn corresponds to the turbulent ratio ($\delta\phi \equiv B_t/B_0$). Further development of the theory led to the equation

$$B_{pos} = \sqrt{4\pi\mu m_H n(H_2)}\frac{\sigma_V}{\delta\phi} , \tag{4.7}$$

which is valid in the assumption of a small polarisation angle ($\delta\phi < 25°$; Ostriker et al. 2001; Padoan et al. 2001; Crutcher et al. 2004). In Eq. 4.7, μ is the gas mean molecular weight per hydrogen molecule, assumed to be $\mu = 2.8$ (Kauffmann et al. 2008), m_H the hydrogen mass ($m_H = 1.67\,10^{-24}$g), and $n(H_2)$ is the gas volume density.

To compute B_{pos}, we needed to determine the quantities $n(H_2)$ and σ_V. For the gas volume density, we consider the H_2 column density map, integrated over the region used to derive the effective radius, obtaining the total number of H_2 molecules H_{tot} in the considered region. Assuming a uniform distribution of the gas, we could thus derive

$$n(H_2) = \frac{3}{4\pi}\frac{H_{tot}}{r_{eff}^3} = 2.6 \times 10^4\,\mathrm{cm}^{-3} . \tag{4.8}$$

For the gas velocity dispersion, we used the results of Benedettini et al. (2012), who observed several molecular tracers in Lupus I with the MOPRA telescope, which at 3 mm has a beam

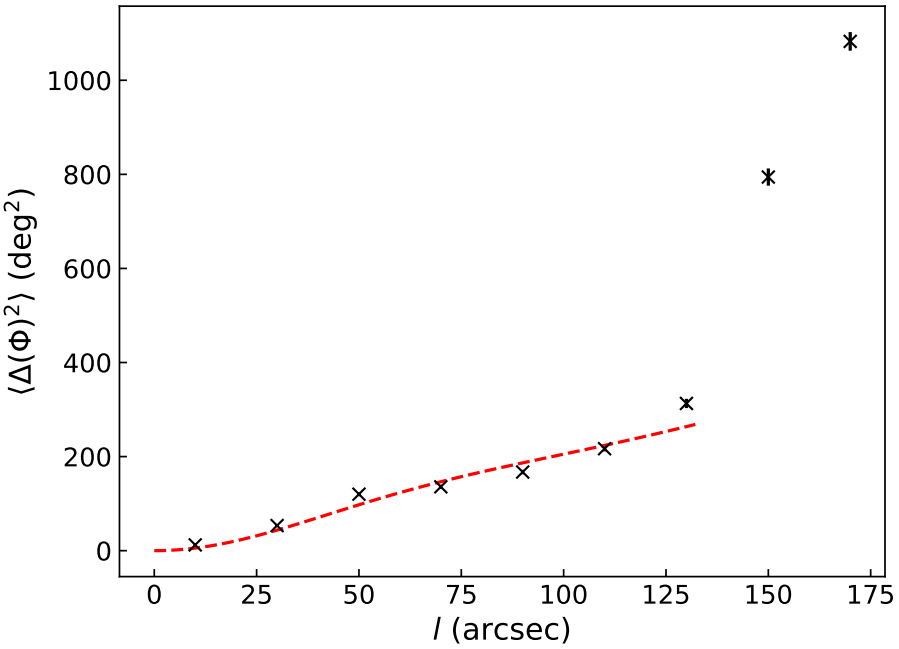

Figure 4.5: Angular dispersion function of the SOFIA data with respect to the distance parameter l, computed as described in §4.4.3. The measurement uncertainties $\sigma_{\rm M}$ are shown as error bars, and for low values of l they are too small to be seen. The best fit to the data points, following Eq. 4.6, is shown with a dashed curve.

size similar to the one of our data. At the position of IRAS15398, these authors reported FWHM values in the range $0.31-0.72\,{\rm km\,s^{-1}}$. We adopted the mean of their results (excluding the CS (2-1) line, which is most likely optically thick), FWHM $= 0.41\,{\rm km\,s^{-1}}$, corresponding to a velocity dispersion $\sigma_{\rm V} = 0.17\,{\rm km\,s^{-1}}$. Inserting these values in Eq. 4.7, we obtained $B_{\rm pos} = 78\,\mu$G. Owing to the strong assumptions of the method, such as the core uniform density, we expected this value to be accurate within a factor of two. Furthermore, we want to highlight that it is intrinsically a lower limit, since it neglects the line-of-sight component of the field.

As shown in §1.5, a fundamental parameter is the mass-to-flux ratio (M/Φ), which is determined by the ratio of the gravitational to magnetic energy. This ratio provides the dynamical state of the core (equilibrium or collapse). In particular, it is interesting to compute its observed value with respect to the critical value, which in observational units can be defined as (Crutcher et al. 2004):

$$R = (M/\Phi)_{\rm obs}/(M/\Phi)_{\rm crit} = 7.6\times10^{-21}\left(\frac{N_{\rm mol}({\rm H_2})}{\rm cm^{-2}}\right)\left(\frac{B}{\mu{\rm G}}\right)^{-1}\,, \qquad 4.9$$

where $N_{\rm mol}({\rm H_2})$ is the mean column density of the source, computed in the region over which B is measured. Focussing on the same region used to derive $n_{\rm H_2}$, we obtained $N_{\rm mol}({\rm H_2}) = 9.8\times10^{21}\,{\rm cm^{-2}}$, and therefore $R = 0.95$. Our derived value of R suggests that the core is in transitional state between being subcritical and supercritical.

Our analysis of the mass-to-flux ratio considers only the gas mass of the source, and neglects

Table 4.2: Summary of the main parameters concerning the magnetic field, derived as described in §4.4.3.

B_t/B_0	m (deg^2/arcsec^2)	B_{pos} (μG)	R
0.267 ± 0.007	170 ± 50	78	0.95

the protostellar mass. However, the total mass within the contour Stokes $I > 0.05$ Jy/pix is $\approx 6\,M_\odot$, which is significantly higher than the the protostellar mass (the upper limit is $M_* < 0.1 M_\odot$, Yen et al. 2017). This approximation therefore causes an error of less than 2%, i.e. well below our uncertainties.

4.4.4 Influence of the assumed parameters

The analysis described above depends on the assumption of several key parameters. We explore in this section how the results are affected by changing the assumed values. The first assumption regards the turbulence correlation scale, δ. The literature results seem to suggest that δ is lower for low-mass star forming regions with respect to high-mass ones: both Liu et al. (2019) and Coudé et al. (2019) found $\delta < 10$ mpc in low-mass cores. We therefore tested other three values (5, 10, 15 mpc), obtaining $B_0 = 16, 40, 62\,\mu$G, respectively. The magnetic field strength hence increases with increasing δ. The turbulent-to-uniform component ratio is lower than one in all cases but the extreme one ($\delta = 5$ mpc), for which is marginally higher than one ($B_t/B_0 = 1.3$). On the other hand, the mass-to-flux ratio for these values is $R > 1.0$, pushing the state of the core more towards the supercritical regime.

A second assumption that is made regards the cloud effective thickness (Δ'), which may not necessary correspond to the real thickness Δ. In particular, according to Houde et al. (2009), $\Delta' \leq \Delta$, where the equality holds only if the large-scale magnetic field is completely uniform. We therefore repeated the analysis using $\Delta' = r_{\rm eff}/2$. The results vary of less than 30%, which is below our uncertainties.

The magnetic field strength can also be calculated directly with the modified Chandrasekhar-Fermi method (Eq. 4.7), computing directly the standard deviation of the position angles ($\delta\phi$), hence avoiding the assumptions made in the ADF method. In this case, Eq. 4.7 must be corrected for a numerical factor (Q) to take into account that its original version tends to overestimate the magnetic field (Ostriker et al. 2001; Crutcher et al. 2004). A usually adopted value is $Q = 0.5$. From the SOFIA data, we measured $\delta\phi_{\rm obs} = 14°$. This value is however biased upward by the observational uncertainties on the position angles (ϵ_{PA}), and it must be corrected using $\delta\phi^2 = \delta\phi^2_{\rm obs} - \epsilon^2_{PA} = (12°)^2$ (Crutcher et al. 2004). Hence, introducing $\delta\phi = 12°$in Eq. 4.7, we obtained $B_0 = 47, \mu$G, which is in well agreement with the result of the full ADF analysis, given the uncertainties. We conclude that the results are robust with respect to our assumptions.

4.5 Conclusions

We have performed polarimetric observations of the dust thermal emission at 1.4 THz in the class 0 protostar IRAS15398. Our data unveil a very ordered magnetic field. The direction of the magnetic field is consistent within uncertainties with that found by Franco & Alves (2015) using optical data, which trace large cloud scales. This suggests that during its evolution the core preserved the B-field morphology inherited from the parental cloud, and experienced a magnetically driven collapse.

The magnetic field lines on the south-east side of the core pinch inwards, hinting at the hourglass shape predicted by the theoretical models. However, we lack the sensitivity to clearly identify the hourglass shape. The lack of such a pinching on the other side of the core may be linked to the presence of an extended structure linked to the central core. The polarisation vectors detected in this filament show a significantly different direction of the magnetic field, perhaps hinting that material is being dragged towards the central object and that the infalling gas is perturbing the magnetic field morphology. Further line observations, which allow us to infer the velocity field in the source, will help us enlighten this point.

Using the modified CF method we estimate the magnetic field strength on the plane of sky to be $B_{\rm pos} = 78\,\mu$G, accurate within a factor of two. This value is in the lower end of the range found on similar spatial scales performed in star forming regions for example with the JCMT telescope (see e.g. Crutcher et al. 2004; Kwon et al. 2018; Soam et al. 2018; Liu et al. 2019), where B-strengths of $80 - 5000\,\mu$G have been reported.

The mass-to-flux ratio that we derive ($R = 0.95$) is close to the transcritical regime ($R = 1$). Usually cores are found to be supercritical (see e.g. Troland & Crutcher 2008), in contrast with molecular clouds which are often subcritical: for instance, Franco & Alves (2015) found $R = 0.027 - 0.057$ in Lupus I. IRAS15398 hosts a protostellar object, which indicates that indeed gravitational collapse has happened and that, on some scales, the source must be supercritical. Our observations are likely missing the angular resolution to probe those scales, and therefore we are seeing an intermediate state due to the subscritical surrounding medium. On the other hand, the uniform-to-turbulent ratio is smaller than one ($B_{\rm t}/B_0 = 0.267$), suggesting a strongly magnetised core. This scenario is also supported by the lack of a large Keplerian disc in the source; Yen et al. (2017) found an upper limit to the disc size of 30 AU. Magnetic braking is in fact an efficient way to remove angular momentum from the infalling and rotating material and prevent the formation of large discs (Li et al. 2014). Overall, our data suggest that IRAS15398 evolved in a highly magnetised environment, and that the ordered magnetic field was preserved from cloud scales down to core scales.

4.6 Future perspectives

As described in the Introduction (§1.5), magnetic fields are expected to play an important role during the star formation process, together with turbulence. However, the precise role of these two forces in the different phases of the star formation process and their mutual interaction are still under great debate. When gas dynamics prevails, it can compress the B-field lines; for

instance, shocks can shape and bend the field lines parallel to their front (Soler et al. 2018). On the other hand, when the magnetic energy is larger then the kinetic one, the field can effectively guide the gas flow, forming for instance filamentary structures. This scenario is supported by both simulations (Nakamura & Li 2008) and observations (Santos et al. 2016).

In this context molecular lines represent a crucial tool to investigate the relation between the kinematics and the magnetic fields. In fact, their analysis yields information about both the velocity field and dispersion, which is a proxy for assessing the turbulence level in the source. We therefore obtained line spectroscopic data to perform this study in IRAS15398, in order to investigate the relation between the kinematic structure and the magnetic field morphology in a protostellar core, which is known to have evolved in an highly magnetised environment. We targeted the rotational transitions of two abundant molecules: $C^{18}O$ (2-1) and DCO^+ (3-2). These lines are expected to be optically thin and they do not present crowded hyperfine structures. Both these characteristics are important to correctly map the centroid velocity and the velocity dispersion. Furthermore, they present different critical densities[1]: $n_{cr}[C^{18}O(2-1)] \approx$ a few$\times 10^4$ cm^{-3} and $n_{cr}[DCO^+(3-2)] \approx 10^6$ cm^{-3}. Therefore, $C^{18}O$ traces the more extended and tenuous gas in the filamentary structure, while DCO^+ traces preferentially the denser component closer to the central protostar, allowing us to fully reconstruct IRAS15398 kinematics.

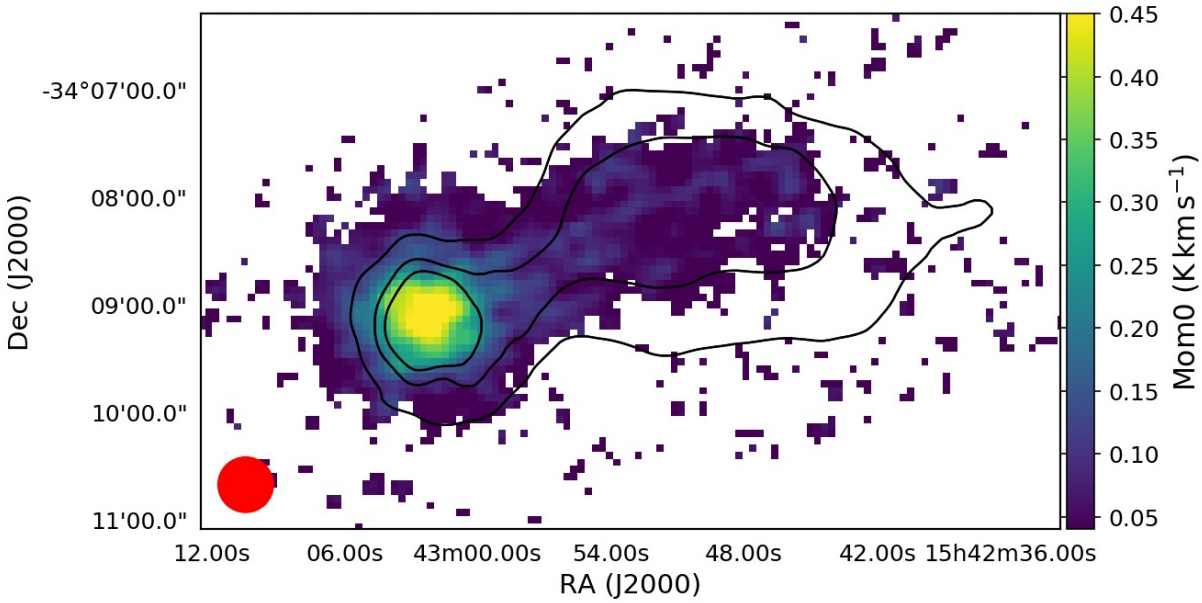

Figure 4.6: Integrated intensity of DCO^+ (3-2) towards IRAS15398. The beam size is shown in the bottom-left corner. The contours show H_2 column density (levels: $[1.0, 1.5, 2.0]\times 10^{22}$ cm^{-2}).

The observations were performed during autumn 2019 with the Atacama Pathfinder EXperiment (APEX) single-dish antenna. The data analysis is still ongoing, in particular for the $C^{18}O$

[1]Based on our on calculation from CDMS data, `https://cdms.astro.uni-koeln.de/classic/catalog`.

(2-1) line which presents a complex kinematic structure with multiple components along the line-of-sight. We present here the preliminary maps obtained for the DCO^+ (3-2) transition, which instead can be fitted with a simple Gaussian model towards all the positions where it is detected. Figure 4.6 shows the integrated intensity of the line. Here and in the following images we have performed a simple S/N cut, masking those pixels where $T_{\rm MB}^{\rm peak}/rms < 3.0$. As expected, DCO^+ is a high-density tracer, and therefore its strongest emission comes from the protostellar envelope. However, we detect it also in the central part of the filamentary structure extending to north-west.

In order to recover the kinematic properties, we have fitted a Gaussian model to the observed data. At each position, its centroid and standard deviation represent the local velocity ($V_{\rm lsr}$) and velocity dispersion ($\sigma_{\rm V}$) of the gas. Figure 4.7 shows the standard-of-rest velocity. The filament appears to be a monolithic structure, with very small dispersion around the mean value ($\langle V_{\rm lsr}\rangle = 5.1\,{\rm km\,s^{-1}}$). On the other and, a moderate velocity gradient is observed towards the central core, in the east-west direction. We can speculate that this is due to the rotation of the core. In this scenario, the rotation axis would lay approximately in the north-south direction, close to the direction of the detected bipolar outflows. This agreement could support the hypothesis of rotation.

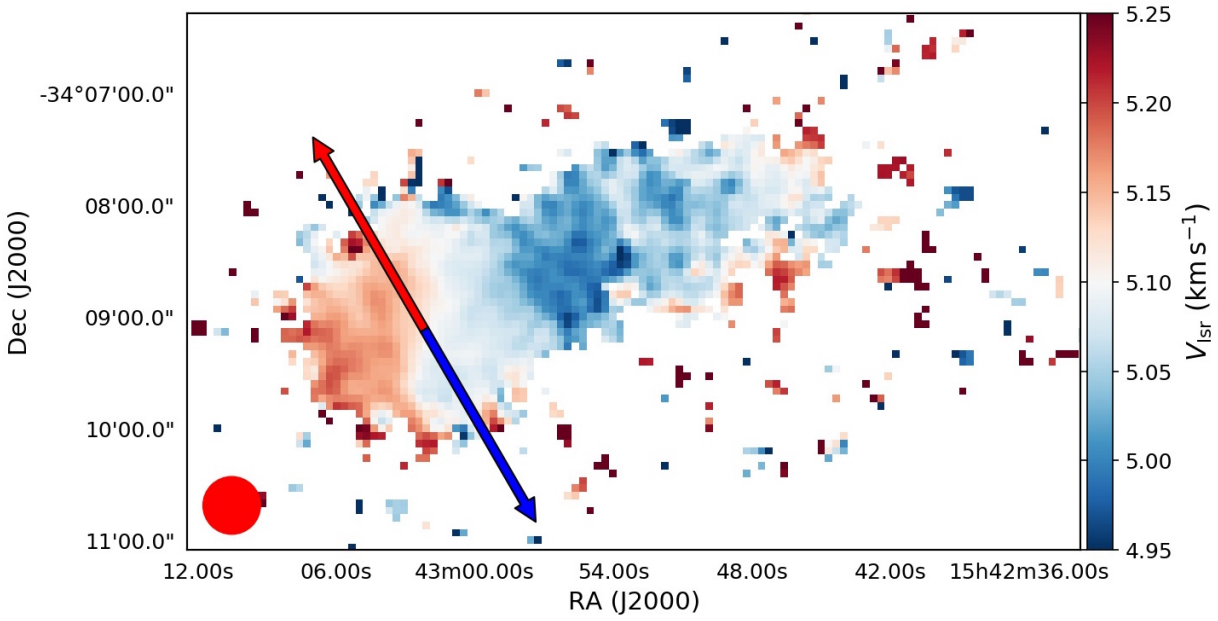

Figure 4.7: The $V_{\rm lsr}$ map obtained fitting the observed DCO^+ data. The beam size is shown in the bottom-left corner. The blue/red arrows represent the bipolar outflow. Its direction lays close to the one of the rotation axis of the core, in the hypothesis that this is the cause of the observed velocity gradient.

The velocity dispersion of the gas is shown in Figure 4.8. The lines are narrow, but become significantly broader towards the central object. In the filament, in fact, the mean value is $\langle\sigma_{\rm V}\rangle = 0.12\,{\rm km\,s^{-1}}$, while for positions where $N_{\rm mol}(H_2) > 2\times10^{22}\,{\rm cm^{-2}}$ we derive $\langle\sigma_{\rm V}\rangle = 0.16\,{\rm km\,s^{-1}}$. This enhancement in the linewidth is most likely linked to the protostellar activity, which is

heating the surrounding material and injecting turbulence in it. As a result, the gas velocity dispersion increases.

The future analysis of these data, combined with the information coming from the $C^{18}O$ line, will allow us to investigate the possible connections within the source kinematics and the magnetic field morphology.

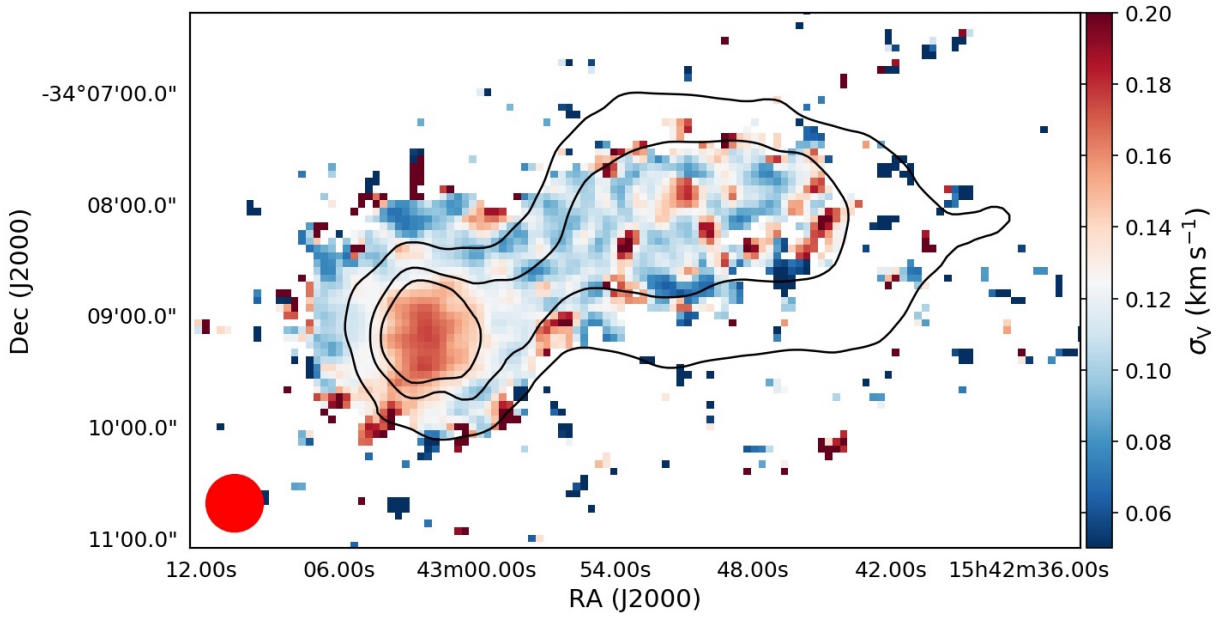

Figure 4.8: The gas velocity dispersion in IRAS15398 traced using the DCO^+ (3-2) line. Contours are the same as in Figure 4.6. The APEX beam size is shown in the bottom-left corner.

Chapter 5

Summary and future perspectives

In this work, we have first focused on fractionation processes, which are known to be highly indicative of the evolutionary stage of prestellar cores. In particular, we have investigated the nitrogen isotopic ratio ($^{14}N/^{15}N$) in a small sample of prestellar cores (Chapter 2). Nitrogen fractionation is of particular interest, since it is believed it can be used to trace the origins of the different material in the Solar System. To reach this ambitious goal, however, one needs a complete understanding of nitrogen chemistry throughout the whole star forming process. Our results show high isotopic ratios in diazenylium ($^{14}N/^{15}N = 580 - 1000$), which cannot be explained by the current chemical models that treat N-isotopologues.

In Chapter 3, we have studied a particular source, L1544, which represents one of the most studied prestellar cores, with the aim of investigating its deuteration level. We have made use of new, high-sensitivity data covering several transitions of some of the most abundant ions in the ISM, together with their isotopologues: N_2H^+, N_2D^+, $HC^{18}O^+$, DCO^+. We have carefully modelled the collected spectra at the core's centre using a fully non-LTE analysis, and used the information coming from it to obtain reliable maps of the column density of the targeted species. One of the main results of this project is that the non-LTE analysis is indeed required, since the different transitions of each molecule exhibit variations in the excitation temperature of more than $1 - 2$ K. Furthermore, the chemical model that provides the best fit to the observed data predicts the depletion of all the molecular tracers at the core's centre, N_2D^+ included. This has been suggested only once in the literature, by Pagani et al. (2007). However, those authors had access to poorer quality data, translating in a low signal-to-noise ratio in their conclusions. Instead, with our high-sensitivity data we are able to infer a drop in the N_2D^+ abundance of one order of magnitude in the central 5000 AU.

With our analysis, we have derived peak deuteration levels of 26% for N_2H^+ and 3.5% in HCO^+. The higher D/H ratio of diazenylium can be explained by its chemical features. N_2H^+ is a late type molecule and it is not affected by freeze-out as strongly as C- or O-bearing species. As a results, it is more abundant in high-density and low-temperature environments, where deuteration processes are greatly enhanced.

Chapter 4 was focused on the study of another key ingredient of the ISM, which can play an important role for the cores' stability: magnetic fields. These cannot be observed directly. However, we have made use of the alignment of dust grains in the presence of an external *B*-field,

which makes their thermal emission polarised. We have therefore performed polarimetry observations at 1.4 THz using the airborne facility SOFIA, which allows to avoid the vast majority of the atmospheric absorption at these frequencies. The targeted source is a young protostellar core, IRAS 15398-3359. Our data unveiled an ordered magnetic field morphology. However, the field lines pinch inwards towards the central object, giving rise to the characteristic hour-glass shape which is predicted by models of magnetically-driven collapse.

5.1 Future perspectives

Specific comments on the immediate development of the projects here discussed have been made in dedicated sections (see for instance §2.7 and §4.6). Here, we want to illustrate a more general outlook for the astrophysical problems addressed in this thesis.

The conclusions of Chapter 2 made clear that we are still far from having a comprehensive understanding of nitrogen chemistry. This is particularly true for N_2H^+, which is of key interest since it should trace the main reservoir of nitrogen in molecular clouds: N_2. To this aim, more efforts are needed from both the modelling and the observational point of view. In particular, observations should provide more useful constrains about the N isotopic ratio during the distinct phases of low-mass star formation. In §2.7, we have presented preliminary results concerning the first $^{14}N/^{15}N$ measurements in a sample of protostellar envelopes. A possible, further expansion of this work will come from the analysis of the next evolutionary stage: protoplanetary discs. At the present day, this kind of study has been performed only on a few sources (see e.g. Guzmán et al. 2017; Hily-Blant et al. 2019), due to the intrinsic weak signal expected from the ^{15}N-bearing isotopologues. Moreover, $N^{15}NH^+$ is still undetected in protoplanetary discs. However, the recent improvements of observational capabilities concerning both sensitivity and angular resolution achieved especially by the ALMA interferometer have made these observations possible. In the near future, this will then allow us to obtain a comprehensive view of the evolution of N-chemistry from the early prestellar phases down to the sites of planet formation.

As previously stated, deuteration is linked to the gas ionisation fraction (see §1.5 and §3.1). This parameter, determining the degree of coupling between the matter and magnetic field lines, is crucial in determining the type of evolution of the ISM. Since it also determines the timescales for ambipolar diffusion, in prestellar cores the ionisation fraction is directly linked to the collapse time. It is hence clear that it represents an important quantity to be investigated observationally. However, the most recent studies on this topic date back more than twenty years, and they consisted only of single-pointing observations (Caselli et al. 1998; Bergin et al. 1999). Thanks to the new results presented in Chapter 3, we can now produce the first map of ionisation fraction in the prototypical prestellar source L1544. From the map of $x(e)$, we will derive the map of the cosmic-ray ionisation rate (ζ), since $x(e) \propto \sqrt{\zeta/n(H_2)}$ (Ciolek & Mouschovias 1995). This will give us the unique opportunity to test the theoretical model of cosmic rays propagation, such as the one of Padovani et al. (2018). This work will provide key informations about the coupling between gas and magnetic field at different positions and depths in the source, hence addressing directly the problem of magnetic braking.

The magnetic field properties in IRAS15398, which have been discussed in Chapter 4, also

need to be addressed with further investigation. Besides the line observations presented as preliminary results in §4.6, we planned a second, deeper campaign with the SOFIA/HAWC+ camera. We aim to obtain a better sensitivity, which will allow as to preserve the instrument native resolution (19″) and to have more detections in the less dense filamentary structure surrounding the central core. In this way, we will be able to reconstruct the more extended morphology of the magnetic fields, which will then be compared with the source kinematic structure. Finally, we believe that IRAS15398 is the ideal target to study the polarised dust thermal emission in the protostar envelope (hundreds of AU). These observations, which can be performed with ALMA, will allow us to recover a multi-scale view of the magnetic field in this source, from the large scales traced by the optical polarimetry, to the core properties obtained with the SOFIA data, down to the envelope (and disc/envelope transition) unveiled by interferometric observations.

5.2 Final remarks

In this thesis we have investigated the chemical and dynamical properties of low-mass star forming regions, using as an Ariadne's thread observations either in continuum or in lines in the frequency range 100 – 1000 GHz. Molecular transitions are particularly effective in probing the chemistry and kinematics of the interstellar medium. We have addressed heterogeneous astronomical problems, from the abundance of rare and faint molecules, such as the ^{15}N-bearing isotopologues, to the evolutionary information brought by deuterated species, to the magnetic field properties traced by polarised dust thermal emission. Despite the diversity of these projects, they all stand on a common ground, which consists of the ambitious goal of understanding the details about how stars such as our Sun are born. In this extensive context, each of the chapters of this thesis represents a piece of the puzzle. Future works will bring new pieces, in the hope of reconstructing, one day, the full picture.

Appendix A

Complementary Material for Chapter 2

A.1 New hyperfine rate coefficients for the N_2H^+/p-H_2 collisional system

Recently, Lique et al. (2015) published a new set of theoretically computed hyperfine rate coefficients of N_2H^+ ($X^1\Sigma^+$) excited by p-H_2 ($j = 0$). The scattering calculation is based on a high-level ab initio potential energy surface (PES), from which state-to-state rate coefficients between the low-lying hyperfine levels were derived for temperatures ranging from 5 to 70 K. These new results provided the first genuine description of the N_2H^+/p-H_2 collisional system, much improving the one based on previously published studies (Daniel et al. 2004, 2005) which used the He atom as collision partner. Indeed, the dissimilar polarisability of H_2 and He has a sizeable effect on the long-range electrostatic interaction and produces a marked difference in the corresponding collision cross sections. Lique et al. (2015) found discrepancies up to a factor of ~ 3 (N_2H^+/p-H_2 being the larger), indicating that the commonly used scaling factor of 1.37 (based on reduced masses) is not appropriate for these systems.

In a previous non-LTE analysis of N_2H^+ emission in L1544 (Bizzocchi et al. 2013), a J-dependent scaling relation based on HCO^+–H_2 and HCO^+–He rate coefficients was adopted. This scheme produced factors in the 1.4–3.2 interval with an average ratio of ~ 2.3 for $1 \leq j \leq 4$, and therefore allowed for a more reliable modelling of the N_2H^+ collisional excitation in the ISM[1]. However, the newly computed set of genuine N_2H^+/p-H_2 collision data clearly supersedes the one derived through this procedure. The RT modellings presented in this paper were therefore performed inserting the N_2H^+/p-H_2, $N^{15}NH^+/p$-H_2, and $^{15}NNH^+/p$-H_2 rate coefficients derived from Lique et al. (2015) into MOLLIE.

Hyperfine de-excitation rate coefficients for the main isotopologue have been made available through the BASECOL[2] database (Dubernet et al. 2013). They are derived from a Maxwellian

[1] In order to be consistent with the formalism employed in collision studies (e.g., Daniel et al. 2005; Lique et al. 2015), in this appendix the lower-case symbol j is used for the quantum number of the molecule end-over-end rotation.

[2] `http://basecol.obspm.fr/`

average over the corresponding hyperfine cross-sections $\sigma_{\alpha\beta}$ (Lique et al. 2015)

$$R_{\alpha\to\beta}(T) = \left(\frac{8}{\pi\mu k_B^3 T^3}\right)^{1/2} \int_0^\infty \sigma_{\alpha\beta} E_c \mathrm{e}^{-E_c/k_B T} \mathrm{d}E_c \,, \tag{A.1}$$

where μ is the reduced mass of the collision system, E_c is the collision energy, and α, β are the initial and final levels, respectively, each labelled with the j, F_1, F quantum numbers. These are obtained by coupling the rotational angular momentum with the two ^{14}N nuclear spins, for example $\mathbf{F}_1 = \mathbf{j} + \mathbf{I}_1$, and $\mathbf{F} = \mathbf{F}_1 + \mathbf{I}_2$. The cross sections are, in turn, obtained by the recoupling technique starting from the "spinless" opacity tensor elements $P^K(j \to j')$:

$$\sigma_{jF_1F\to j'F_1'F'} = \frac{\pi}{k_j^2}[F_1\, F_1'\, F'] \sum_K \begin{Bmatrix} F_1 & F_1' & K \\ F' & F & I_2 \end{Bmatrix}^2 \begin{Bmatrix} j & j' & K \\ F_1' & F_1 & I_1 \end{Bmatrix}^2 P^K(j \to j') \,. \tag{A.2}$$

Here, k_j is the wave-vector for the energy channel E_c, $k_j^2 = (2\mu/\hbar^2)(E_c - E_j)$; the terms in brace parentheses are the Wigner-6j symbols, and the notation $[xy\ldots]$ is a handy shorthand for the product $(2x+1)(2y+1)\ldots$.

Hyperfine cross-sections for the N^{15}NH$^+$, and ^{15}NNH$^+$ isotopic variant (one ^{14}N nucleus) are not included in the BASECOL compilation. They can however be obtained, to a very good approximation, by summing Eq. A.2 over the final F' states. Using the orthogonality property of the 6j symbols it holds:

$$\sum_{F'} [F'] \begin{Bmatrix} F_1 & F_1' & K \\ F' & F & I_2 \end{Bmatrix}^2 = [F_1]^{-1} \,, \tag{A.3}$$

because the triads (F_1', F_1, K) and (I_2, F, F') satisfy the triangular condition by definition (Daniel et al. 2004). Hence, one has the equality:

$$\sum_{F'} \sigma_{jF_1F\to j'F_1'F'} = \frac{\pi}{k_j^2}[F_1'] \begin{Bmatrix} j & j' & K \\ F_1' & F_1 & I_1 \end{Bmatrix}^2 P^K(j \to j') = \sigma_{jF_1\to j'F_1'} \,, \tag{A.4}$$

which, inserted in the A.1 yields, to a very good approximation:

$$\sum_{F'} R_{jF_1F\to j'F_1'F'}(T) = R_{jF_1\to j'F_1'}(T) \,. \tag{A.5}$$

The ^{15}N-bearing isotopologues contain only one quadrupolar nucleus and the appropriate angular momentum addition scheme is $\mathbf{F} = \mathbf{j} + \mathbf{I}$. Therefore, in the right-hand term of A.5, the quantum number F_1 can be replaced by the new F to give the hyperfine coefficients for the N^{15}NH$^+$/p-H$_2$ and ^{15}NNH$^+$/p-H$_2$ collisions. In this treatment, we neglected the isotopic dependence of the cross sections, which is expected to be negligible for the ^{14}N↔^{15}N substitution (see for example Buffa et al. 2009).

The excitation rates, which are also required in MOLLIE, are derived through the detailed balance relations

$$R_{jF_1F\leftarrow j'F_1'F'}(T) = \frac{[F]}{[F']} R_{jF_1F\to j'F_1'F'}(T)\, \mathrm{e}^{-\Delta E/k_B T} \,, \quad \text{for } N_2H^+ \,, \tag{A.6}$$

$$R_{jF\to j'F'}(T) = \frac{[F]}{[F']} R_{jF\to j'F'}(T)\, \mathrm{e}^{-\Delta E/k_B T}\,, \quad \text{for } \mathrm{N^{15}NH^+} \text{ and } {}^{15}\mathrm{NNH^+}\,, \tag{A.7}$$

where ΔE represents the energy difference between the hyperfine levels (jF_1F) and $(j'F'_1F')$ or (jF) and $(j'F')$.

A.2 χ^2 analysis

In this Appendix, we show the χ^2 values used to determine the best-fit value for the abundance (and therefore for the column density) of each molecule, together with their uncertainties, in L183, L694-2 and L1544 (Figures A.1–A.3). The χ^2 is evaluated according to Eq. 2.4. L429 is not present due to the difficulties of its modelling. See the main text for more details.

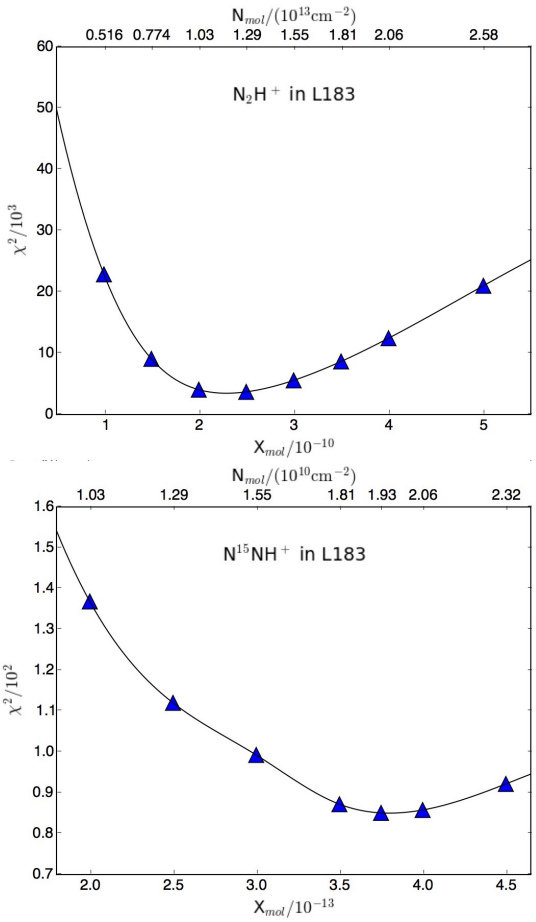

Figure A.1: The χ^2 values for different abundance values (and corresponding column densities) in L183, for N_2H^+ (upper panel) and $N^{15}NH^+$ (lower panel). The black curve is the one used to estimate the uncertainties, according to what said in §2.4.2.

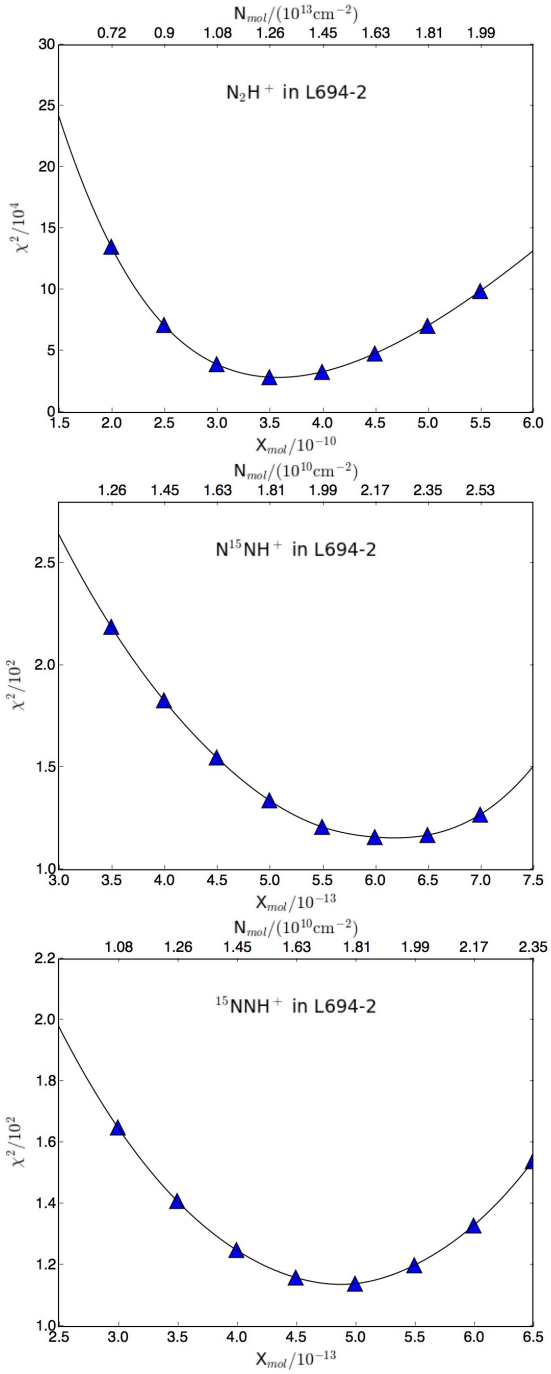

Figure A.2: The χ^2 values for different abundance values (and corresponding column densities) for L694-2. From top to bottom: N_2H^+, $N^{15}NH^+$, $^{15}NNH^+$. The black curve is the one used to estimate the uncertainties, as explained in §2.4.2.

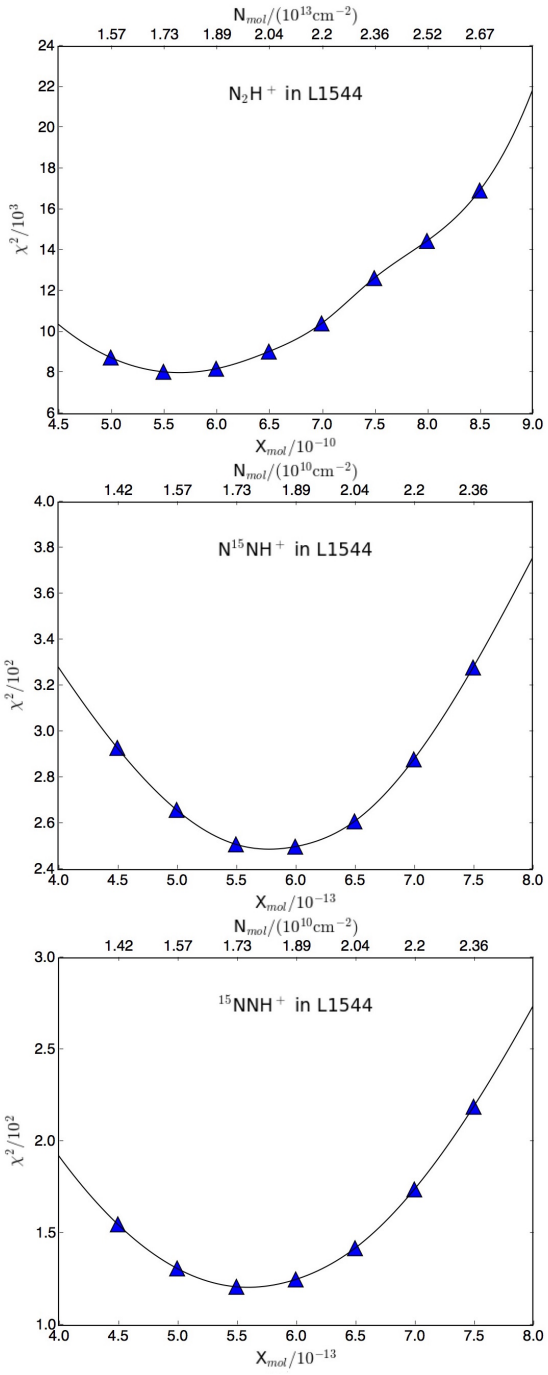

Figure A.3: The χ^2 values obtained for different abundance values (and corresponding column densities) in L1544. From top to bottom: N_2H^+, $N^{15}NH^+$, $^{15}NNH^+$. The black curve is the one used to estimate the uncertainties, as explained in §2.4.2.

Appendix B

Complementary Material for Chapter 3

B.1 The spectroscopic constants

In Table B.1 we report the values of the spectroscopic parameters used to derive the column densities, according to the method explained in §3.3.4. The references for the shown values are reported in the last column of the table. Figures B.1 and B.2 show the partition function for N_2H^+ and HCO^+ (and isotopologues), respectively. In the considered range of temperatures, the correlation is almost linear.

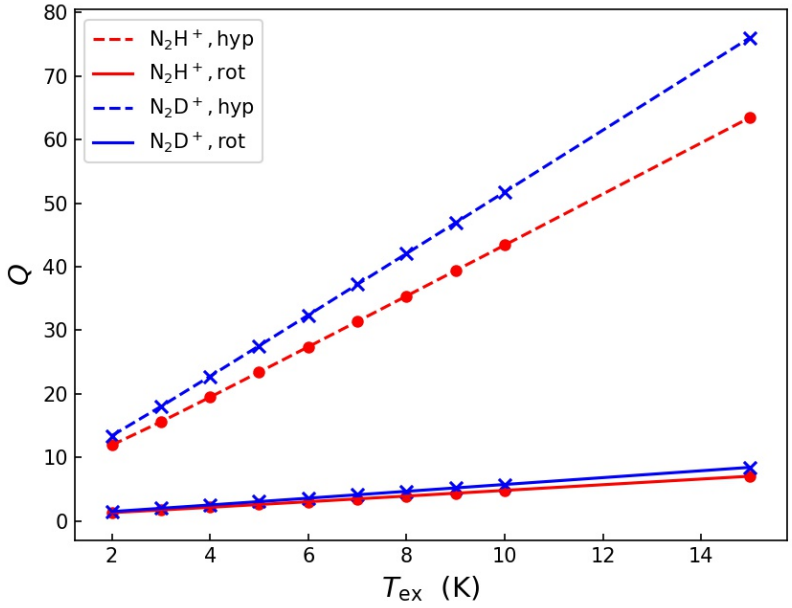

Figure B.1: Partition function of N_2H^+ (red circles) and N_2D^+ (blue crosses) as a function of excitation temperature. Q for rotational transition, neglecting the hyperfine structure, are indicated with solid lines, while the dashed curves take into account all the hyperfine levels.

Table B.1: Spectroscopic values for the transitions used in the analysis to derive the molecular column densities.

Rotational transition	Hyperfine component[a]	ν GHz	g_u	E_u/k_B K	A_{ul} 10^{-5} s^{-1}	Ref.[c]
		N_2H^+				
$J = 1-0$	$J, F_1, F = 1,0,1 \leftarrow 0,1,*$[b]	93.1762604	3	4.472	3.628	1
$J = 3-2$	$J, F_1, F = 3,4,5 \leftarrow 2,3,4$	279.5118572	11	13.41	1.259×10^2	1
		N_2D^+				
$J = 1-0$	$J, F_1, F = 1,0,1 \leftarrow 0,1,*$	77.1121207	3	3.701	2.057	2
$J = 2-1$	$J, F_1, F = 2,3,3 \leftarrow 1,2,2$	154.2170958	7	11.10	18.08	2
$J = 2-1$	$J, F_1, F = 2,3,2 \leftarrow 1,2,1$	154.2171220	5	11.10	15.63	2
$J = 2-1$	$J, F_1, F = 2,2,3 \leftarrow 1,1,2$	154.2171273	7	11.10	14.17	2
$J = 2-1$	$J, F_1, F = 2,3,4 \leftarrow 1,2,3$	154.2171888	9	11.10	19.74	2
$J = 3-2$	-	231.3218611	7	22.20	71.38	2
		DCO^+				
$J = 1-0$	-	72.0393123	3	3.457	2.206	3
$J = 2-1$	-	144.0772854	5	10.37	21.18	3
$J = 3-2$	-	216.1125804	7	20.74	76.58	3
		$HC^{18}O^+$				
$J = 1-0$	-	85.1622231	3	4.087	3.645	4

[a] When no hyperfine component is indicated, the transition is intended as a single transition;

[b] The notation $J, F_1, F \leftarrow J', F_1', *$ indicates that there are multiple but degenerate lower states, which have the same energy but different F quantum number;

[c] The spectroscopic data are taken from: [1] Our calculation based on data from Cazzoli et al. (2012), [2]) our calculation based on data from Dore et al. (2004); Amano et al. (2005); Yu et al. (2015), [3] our calculation based on data from Caselli & Dore (2005); Lattanzi et al. (2007), and [2] from Bizzocchi et al. (in prep.).

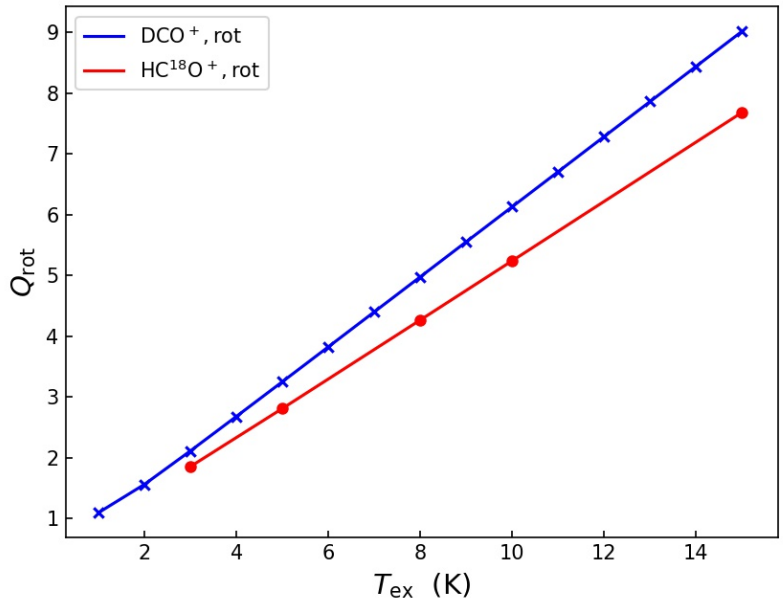

Figure B.2: Rotational partition function of DCO^+ (blue crosses) and $HC^{18}O^+$ (red dots), as a function of T_{ex}.

B.2 Molecular abundance profiles

Here, we plot the abundance profiles computed with our chemical network and tested with the non-LTE approach. Figure B.3, B.4, and B.5 show the models at the five different time-steps, respectively, for $A_V = 1, 2,$ and 5.

B.3 Discussion on the excitation temperature

As described in §2.4, a main issue to derive the molecular column density when its rotational lines are observed consists in determining the excitation temperatures of the transitions. When T_{ex} is not the same for all the lines (or when just one line is available), the problem becomes degenerate. A non-LTE analysis is therefore necessary to constrain these parameters (N_{mol} and T_{ex}) independently.

One could argue that MOLLIE can be used to derive the T_{ex} values directly. This is only partially true. MOLLIE, as in any non-LTE radiative transfer code that performs ray tracing, does not operate directly with the excitation temperature quantity; it propagates and counts photons, and it solves the statistical equilibrium equations for the energy level populations. The latter are indeed related to T_{ex} through the Boltzmann equation. However, the T_{ex} obtained in this

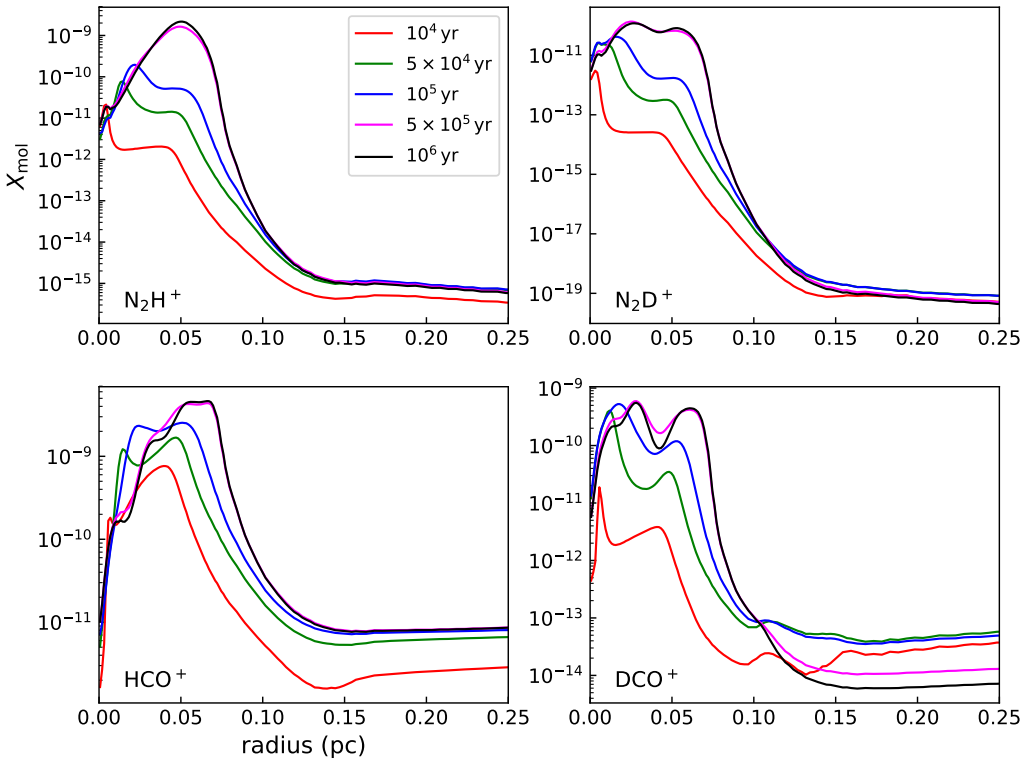

Figure B.3: Molecular abundances in the model with $A_V = 1$ mag for N_2H^+ (top-left), N_2D^+ (top-right), HCO^+ (bottom-left), and DCO^+ (bottom-right). The colours represent the different time-steps: 10^4 yr (red), 5×10^4 yr (green), 10^5 yr (blue), 5×10^5 yr (purple), and 10^6 yr (black).

way are only local values, since they can be computed cell by cell[1]. The result is therefore a one-dimensional radial profile of T_{ex} for each transition.

On the other hand, the T_{ex} that appears in the equations of radiative transfer is an average quantity, integrated along the line of sight and over the beam size, which relates the observed fluxes with the molecular column density for the beam of that specific observation. It is not straightforward to link the local T_{ex} profiles obtained in MOLLIE with the T_{ex} values needed to compute N_{mol}, especially because T_{ex} is an intensive quantity. An approach that we have tested is to integrate the T_{ex} profiles along the line of sight, using the H_2 column density as a weighting function. Since H_2 is the main collisional partner, this choice seems reasonable. However, it neglects other important parameters that affect T_{ex}, such as the gas temperature and the density of the molecule itself. Another point that must be taken into account is that, contrary to T_{ex}, the molecular abundance is an extensive quantity that can be multiplied by $n(H_2)$ and integrated along the line-of-sight to derive the molecular column density without any ambiguity. It is a natural requirement that the two methods to derive N_{mol}, i.e. the physical and chemical modelling done

[1]In our simulation, the finest spatial grid has a resolution of $3\,10^{-3}$ pc, orders of magnitude smaller than the resolution of the observed spectra.

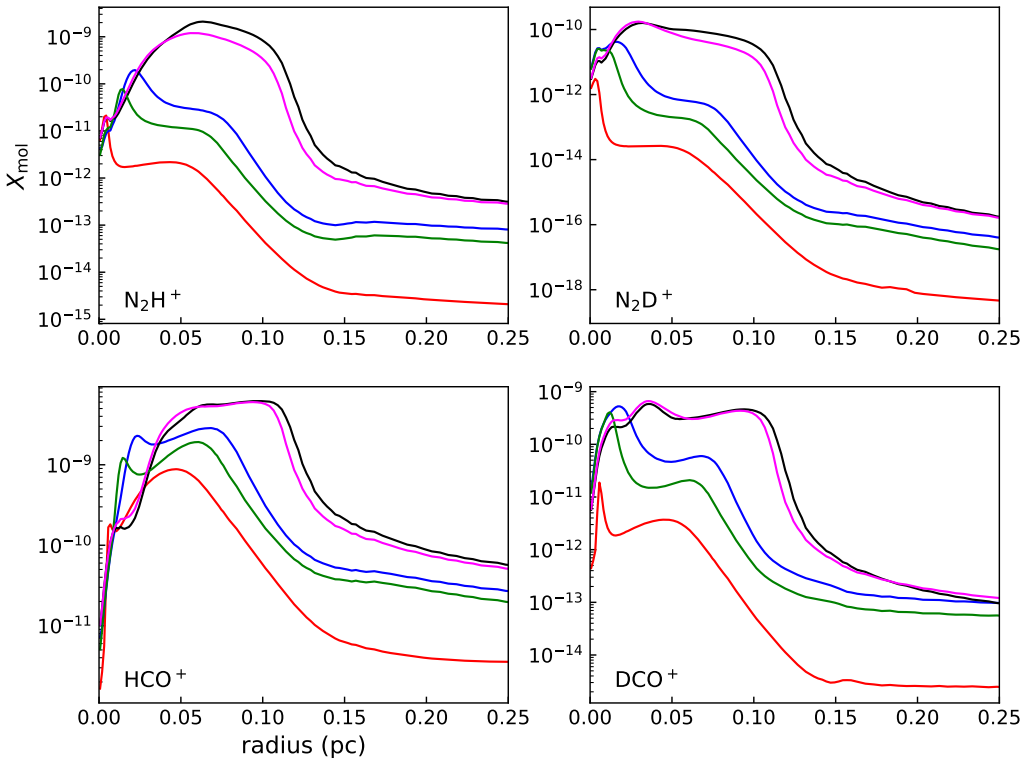

Figure B.4: Same as Fig. B.3, but for $A_V = 2$ mag.

with MOLLIE and the solution of Eqs. 3.1 and 3.2, must be consistent and provide the same result at the centre of the core. With this constraint, T_{ex} becomes a free parameter that can be tuned to ensure the required consistency. This is the selected method to derive the T_{ex} values reported in Table 3.3.

We reiterate that this approach is possible only at the dust peak, because the physical and chemical models are spherically symmetric and cannot reproduce the asymmetries of the core that the observations unveil. Furthermore, the model of Keto et al. (2015) has been specifically developed to reproduce the dust peak.

A strong assumption that we make in §3.3.4 is that the T_{ex} values found, as described immediately above, are constant throughout our map coverage. This is questionable, since one might expect molecules to be less excited in the outskirts of the core, where the gas is less dense. In order to investigate this point, we tried to derive the DCO^+ column density using a decreasing T_{ex} profile for each line. DCO^+ is a representative case, because it has a more extended distribution than for instance N_2D^+ and three transitions are available at the same time. We realised that a decrease of more than $0.5 - 1.0$ K within $\approx 60''$ (the limit of our map coverage) is enough to cause our N_{mol} fitting routine to break down. With these profiles, the resulting N_{mol} maps present unphysical features, such as values at the border of the core that are several times higher than at the integrated intensity peak, and/or unrealistic morphologies.

In order to further test this assumption, we focus on N_2D^+. As already mentioned, MOLLIE

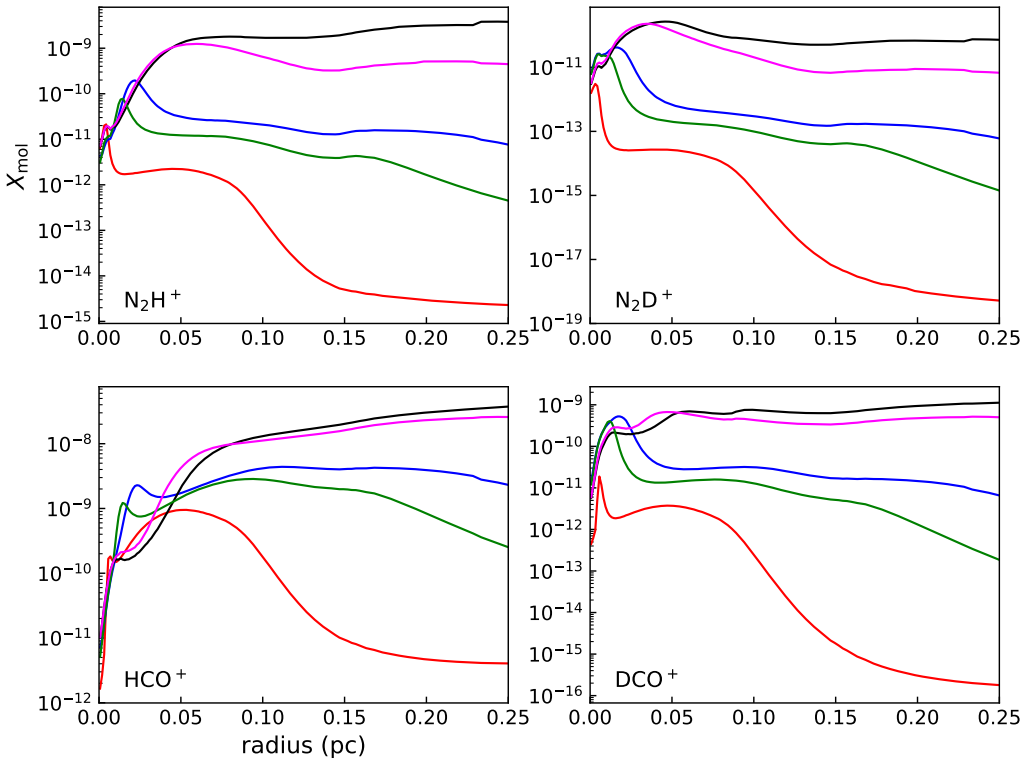

Figure B.5: Same as Fig. B.3, but for $A_V = 5$ mag.

and our physical and chemical models are not able to reproduce the observed spectra outside the dust peak. However, N_2D^+ is sufficiently centrally concentrated and symmetric around the centre of the core to allow a reasonable fit to the observations also outside dust peak. In particular, we were able to compare the synthetic spectra extracted from the model at 40″ offset with the observed signals obtained by averaging the data in a ring at a distance of 40″ from the centre of the core. We can therefore constrain N_{mol} at two different offsets, and verify that the T_{ex} values that reproduce these column densities are equal within the uncertainties. Figure B.6 shows the results of this analysis. The red and green dashed lines represent the T_{MB} observed values of the line components used to derive N_{mol} (see §3.3.4), at the dust peak and at 40″ offset, respectively. The shaded area indicates the spectra rms[2]. The solid curves indicate the T_{MB} of each line as a function of T_{ex}, obtained using Eqs. 3.1 and 3.2 using the column density values predicted by MOLLIE at the two offsets (3.5 and 1.6×10^{12} cm^{-2}, respectively). Finally, the black dashed lines show the T_{ex} values adopted in this work, and the grey shadows indicate a 0.5 K variation of this quantity. All the observations are smoothed at the same beam size (34″), which is the resolution of the final N_{mol} map. For all three transitions the solid lines cross the interceptions of the shaded areas, suggesting that within our uncertainties we are not able to detect a significant change of T_{ex}.

[2]These uncertainties are lower limits, since they do not take into account the calibration uncertainties (up to 15%).

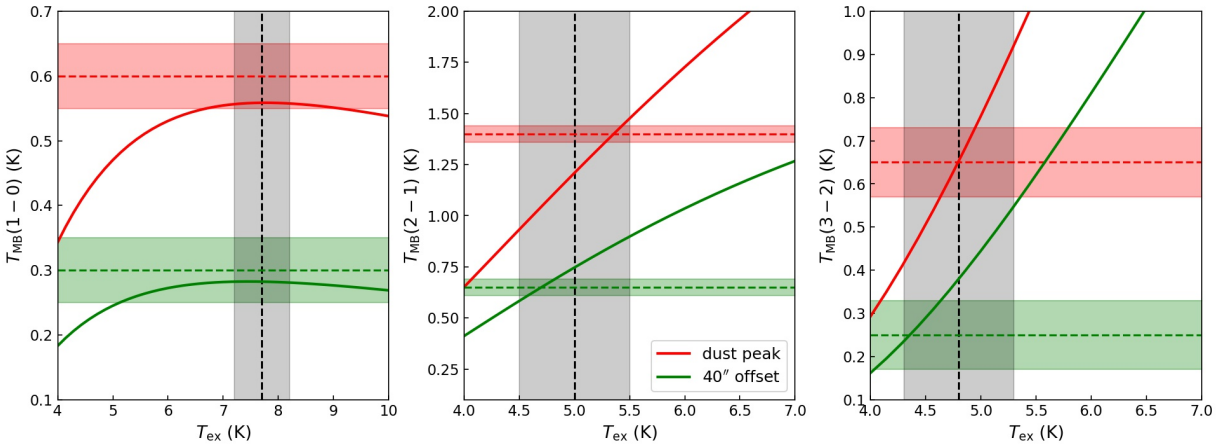

Figure B.6: Isolated component of N_2D^+ (1-0) (left panel), the central component of N_2D^+ (2-1) (centre), and the N_2D^+ (3-2) line (right panel). In each panel, the horizontal dashed lines are the observed peak temperatures of the selected N_2D^+ transition at the dust peak (red), and at 40" of offset (green). The shadowed areas represent observational uncertainties. The solid curves indicate T_{MB} as a function of T_{ex}, obtained via the radiative transfer equations and using the column density values predicted by MOLLIE at the two offsets. The vertical dashed line is the T_{ex} value used in the analysis of the maps, and the grey shaded area is its uncertainty (0.5 K).

We want to highlight that our analysis does not imply that T_{ex} is indeed constant across the whole core, but only that our observations are not sensitive to its variation and that they can be analysed assuming a constant value. Most likely, this is also due to the limited coverage of our maps, which are $2' \times 2'$ in size, meaning that in a core radius we have at most two or three independent beams. All this said, we assume that our T_{ex} values reported in Table 3.3 are accurate to within 0.5 K.

Appendix C

Complementary Material for Chapter 4

C.1 Stokes parameters

Figure C.1 reports in the three panels the Stokes parameters observed with SOFIA. The maps have been smoothed to 42″ with respect to a native resolution of 19″ to improve the S/N.

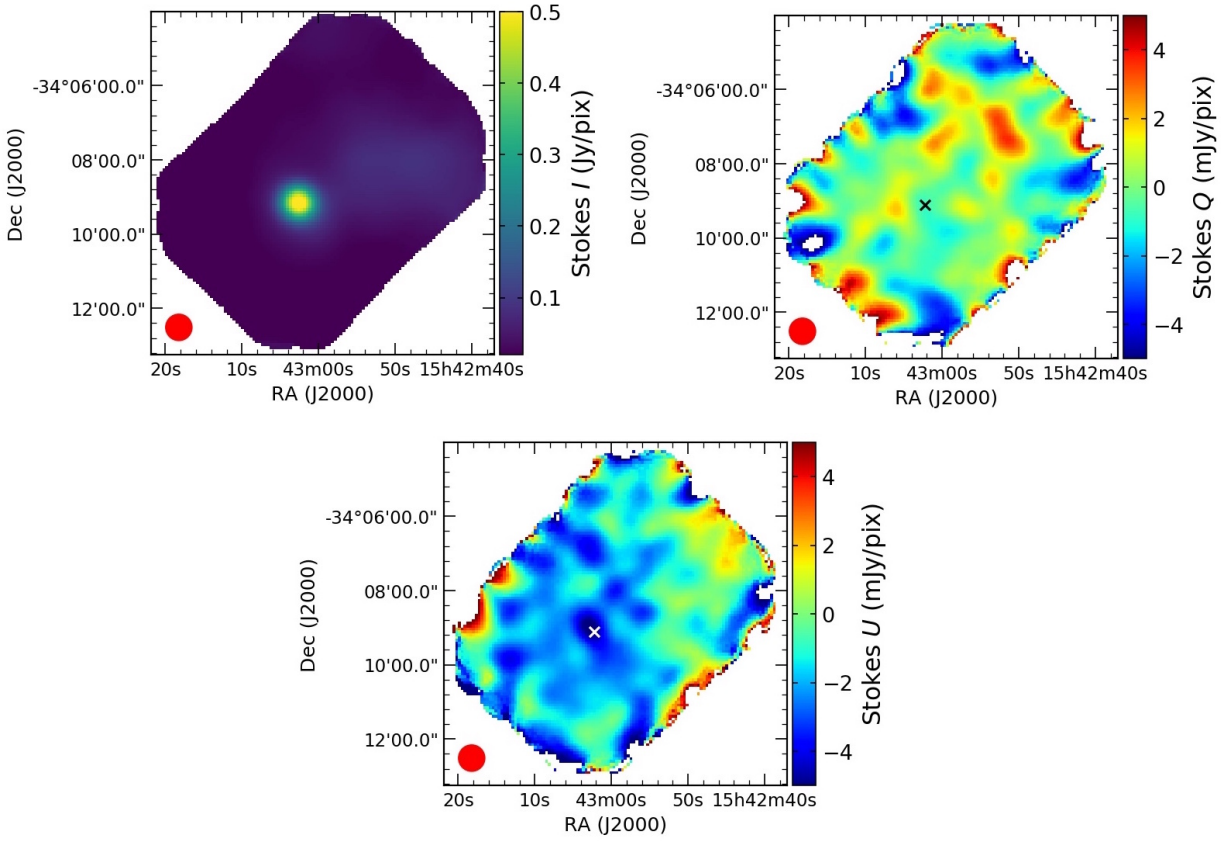

Figure C.1: Colour map of the three Stokes parameter I (top-left), Q (top-right), and U (bottom). The smoothed beam size is indicated in the bottom left corners. In the Stokes Q and U panels, the cross represents the position of the protostar.

Appendix D

Observing proposals used for this thesis

In this Appendix, we list the observing proposals concerning the data presented in this thesis, together with their facility and the Principal Investigator name.

- *Polarimetry in B228*,
  facility: SOFIA; PI: Elena Redaelli
- *The kinematics of a magnetised protostellar core*,
  facility: APEX; PI: Elena Redaelli
- *The* ^{14}N/^{15}N *ratio in low-mass protostars: a new step towards understanding N-chemistry*,
  facility: IRAM 30m telescope; PI: Elena Redaelli
- *Casting light on nitrogen chemistry*,
  facility: Green Bank Telescope; PI: Elena Redaelli
- *Detailed kinematics of the deuterated gas and ionisation fraction across a prototypical pre-stellar core*,
  facility: IRAM 30m telescope; PI: Dr. Luca Bizzocchi
- *Deuterated methanol and* CO *distribution in the starless core L1544*,
  facility: IRAM 30m telescope; PI: Dr. Luca Bizzocchi
- ^{15}N *fractionation at the starting point of star formation*,
  facility: IRAM 30m telescope; PI: Dr. Luca Bizzocchi
- *Investigating the nitrogen isotopic fractionation mechanism in cold quiescent clouds: search for* $N^{15}NH^+$ *and* $^{15}NNH^+$ *in L694-2*,
  facility: IRAM 30m telescope; PI: Dr. Luca Bizzocchi

Bibliography

Allen, A., Li, Z.-Y., & Shu, F. H. 2003, ApJ, 599, 363

Altwegg, K., Balsiger, H., Bar-Nun, A., et al. 2015, Science, 347, 1261952

Alves, F. O., Franco, G. A. P., & Girart, J. M. 2008, A&A, 486, L13

Alves, F. O., Frau, P., Girart, J. M., et al. 2014, A&A, 569, L1

Amano, T., Hirao, T., & Takano, J. 2005, Journal of Molecular Spectroscopy, 234, 170

Andersson, B. G., Lazarian, A., & Vaillancourt, J. E. 2015, ARA&A, 53, 501

André, P., Di Francesco, J., Ward-Thompson, D., et al. 2014, in Protostars and Planets VI, ed. H. Beuther, R. S. Klessen, C. P. Dullemond, & T. Henning, 27

André, P., Men'shchikov, A., Bontemps, S., et al. 2010, A&A, 518, L102

André, P., Ward-Thompson, D., & Barsony, M. 2000, in Protostars and Planets IV, ed. V. Mannings, A. P. Boss, & S. S. Russell, 59

Arzoumanian, D., André, P., Didelon, P., et al. 2011, A&A, 529, L6

Asplund, M., Grevesse, N., Sauval, A. J., & Scott, P. 2009, ARA&A, 47, 481

Bacmann, A., Lefloch, B., Ceccarelli, C., et al. 2002, A&A, 389, L6

Benedettini, M., Pezzuto, S., Burton, M. G., et al. 2012, MNRAS, 419, 238

Bergin, E. A., Plume, R., Williams, J. P., & Myers, P. C. 1999, ApJ, 512, 724

Bethell, T. J., Chepurnov, A., Lazarian, A., & Kim, J. 2007, ApJ, 663, 1055

Bizzocchi, L., Caselli, P., Leonardo, E., & Dore, L. 2013, A&A, 555, A109

Bizzocchi, L., Caselli, P., Spezzano, S., & Leonardo, E. 2014, A&A, 569, A27

Bjerkeli, P., Jørgensen, J. K., & Brinch, C. 2016, A&A, 587, A145

Black, J. H. 1994, in Astronomical Society of the Pacific Conference Series, Vol. 58, The First Symposium on the Infrared Cirrus and Diffuse Interstellar Clouds, ed. R. M. Cutri & W. B. Latter, 355

Bohlin, R. C., Savage, B. D., & Drake, J. F. 1978, ApJ, 224, 132

Bolatto, A. D., Wolfire, M., & Leroy, A. K. 2013, ARA&A, 51, 207

Bonal, L., Huss, G. R., Krot, A. N., et al. 2010, Geochim. Cosmochim. Acta, 74, 6590

Bracco, A., Palmeirim, P., André, P., et al. 2017, A&A, 604, A52

Brauer, R., Wolf, S., & Reissl, S. 2016, A&A, 588, A129

Buffa, G., Dore, L., & Meuwly, M. 2009, MNRAS, 397, 1909

Caselli, P., Benson, P. J., Myers, P. C., & Tafalla, M. 2002a, ApJ, 572, 238

Caselli, P., Bizzocchi, L., Keto, E., et al. 2017, A&A, 603, L1

Caselli, P. & Dore, L. 2005, A&A, 433, 1145

Caselli, P., Keto, E., Bergin, E. A., et al. 2012, ApJ, 759, L37

Caselli, P., Walmsley, C. M., Tafalla, M., Dore, L., & Myers, P. C. 1999, ApJ, 523, L165

Caselli, P., Walmsley, C. M., Terzieva, R., & Herbst, E. 1998, ApJ, 499, 234

Caselli, P., Walmsley, C. M., Zucconi, A., et al. 2002b, ApJ, 565, 331

Caselli, P., Walmsley, C. M., Zucconi, A., et al. 2002c, ApJ, 565, 344

Cazzoli, G., Cludi, L., Buffa, G., & Puzzarini, C. 2012, ApJS, 203, 11

Ceccarelli, C., Caselli, P., Bockelée-Morvan, D., et al. 2014, in Protostars and Planets VI, ed. H. Beuther, R. S. Klessen, C. P. Dullemond, & T. Henning, 859

Chacón-Tanarro, A., Caselli, P., Bizzocchi, L., et al. 2017, A&A, 606, A142

Chacón-Tanarro, A., Caselli, P., Bizzocchi, L., et al. 2019, A&A, 622, A141

Chacon-Tanarro, A., Pineda, J. E., Caselli, P., et al. 2019, arXiv e-prints, arXiv:1901.02476

Chandrasekhar, S. & Fermi, E. 1953, ApJ, 118, 116

Charnley, S. B. & Rodgers, S. D. 2002, ApJ, 569, L133

Chen, M. C.-Y., Di Francesco, J., Johnstone, D., et al. 2016, ApJ, 826, 95

Chiang, H.-F., Looney, L. W., & Tobin, J. J. 2012, ApJ, 756, 168

Ciolek, G. E. & Mouschovias, T. C. 1995, ApJ, 454, 194

Colzi, L., Fontani, F., Caselli, P., et al. 2018a, A&A, 609

Colzi, L., Fontani, F., Rivilla, V. M., et al. 2018b, MNRAS, 976

Coudé, S., Bastien, P., Houde, M., et al. 2019, ApJ, 877, 88

Crapsi, A., Caselli, P., Walmsley, C. M., et al. 2005, ApJ, 619, 379

Crapsi, A., Caselli, P., Walmsley, M. C., & Tafalla, M. 2007, A&A, 470, 221

Crutcher, R. M. 2012, ARA&A, 50, 29

Crutcher, R. M., Nutter, D. J., Ward-Thompson, D., & Kirk, J. M. 2004, ApJ, 600, 279

Crutcher, R. M., Troland, T. H., Goodman, A. A., et al. 1993, ApJ, 407, 175

Crutcher, R. M., Wandelt, B., Heiles, C., Falgarone, E., & Troland, T. H. 2010, ApJ, 725, 466

Dalgarno, A. 2006, Proceedings of the National Academy of Science, 103, 12269

Dalgarno, A. & Lepp, S. 1984, ApJ, 287, L47

Daniel, F., Cernicharo, J., & Dubernet, M.-L. 2006, ApJ, 648, 461

Daniel, F., Cernicharo, J., Roueff, E., Gerin, M., & Dubernet, M. L. 2007, ApJ, 667, 980

Daniel, F., Dubernet, M.-L., & Meuwly, M. 2004, J. Chem. Phys., 121, 4540

Daniel, F., Dubernet, M.-L., Meuwly, M., Cernicharo, J., & Pagani, L. 2005, MNRAS, 363, 1083

Daniel, F., Faure, A., Pagani, L., et al. 2016, A&A, 592, A45

Daniel, F., Gérin, M., Roueff, E., et al. 2013, A&A, 560, A3

De Simone, M., Fontani, F., Codella, C., et al. 2018, MNRAS, 476, 1982

Dolginov, A. Z. & Mitrofanov, I. G. 1976, Ap&SS, 43, 291

Dore, L., Bizzocchi, L., Degli Esposti, C., & Tinti, F. 2009, A&A, 496, 275

Dore, L., Caselli, P., Beninati, S., et al. 2004, A&A, 413, 1177

Doty, S. D., Schöier, F. L., & van Dishoeck, E. F. 2004, A&A, 418, 1021

Dubernet, M.-L., Alexander, M. H., Ba, Y. A., et al. 2013, A&A, 553, A50

Dzib, S. A., Loinard, L., Ortiz-León, G. N., Rodríguez, L. F., & Galli, P. A. B. 2018, ApJ, 867, 151

Emprechtinger, M., Caselli, P., Volgenau, N. H., Stutzki, J., & Wiedner, M. C. 2009, A&A, 493, 89

Falgarone, E., Troland, T. H., Crutcher, R. M., & Paubert, G. 2008, A&A, 487, 247

Fiedler, R. A. & Mouschovias, T. C. 1993, ApJ, 415, 680

Flower, D. R. 1999, MNRAS, 305, 651

Fontani, F., Caselli, P., Palau, A., Bizzocchi, L., & Ceccarelli, C. 2015, ApJ, 808, L46

Fouchet, T., Irwin, P. G. J., Parrish, P., et al. 2004, Icarus, 172, 50

Franco, G. A. P. & Alves, F. O. 2015, ApJ, 807, 5

Frau, P., Girart, J. M., Zhang, Q., & Rao, R. 2014, A&A, 567, A116

Furuya, K. & Aikawa, Y. 2018, ApJ, 857, 105

Galli, D., Lizano, S., Shu, F. H., & Allen, A. 2006, ApJ, 647, 374

Garrod, R. T., Wakelam, V., & Herbst, E. 2007, A&A, 467, 1103

Gerin, M., Marcelino, N., Biver, N., et al. 2009, A&A, 498, L9

Gerin, M., Pety, J., Fuente, A., et al. 2015, A&A, 577, L2

Girart, J. M., Rao, R., & Marrone, D. P. 2006, Science, 313, 812

Goldsmith, P. F. 2001, ApJ, 557, 736

Goldsmith, P. F. & Langer, W. D. 1999, ApJ, 517, 209

Goodman, A. A., Bastien, P., Myers, P. C., & Menard, F. 1990, ApJ, 359, 363

Gourier, D., Robert, F., Delpoux, O., et al. 2008, Geochim. Cosmochim. Acta, 72, 1914

Green, J. A., Caswell, J. L., & McClure-Griffiths, N. M. 2015, MNRAS, 451, 74

Guelin, M., Langer, W. D., Snell, R. L., & Wootten, H. A. 1977, ApJ, 217, L165

Guzmán, V. V., Öberg, K. I., Huang, J., Loomis, R., & Qi, C. 2017, ApJ, 836, 30

Hall, J. S. 1949, Science, 109, 166

Harper, D. A., Runyan, M. C., Dowell, C. D., et al. 2018, Journal of Astronomical Instrumentation, 7, 1840008

Harvey, D. W. A., Wilner, D. J., Lada, C. J., Myers, P. C., & Alves, J. F. 2003a, ApJ, 598, 1112

Harvey, D. W. A., Wilner, D. J., Myers, P. C., & Tafalla, M. 2003b, ApJ, 597, 424

Hildebrand, R. H. 1983, QJRAS, 24, 267

Hildebrand, R. H., Kirby, L., Dotson, J. L., Houde, M., & Vaillancourt, J. E. 2009, ApJ, 696, 567

Hily-Blant, P., Bonal, L., Faure, A., & Quirico, E. 2013, Icarus, 223, 582

Hily-Blant, P., Magalhaes, V., Kastner, J., et al. 2017, A&A, 603, L6

Hily-Blant, P., Magalhaes de Souza, V., Kastner, J., & Forveille, T. 2019, arXiv e-prints, arXiv:1911.06676

Hily-Blant, P., Walmsley, M., Pineau Des Forêts, G., & Flower, D. 2010, A&A, 513, A41

Houde, M., Vaillancourt, J. E., Hildebrand, R. H., Chitsazzadeh, S., & Kirby, L. 2009, ApJ, 706, 1504

Hull, C. L. H. & Zhang, Q. 2019, Frontiers in Astronomy and Space Sciences, 6, 3

Jones, T. J., Bagley, M., Krejny, M., Andersson, B. G., & Bastien, P. 2015, AJ, 149, 31

Jones, T. J., Gordon, M., Shenoy, D., et al. 2016, AJ, 151, 156

Jørgensen, J. K., Bourke, T. L., Myers, P. C., et al. 2007, ApJ, 659, 479

Juvela, M. 2005, A&A, 440, 531

Juvela, M., Padoan, P., & Nordlund, Å. 2001, ApJ, 563, 853

Kahane, C., Jaber Al-Edhari, A., Ceccarelli, C., et al. 2018, ApJ, 852

Kataoka, A., Muto, T., Momose, M., et al. 2015, ApJ, 809, 78

Kauffmann, J., Bertoldi, F., Bourke, T. L., Evans, N. J., I., & Lee, C. W. 2008, A&A, 487, 993

Keto, E. & Caselli, P. 2010, MNRAS, 402, 1625

Keto, E., Caselli, P., & Rawlings, J. 2015, MNRAS, 446, 3731

Keto, E., Rybicki, G. B., Bergin, E. A., & Plume, R. 2004, ApJ, 613, 355

Keto, E. R. 1990, ApJ, 355, 190

Kong, S., Caselli, P., Tan, J. C., Wakelam, V., & Sipilä, O. 2015, ApJ, 804, 98

Kramer, C., Alves, J., Lada, C. J., et al. 1999, A&A, 342, 257

Kutner, M. L. & Ulich, B. L. 1981, ApJ, 250, 341

Kwon, J., Doi, Y., Tamura, M., et al. 2018, ApJ, 859, 4

Kwon, W., Looney, L. W., Mundy, L. G., Chiang, H.-F., & Kemball, A. J. 2009, ApJ, 696, 841

Lattanzi, V., Walters, A., Drouin, B. J., & Pearson, J. C. 2007, ApJ, 662, 771

Lawson, P. A., Osborne, David, J., & Adams, N. G. 2011, International Journal of Mass Spectrometry, 304, 41

Lazarian, A. 2007, J. Quant. Spec. Radiat. Transf., 106, 225

Lazarian, A., Andersson, B. G., & Hoang, T. 2015, Grain alignment: Role of radiative torques and paramagnetic relaxation, 81

Lecuyer, C., Gillet, P., & Robert, F. 1998, Chemical Geology, 145, 249

Lee, C. W., Myers, P. C., & Tafalla, M. 2001, ApJS, 136, 703

Lee, S. H., Park, Y.-S., Sohn, J., Lee, C. W., & Lee, H. M. 2007, ApJ, 660, 1326

Leger, A., Jura, M., & Omont, A. 1985, A&A, 144, 147

Li, A. 2008, arXiv e-prints, arXiv:0808.4117

Li, H. B., Goodman, A., Sridharan, T. K., et al. 2014, in Protostars and Planets VI, ed. H. Beuther, R. S. Klessen, C. P. Dullemond, & T. Henning, 101

Li, Z.-Y., Krasnopolsky, R., & Shang, H. 2013, ApJ, 774, 82

Linsky, J. L., Draine, B. T., Moos, H. W., et al. 2006, ApJ, 647, 1106

Lique, F., Daniel, F., Pagani, L., & Feautrier, N. 2015, MNRAS, 446, 1245

Liu, J., Qiu, K., Berry, D., et al. 2019, ApJ, 877, 43

Loison, J.-C., Wakelam, V., Gratier, P., & Hickson, K. M. 2019, MNRAS, 484, 2747

Mac Low, M.-M. & Klessen, R. S. 2004, Reviews of Modern Physics, 76, 125

Mangum, J. G., Emerson, D. T., & Greisen, E. W. 2007, A&A, 474, 679

Marty, B., Chaussidon, M., Wiens, R. C., Jurewicz, A. J. G., & Burnett, D. S. 2011, Science, 332, 1533

Matthews, B. C., McPhee, C. A., Fissel, L. M., & Curran, R. L. 2009, ApJS, 182, 143

McKee, C. F. 1989, ApJ, 345, 782

McKee, C. F. & Ostriker, E. C. 2007, ARA&A, 45, 565

McKee, C. F. & Ostriker, J. P. 1977, ApJ, 218, 148

Mellon, R. R. & Li, Z.-Y. 2008, ApJ, 681, 1356

Mezger, P. G., Wink, J. E., & Zylka, R. 1990, A&A, 228, 95

Milam, S. N., Savage, C., Brewster, M. A., Ziurys, L. M., & Wyckoff, S. 2005, ApJ, 634, 1126

Mouschovias, T. C. & Spitzer, L., J. 1976, ApJ, 210, 326

Nakamura, F. & Li, Z.-Y. 2008, ApJ, 687, 354

Nakano, T. & Nakamura, T. 1978, PASJ, 30, 671

Nguyen, T., Baouche, S., Congiu, E., et al. 2018, A&A, 619, A111

Nier, A. O. 1950, Physical Review, 77, 789

Ossenkopf, V. & Henning, T. 1994, A&A, 291, 943

Ostriker, E. C., Stone, J. M., & Gammie, C. F. 2001, ApJ, 546, 980

Oya, Y., Sakai, N., Sakai, T., et al. 2014, ApJ, 795, 152

Padoan, P., Goodman, A., Draine, B. T., et al. 2001, ApJ, 559, 1005

Padovani, M., Ivlev, A. V., Galli, D., & Caselli, P. 2018, A&A, 614, A111

Pagani, L., Bacmann, A., Cabrit, S., & Vastel, C. 2007, A&A, 467, 179

Pagani, L., Bacmann, A., Motte, F., et al. 2004, A&A, 417, 605

Pagani, L., Bourgoin, A., & Lique, F. 2012, A&A, 548, L4

Pelkonen, V. M., Juvela, M., & Padoan, P. 2009, A&A, 502, 833

Penzias, A. A. 1981, ApJ, 249, 518

Pignatari, M., Zinner, E., Hoppe, P., et al. 2015, ApJ, 808, L43

Planck Collaboration, Ade, P. A. R., Aghanim, N., et al. 2016, A&A, 586, A138

Punanova, A., Caselli, P., Pineda, J. E., et al. 2018, A&A, 617, A27

Redaelli, E., Alves, F. O., Caselli, P., et al. 2017, ApJ, 850, 202

Redaelli, E., Alves, F. O., Santos, F. P., & Caselli, P. 2019a, A&A, 631, A154

Redaelli, E., Bizzocchi, L., Caselli, P., et al. 2018, A&A, 617, A7

Redaelli, E., Bizzocchi, L., Caselli, P., et al. 2019b, A&A, 629, A15

Remusat, L., Robert, F., Meibom, A., et al. 2009, ApJ, 698, 2087

Robitaille, T. P. & Whitney, B. A. 2010, ApJ, 710, L11

Rodgers, S. D. & Charnley, S. B. 2008, MNRAS, 385, L48

Rohlfs, K. & Wilson, T. L. 2004, Tools of radio astronomy

Romano, D., Matteucci, F., Zhang, Z. Y., Papadopoulos, P. P., & Ivison, R. J. 2017, MNRAS, 470, 401

Roueff, E., Loison, J. C., & Hickson, K. M. 2015, A&A, 576, A99

Ruaud, M., Wakelam, V., & Hersant, F. 2016, MNRAS, 459, 3756

Rygl, K. L. J., Benedettini, M., Schisano, E., et al. 2013, A&A, 549, L1

Sánchez, A. G., Baugh, C. M., Percival, W. J., et al. 2006, MNRAS, 366, 189

Santos, F. P., Ade, P. A. R., Angilè, F. E., et al. 2017, ApJ, 837, 161

Santos, F. P., Busquet, G., Franco, G. A. P., Girart, J. M., & Zhang, Q. 2016, ApJ, 832, 186

Sarangi, A., Matsuura, M., & Micelotta, E. R. 2018, Space Sci. Rev., 214, 63

Schlafly, E. F., Green, G., Finkbeiner, D. P., et al. 2014, ApJ, 786, 29

Shirley, Y. L. 2015, Publications of the Astronomical Society of the Pacific, 127, 299

Sipilä, O., Caselli, P., & Harju, J. 2013, A&A, 554, A92

Sipilä, O., Caselli, P., & Harju, J. 2015a, A&A, 578, A55

Sipilä, O., Caselli, P., Redaelli, E., Juvela, M., & Bizzocchi, L. 2019, MNRAS, 487, 1269

Sipilä, O., Harju, J., Caselli, P., & Schlemmer, S. 2015b, A&A, 581, A122

Soam, A., Pattle, K., Ward-Thompson, D., et al. 2018, ApJ, 861, 65

Sohn, J., Lee, C. W., Park, Y.-S., et al. 2007, ApJ, 664, 928

Soler, J. D., Bracco, A., & Pon, A. 2018, A&A, 609, L3

Solomon, P. M., Rivolo, A. R., Barrett, J., & Yahil, A. 1987, ApJ, 319, 730

Spergel, D. N., Verde, L., Peiris, H. V., et al. 2003, ApJS, 148, 175

Spezzano, S., Bizzocchi, L., Caselli, P., Harju, J., & Brünken, S. 2016, A&A, 592, L11

Spezzano, S., Caselli, P., Bizzocchi, L., Giuliano, B. M., & Lattanzi, V. 2017, A&A, 606, A82

Stahler, S. W. & Palla, F. 2005, The Formation of Stars

Stark, R., Sandell, G., Beck, S. C., et al. 2004, ApJ, 608, 341

Tachihara, K., Dobashi, K., Mizuno, A., Ogawa, H., & Fukui, Y. 1996, PASJ, 48, 489

Tafalla, M., Mardones, D., Myers, P. C., et al. 1998, ApJ, 504, 900

Tafalla, M., Myers, P. C., Caselli, P., & Walmsley, C. M. 2004, A&A, 416, 191

Tafalla, M., Myers, P. C., Caselli, P., Walmsley, C. M., & Comito, C. 2002, ApJ, 569, 815

Takahashi, J. & Williams, D. A. 2000, MNRAS, 314, 273

Tazaki, R., Lazarian, A., & Nomura, H. 2017, ApJ, 839, 56

Terzieva, R. & Herbst, E. 2000, MNRAS, 317, 563

Troland, T. H. & Crutcher, R. M. 2008, ApJ, 680, 457

Trumpler, R. J. 1930, Lick Observatory Bulletin, 420, 154

Vaillancourt, J. E. 2006, PASP, 118, 1340

Verschuur, G. L. 1968, Phys. Rev. Lett., 21, 775

Visser, R., Bruderer, S., Cazzoletti, P., et al. 2018, A&A, 615, A75

Walker, C. K., Adams, F. C., & Lada, C. J. 1990, ApJ, 349, 515

Wang, J.-W., Lai, S.-P., Eswaraiah, C., et al. 2019, ApJ, 876, 42

Ward-Thompson, D., Motte, F., & Andre, P. 1999, MNRAS, 305, 143

Whittet, D. C. B., Hough, J. H., Lazarian, A., & Hoang, T. 2008, ApJ, 674, 304

Wilson, T. L. 1999, Reports on Progress in Physics, 62, 143

Wirström, E. S., Adande, G., Milam, S. N., Charnley, S. B., & Cordiner, M. A. 2016, IAU Focus Meeting, 29, 271

Wirström, E. S. & Charnley, S. B. 2018, MNRAS, 474, 3720

Yen, H.-W., Koch, P. M., Takakuwa, S., et al. 2017, ApJ, 834, 178

Yu, S., Pearson, J. C., Drouin, B. J., et al. 2015, Journal of Molecular Spectroscopy, 314, 19

Zuckerman, B. & Palmer, P. 1974, ARA&A, 12, 279

Acknowledgments

This thesis marks the end of a journey that began far from here in space and time. In a sense, all the people who took even a small part in it are to be acknowledged now, because they made this result possible. However, there are some names that I feel to thank explicitly, because without them I probably would not be here today.

First to be thanked, my supervisor Paola Caselli, who chose me for this PhD, gave me trust and invaluable advice, and led me from the university student I was three years ago to the scientist I hope to be today. Alongside with her, I would like to thank also Felipe. With your experience, you taught me so much that my whole career will keep trace of it. Thanks for supporting me in the bad days, and for sharing the joy of the good ones. And thanks to Luca, for the never-ending discussions about science and everything else. At certain times, I probably wouldn't have known what to do without you.

The entire CAS and in general MPE gang must be in this list. In particular, I want to mention Jo, Dome and Caro, for the happy moments we shared in the office 1.4.50, and outside of it; Michela and Vale, for the coffee-time chats; Ana and Vlas, for all the help you gave me in particular when I started, and for the friendship we built after that; Linda, for the fun we had on boulder walls, at the IMPRS parties, and more or less everywhere. Outside MPE, thanks to Laura: in these three years we came to know each other and became friends, and I hope we will always manage to meet here and there around the world.

I would also like to thank Silvia and Senni, for everything you offered me: laughs, food, and especially guidance. You helped me way more than you probably even realise.

Thanks to my friends of a life-time, Paola and Francesca, for having been there in every moment, low or high. In the last 10 years, our lives have taken quite different roads, but all the time you have been by my side: let's keep walking together. Thanks to Baglio, because despite the distance you have always supported me. And thanks to Giovanni, for being the amazing person you are: the master would have been impossible without you, and the PhD as well.

Thanks to my love, Matteo. My life in Munich started with you, and it now continues with you. Thanks for holding my hand when I needed it, and also when I didn't. So far it has been an incredible journey. I can't wait to see which new adventures the future has in store for us. And I am happy to thank also Matteo's family, for always making me feel at home with them.

And finally, thanks to my family, and in particular to my parents Antonella and Giorgio. None of this would have been possible without you. You taught me to walk, and then you let me climb the path I wanted, while being always there to cheer and encourage me. There are no words to describe what you did and still do for me. Just thank you.